

Engineering Impurity Behavior on the Micron-Scale in Metallurgical-Grade Silicon Production

By

Sarah Bernardis

B.S./M.S. Physics
Università degli Studi di Padova, 2005

M.S. Materials Science and Engineering
Massachusetts Institute of Technology, 2008

Submitted to the Department of Materials Science and Engineering in Partial Fulfillment of the
Requirements for the Degree of

Doctor of Philosophy in Materials Science and Engineering
at the
Massachusetts Institute of Technology

February 2012

© 2012 Massachusetts Institute of Technology. All rights reserved.

Signature of Author: _____
Department of Materials Science and Engineering

Certified by: _____
Kenneth C. Russell
Professor Emeritus of Metallurgy and Nuclear Engineering
Thesis Supervisor

Accepted by: _____
Christopher Schuh
Chair, Departmental Committee on Graduate Students

Engineering Impurity Behavior on the Micron-Scale in Metallurgical-Grade Silicon Production

By

Sarah Bernardis

Submitted to the Department of Materials Science and Engineering
on October 15th, 2012 in Partial Fulfillment of the
Requirements for the Degree of Doctor of Philosophy in
Materials Science and Engineering

Abstract

Impurities are detrimental to silicon-based solar cells. A deeper understanding of their evolution, microscopic distributions, and oxidation states throughout the refining processes may enable the discovery of novel refining techniques. Using synchrotron-based microprobe techniques and bulk chemical analyses, we investigate Fe, Ti, and Ca starting from silicon- and carbon bearing raw feedstock materials to metallurgical grade silicon (MG-Si), via carbothermic reduction.

Before reduction, impurities are present in distinct micron- or sub-micron-sized minerals, frequently located at structural defects in Si-bearing compounds. Chemical states vary, they are generally oxidized (*e.g.*, Fe²⁺, Fe³⁺). Impurity concentrations are directly correlated to the geological type of quartz: pegmatitic and hydrothermal quartz have fewer impurities than quartzite. Particles containing Cr, Mn, Fe, Ni, Cu, K, and/or Zn are also detected. In carbon-bearing compounds, Ca typically follows wood veins. In wood, Fe and Ti are diffused uniformly. In contrast, charcoal samples can contain particles of Fe, Ti, and/or Ca. The overall impurity content in the pine charcoal sample is higher than in the pine woodchip, suggesting that the charcoalization process introduces unintentional contamination.

During reduction, silica evolution is analyzed in parallel to Fe. Fe is predominantly clustered in minerals which influence its oxidation state. Here, Fe is embedded in muscovite with predominance of Fe³⁺. Initially, Fe is affected by the decomposition of muscovite and it is found as Fe²⁺; as muscovite disappears, Fe diffuses in the molten silica, segregating towards interfaces. Contrary to thermodynamic expectation, Fe is oxidized until late in the reduction process as the silica melt protects it from gases present in the furnace, hence minimizing its reduction, only partially measured at high temperatures.

After reduction, the initial low- to sub- ppmw concentrations measured in the precursor quartz increase drastically in the MG-Si. The refining process is responsible for the increased contamination. Yet, most impurities are clustered at grain boundaries and a leaching process could remove them.

Electrical fragmentation and a leaching treatment are tested as a method to expose grain boundaries of “dirty” quartzite and to remove impurities. The selective fragmentation proves to be a very important step in removing impurities via leaching.

Thesis Supervisor: Kenneth C. Russell

Title: Professor Emeritus of Metallurgy and Nuclear Engineering

Acknowledgments

I crossed the finish line thanks to a handful of professors I had the luck to meet and to collaborate with throughout the last years. In chronological order: Sam Allen made me discover the beauty of the world of kinetics as well as dedicated his time to improve my graduate student experience. Ken Russell inspired me by always pointing out the most important scientific aspects and by providing broader perspectives. Tonio Buonassisi suggested and motivated this research; his contributions and scientific insights were invaluable. Marisa Di Sabatino drastically changed my life by inviting me to perform experiments with her. This thesis would have been very different without her long term vision, passion, and persistence. Merete Tangstad was always available to discuss anything from furnace thermodynamics to possible funding miracles. Her perspective both on life and the PhD experience should be written for the next generations of students. Rune Larsen, my quartz guru, without his expertise, quartz would have been a cryptic feedstock material rather than an amazing mineral.

I feel deeply indebted to Dean Blance Staton. She has been extremely supportive and always suggested brilliant solutions to colorful situations. Her wisdom and experience were irreplaceable.

To the MIT Glass Lab and to my close friends, their humor and support, infinite chats, and the many evenings spent together, Martina Poletti, Riccardo Pedersini, Anna Custo, Gabriele & Miriam Vanoni, Andrea Allais, Linda Valeri, Jon Gibbs, Mike Tarkanian, and Dana Shemuly.

A special thank you to my sister Elena, always present and supportive. You know I really mean it.

To all of you, my everlasting gratitude.

Contents

Abstract.....	- 3 -
Acknowledgments.....	- 5 -
Contents	- 7 -
List of Figures.....	- 11 -
List of Tables	- 14 -
1. Introduction	- 15 -
1.1. Motivation	- 15 -
1.1.1. Selected Impurities: Fe, Ti, and Ca.....	- 17 -
1.2. Carbothermic Reduction	- 18 -
1.3. Silica and Trace Elements during Carbothermic Reduction	- 19 -
1.3.1. Before Carbothermic Reduction	- 20 -
1.3.2. During Carbothermic Reduction.....	- 22 -
1.3.3. After Carbothermic Reduction.....	- 26 -
1.4. Scope and Structure of this Thesis	- 26 -
1.4.1. Process Description.....	- 27 -
1.4.2. Process Development.....	- 27 -
2. Characterization Methods.....	- 29 -
2.1. Quartz Section Preparation.....	- 29 -
2.2. Microscopy.....	- 30 -
2.2.1. Optical Microscopy.....	- 30 -
2.2.2. Scanning Electron Microscopy.....	- 30 -
2.2.3. Electron Probe Micro-Analyzer.....	- 31 -
2.2.4. Synchrotron Based X-ray Fluorescence.....	- 31 -
2.3. Spectroscopy	- 34 -
2.3.1. X-Ray Near Edge Absorption Structure	- 34 -
2.3.2. Fourier Transform Infrared Spectroscopy	- 35 -

2.4.	X-ray Diffraction.....	- 35 -
2.5.	Bulk Concentration Analysis	- 36 -
2.5.1.	Inductively Coupled Plasma Mass Spectrometry	- 36 -
2.5.2.	Glow Discharge Mass Spectrometry	- 37 -
3.	Before Carbothermic Reduction: Raw Feedstock Materials	- 39 -
3.1.	Raw Feedstock Materials	- 39 -
3.2.	Silicon Bearing Raw Feedstock Materials	- 40 -
3.2.1.	Pegmatitic Quartz.....	- 40 -
3.2.2.	Hydrothermal Quartz	- 41 -
3.2.3.	Quartzite.....	- 41 -
3.3.	Carbon Bearing Raw Feedstock Materials.....	- 42 -
3.4.	Impurity Distribution and Oxidation States	- 42 -
3.4.1.	Iron.....	- 43 -
3.4.2.	Titanium.....	- 45 -
3.4.3.	Calcium.....	- 47 -
3.4.4.	Elemental Co-Location and Other Impurities.....	- 48 -
3.5.	Discussion	- 49 -
3.6.	Conclusions	- 51 -
4.	During Carbothermic Reduction	- 53 -
4.1.	Hydrothermal Quartz.....	- 53 -
4.2.	Experimental Procedure	- 54 -
4.3.	Results	- 55 -
4.3.1.	Host Matrix – Silica	- 56 -
4.3.2.	Iron.....	- 58 -
4.4.	Discussion	- 64 -
4.4.1.	Effect of the Reducing Environment	- 64 -
4.4.2.	Silica Evolution.....	- 66 -
4.4.3.	Evolution of Distribution and Oxidation State of Iron	- 68 -
4.5.	Conclusions	- 71 -
5.	After Carbothermic Reduction: Metallurgical Grade Silicon.....	- 73 -
5.1.	Materials and Method.....	- 73 -

5.2. Observations.....	- 74 -
5.2.1. Quartzite.....	- 74 -
5.2.2. Metallurgical-Grade Silicon.....	- 75 -
5.2. Discussion	- 80 -
5.3. Conclusions	- 81 -
6. Process Development: Quartz Leaching.....	- 83 -
6.1. Introduction	- 83 -
6.2. Principles of Electrical Fragmentation.....	- 86 -
6.3. Materials.....	- 87 -
6.4. Experimental Procedure	- 88 -
6.4.1. Electrical Fragmentation.....	- 88 -
6.4.2. Wet Etching	- 89 -
6.5. Results and Observations	- 89 -
6.6. Conclusions	- 95 -
7. Conclusions	- 97 -
8. Future Work.....	- 99 -
Appendix A.....	- 103 -
Appendix B.....	- 109 -
Appendix C	- 115 -
Bibliography	- 127 -

List of Figures

Figure 1.1 Foreign elements in quartz can be found as a) substitutional or interstitial point defects (redrawn from Bragg 1937); b) fluid inclusions; and c) solid (mineral) inclusions.....	- 20 -
Figure 3.1 Representative optical micrographs in normal (a) and crossed polarized light (b, c) of the silicon-bearing samples: a) pegmatitic quartz; b) hydrothermal quartz; and c) quartzite.	- 40 -
Figure 3.2 Representative SEM micrographs of the carbon-bearing samples: a) pine woodchip; b) pine charcoal.-	42 -
Figure 3.3 μ -XRF maps of silicon-bearing compounds used during silicon refining. Impurities are predominantly seen in clusters, which tend to decorate structural defects. Intensity scale bars are in [atoms/cm ²] and are optimized for maximum contrast.....	- 43 -
Figure 3.4 μ -XRF maps of carbon-bearing compounds used during silicon refining (“W” stands for woodchip and “C” for charcoal). Impurity clusters can be observed in charcoal samples. Intensity scale bars are in [atoms/cm ²] and are optimized for maximum contrast.	- 44 -
Figure 3.5 Fe K-edge XANES of the Si- (a-c) and C- (d-f) bearing feedstock materials. Fe ⁰ peaks at 7110 eV (d), Fe ²⁺ at 7111.5 eV (b,c,e), and Fe ³⁺ at 7113 eV (a,c,d,e,f); peak splitting between 7111.5 and 7113 eV indicates 2+ and 3+ oxidation state mixing (c,f).....	- 46 -
Figure 3.6 μ -XRF map of a grain boundary in quartzite showing distribution of a) Fe, b) Ti, and c) Ca.	- 47 -
Figure 3.7 Impurity concentration of iron (yellow), titanium (orange), and calcium (red) in the a) Si- and b) C-bearing compounds (“W” stands for woodchip and “C” for charcoal). Results obtained from μ -XRF measurements (full color) are compared to ICP-MS analysis	- 48 -
Figure 4.1 Transmitted visible light images of the petrographic thin sections of hydrothermal quartz showing: a) the bimodal grain size distribution; b) H ₂ O-CO ₂ based fluid inclusions; and c) the presence of muscovite crystals (two examples circled in white).	- 55 -
Figure 4.2 Snapshots of the quartz being heated to 1900°C. The silica first expands (1000-1600°C) then contracts into a droplet, typical of the molten state (1900°C).....	- 56 -
Figure 4.3 Crystalline structure versus annealing temperature: silica is found as quartz in the untreated sample and at 1000°C; it transforms to a mixture of quartz, cristobalite, and molten state at 1600°C. The 1000°C and 1600°C spectra are multiplied by ten and upward shifted.	- 57 -
Figure 4.4 Room temperature reflected FT-IR spectra; the untreated quartz FT-IR spectrum is used to infer changes upon annealing in the other three spectra.	- 57 -

Figure 4.5 Transmitted visible light micrographs (a,d,g,l) and corresponding μ -XRF Fe (b,e,h,m) and K (c,f,i,n) distribution maps of untreated, annealed to 1000°C, 1600°C and 1900°C samples, collected at 10keV. The field of view for each sample is 2000 x 1000 μm^2 . The untreated sample (a) has a structure similar to the one of the sample annealed to 1000°C (d). The same is valid for the Fe-rich particles (b and e), which are seen as distinct particles, possibly co-located with muscovite ($\text{KAl}_3\text{Si}_3\text{O}_{10}(\text{OH},\text{F})_2$) crystals seen in transmitted light (Figure 1b); K-rich particles (c and f) are in fact co-located with Fe. In the sample annealed to 1600°C (g), molten silica channels (1) and cristobalite formation (2) are visible around quartz (3); at this temperature, Fe preferentially segregates towards molten features (h). At 1900°C the sample is completely molten and gas bubbles are evenly distributed (l). Fe is found only at interfaces between the gaseous phase and the glassy silica (m). In these latter samples, K mostly volatilized (i, n). - 59 -

Figure 4.6 Absolute (left axis) and relative (right axis) mass loss of both silica (a) and graphite substrate (b). In the case of silica, mass loss is caused by $\text{SiO}(\text{g})$ formation; the graphite substrate mass change is potentially caused by reaction with the reducing gas and with the silica. Lines are only an eye guide. Mass measurement errors fall within the size of the point markers. - 61 -

Figure 4.7 Iron (coded in red) segregates preferentially towards interfaces: 10keV μ -XRF maps show Fe located in Si- (coded in blue) deprived molten channels visible in the sample annealed at 1600°C (a) and in gaseous bubbles as well as along the sample interface in the sample annealed at 1900°C (c). Selected sub-regions in a) and c) are shown in the 7.3 keV μ -XRF maps b) and d), respectively. Color intensity reflects XRF counts and is optimized for maximum contrast. - 61 -

Figure 4.8 Fe pre K-edge μ -XANES peaks: Fe^{3+} peaks at 7113 eV (RT, 1600, 1900°C); Fe^{2+} at 7111.5 eV (1000°C). However, least-square linear combination fitting of the full spectra shows that at high temperatures (1600 and 1900°C) these peaks are the result of a combination of Fe^{3+} and Fe^{2+} (see Figure 4.9). - 62 -

Figure 4.9 Example of a least-square linear combination fit of the μ -XANES of one particle at 1600°C (red) and 1900°C (blue, shifted upwards): co-presence of Fe^{3+} and Fe^{2+} oxidation states is found. - 62 -

Figure 4.10 μ -XRF chemical maps of the Fe oxidation state evolution. The “Total Fe” (first row) depicts total Fe measured above the K-edge (7.3 keV). This μ -XRF map is then fitted by a XANES database comprising Fe(0), Fe(2+), and Fe(3+) species and split between “Fe(0)” (second row), “Fe(2+)” (third row), and “Fe(3+)” (forth row). See text for description. All maps measure 500 x 250 μm^2 ; intensity scale bars are in μ -XRF counts and are optimized for optical contrast. **Error! Bookmark not defined.**

Figure 4.11 Temperature dependent elemental composition of one characteristic Fe-rich particle per sample. Main differences are the presence of: Cr (untreated, 1000°C), Ca and Ti (1600°C, 1900°C). - 63 -

Figure 4.12 SEM images of the graphite substrates after being heated in $\text{CO}(\text{g})$ with SiO_2 . The first column shows the area in contact with the SiO_2 ; the second column, details of the reaction between the silica and the graphite; the third column, an area far from the reaction zone. See text for reaction description. - 68 -

Figure 4.13 Stability of the Fe oxidation state based on the oxygen fugacity. At 1600°C and 1900°C, the stability field of Fe⁰ is thermodynamically approached. Fe data from Ohmoto 1977; C-CO-CO₂ data from Jakobsson 1994 .. - 70 -

Figure 5.1 Two transmitted light images of petrographic thin sections of the quartzite used to extract the metallurgical-grade silicon discussed in this chapter. During metamorphism, quartz grains re-aligned following a shearing direction. Trails of fluid inclusions (black dots) perpendicular to the shearing direction and a foreign mineral are visible in b). - 74 -

Figure 5.2 Impurity bulk concentration analyses. Impurities in quartzite (red) are compared to the ones obtained in the MG-Si (gray). For this latter, ICP-MS (gray) analyses are compared to GD-MS (textured gray)..... - 76 -

Figure 5.3 MG-Si SEM image (a) showing several silicon grains with impurities decorating grain boundaries. A selected sub-region (b) is analyzed by EDX (c): its chemical composition shows Al and Ca co-located with Fe and with some Ti. Three different areas are analyzed (a, d, g) and the same co-location pattern is observed (c, f, i). Concentrations are in mass percent. - 77 -

Figure 6.1 Transmitted light images of petrographic thin sections of a) hydrothermal quartz; b) hydrothermal vein quartz; and c) quartzite. - 90 -

Figure 6.2 ICP-MS test blanks and b) USGS Diabase W-2 reference geomaterial. Comparison of two analytical measurements performed at different times..... - 92 -

Figure 6.3 ICP-MS analyses of the impurity concentrations in a) hydrothermal quartz, b) hydrothermal vein quartz, and c) quartzite, as the initial material (yellow) is electrically fragmented (orange), sieved (red) and finally leached. Four leaching recipes are tested (white and gray). - 93 -

List of Tables

Table 6.1 Examples of leaching recipes reported in the literature - 85 -

1. Introduction

This introductory chapter gives the theoretical background on which this thesis was thought and developed. In section 1.1, the motivation that led to this research, the impact impurities have on silicon-based solar cells, and the choice of the investigated impurities, are outlined. Section 1.2 explains the carbothermic reduction process currently used to extract silicon from raw feedstock materials. Section 1.3 provides insight on the silica host structure and on the impurities in terms of the reduction process: before (section 1.3.1.), during (section 1.3.2.), and after reduction (section 1.3.3.). The scope and the structure of the thesis are outlined in section 1.4.

1.1. Motivation

Impurities degrade silicon-based solar cell performance, reducing minority carrier diffusion length [1,2] and power output [3,4]. The problem can be simply stated in the following way: undesired impurities reduce carrier lifetime by acting as traps and recombination centers. On the other hand, impurities, when intentionally added as dopants, can be crucial to achieve proper device structure and functionality. A silicon feedstock devoid of deleterious impurities is imperative for efficient, reliable and, especially, reproducible silicon-based solar cells.

To avoid the negative effects of impurities, photovoltaic devices have traditionally been fabricated using high-purity (99.9999999%, 9N) electronic-grade silicon (EG-Si). However, their high costs and limited availability led to exploring alternatives termed solar-grade silicon (SoG-Si, 6N purity [5,6]), including modified Siemens processes and upgraded-metallurgical-grade

silicon (UMG-Si) [7]. Metallurgical-grade silicon (MG-Si, > 98%) is the starting material for UMG-Si purification.

Extraction of silicon from raw feedstocks requires carbothermic reduction, industrially performed in submerged electric arc furnaces [8,9]. Metallic impurities present in the initial raw feedstock materials [10,11], and especially within the obtained silicon and solar cells [1,5,6,12-17] are object of extensive research. Often, post-reduction silicon refining is the only method sought to reduce unwanted impurities, directing efforts to understand their behavior to a certain step of the extraction process onwards. Yet impurities are already present in the raw feedstocks and they participate in the silica reduction process.

Given the rapid growth of the silicon solar cell industry and the increasing demand for silicon feedstock with purity higher than 6N, it is essential for the silicon refining industry to investigate alternative Si-bearing raw materials. Less stringent purity requirements and novel methods to remove impurities prior to reducing the raw feedstock materials would allow overcoming availability constraints on high-purity raw feedstock compounds.

We postulate that a deeper understanding of the microscopic distributions, oxidation states, and concentrations of the impurities throughout the Si extraction process, from silicon- and carbon-raw feedstock material to MG-Si, could assist in developing more competitive and efficient refining techniques, thus improving existing processes and widening the usable feedstock to less pure materials.

1.1.1. Selected Impurities: Fe, Ti, and Ca

Iron, titanium, and calcium are the three impurities investigated in this thesis. These impurities are chosen according to their effects either on solar cell performance or during the silicon refining and ingot crystallization processes.

Iron ($[\text{Ar}] 3d^6 4s^2$) has detrimental effects on silicon solar cells: it is a fast-diffusing transition metal during solar cell processing [18]; and by introducing deep energy levels in the silicon band gap, it reduces minority carrier lifetime, resulting in a strong negative impact on cell performance [1,13]. Titanium ($[\text{Ar}] 4s^2 3d^2$) has lower diffusivity and solubility than iron [18]; even though Ti is generally less abundant than Fe, its effect on carrier lifetime is more deleterious due to the deep levels it generates in the silicon band gap [1,19,20]. Calcium ($[\text{Ar}] 4s^2$) is not considered an impurity with strong electrical activity [21], and its action in purifying silicon is actually sought during slagging [8]. However, ongoing investigations indicate that selected phase transitions in the Ca-O system can disrupt silicon refining and ingot crystallization [22,23]. It can aggregate in an oxidized form on the bottom of the submerged electric arc furnace, from where it is not easily removed. Calcium oxide (CaO) has a melting temperature of 2613°C [24], which is far higher than the melting point of pure silica (1723°C [25]). As the area underneath the electrodes generally reaches 2000-2200°C, CaO lumps accumulate modifying the heat distribution, which in turn disrupts chemical reactions leading to silicon extraction. Moreover, CaO can react with the furnace lining, potentially cracking it.

1.2. Carbothermic Reduction

As silicon is found in nature only in an oxidized state, industry reduces silica to silicon through a process known as carbothermic reduction, which utilizes C-bearing compounds as the reducing species, generally a mixture of woodchips, coal, and coke [8,10]. Quartz and quartzite are currently used as the primary Si-bearing raw feedstock material in the production of MG-Si.

Extraction is currently performed in submerged electric arc furnaces [8,9]. The overall carbothermic reaction is generally written as $\text{SiO}_2(\text{s}) + 2\text{C}(\text{s}) \rightarrow \text{Si}(\text{l}) + 2\text{CO}(\text{g})$. It summarizes a chain of reactions that occur in different locations of the furnace at different temperatures and in the presence of different chemical species. In fact, this oversimplified thermodynamic reaction is the overall description of on-going multiple kinetic reactions throughout the entire furnace. As the raw feedstock is charged (*i.e.* inserted in the furnace) and silicon metal is tapped (*i.e.* extracted from the furnace bottom), by-products of the process are left in the furnace and act as reactants for the next reactions involving the new charged material flowing downwards. Furnace and electrode design create heat gradients, which in turn will generate mass flow gradients; these, finally, dictate reactant availability. Due to these gradients, material flowing downwards near the electrodes will be faster compared to colder material accumulated near the sides of the furnace. Reactions can be analyzed with respect to different variables: distance from the electrodes can be considered on a horizontal cross-section of the furnace; variable descent times on a vertical-cross section. The overall reaction captures all these phenomena. Detailed explanation of all reactions occurring in a submerged electric arc furnace, specifically dedicated to silicon refining, can be found in [9].

Several theoretical [9,26-28] and experimental [29-32] studies concentrated on the Si-C-O system and proposed chemical reactions during silica reduction. However, industrial submerged electric arc furnaces operate outside thermodynamic equilibrium conditions in dynamic cycles of charging, stocking (*i.e.* breaking the crust formed at the top of the furnace), and tapping. These cycles influence chemical speciation, temperature, and pressure [33,34]. Industrial furnaces are counter-current reactors where gases produced in the crater zone ascend reacting with the new, colder charge before re-descending in the crater zone [35]. Even though a steady state should be reached between ascending and descending species, several authors reported difficulties in applying thermodynamic knowledge to obtain silicon metal from silica and carbon materials in a laboratory scale furnace ([27] and references therein).

1.3. Silica and Trace Elements during Carbothermic Reduction

Si-bearing raw feedstock materials are charged at the top of the furnace (~1000°C) and they descend towards the bottom (~2000-2200°C) undergoing phase transitions while also chemically reacting with other species they encounter. At atmospheric pressure, there are four crystalline phases of silica and these are stable at different temperatures: α -quartz, β -quartz, hexagonally close packed (HP)-tridymite, and β -cristobalite [25]. Most raw feedstock materials are found in nature as α -quartz. During the carbothermic extraction process, before reaching the molten state, the initial α -quartz can transform to the other three polymorphs.

Trace elements originally embedded in the α -quartz follow the same path in the furnace until they are liberated from the host crystal. Volatile trace elements escape with the out-diffusing gases, while other trace elements, such as transition metals, reach the bottom of the furnace

where they become intermixed with the liquid silicate. After reduction, impurities are tapped from the furnace with the silicon.

1.3.1. Before Carbothermic Reduction

The silica polymorph crystal structures are comprised of Si and O atoms covalently bonded in tetrahedra. The room temperature stable silica polymorph is α -quartz. It has a trigonal crystal structure, which belongs to the $P3_121$ or $P3_221$ (enantiomorphic) space groups [25], depending on the handedness (left, right, respectively [36]) of the tetrahedral helical structure; lattice parameters are $a = 4.70 \text{ \AA}$ and $c = 5.25 \text{ \AA}$ [37].

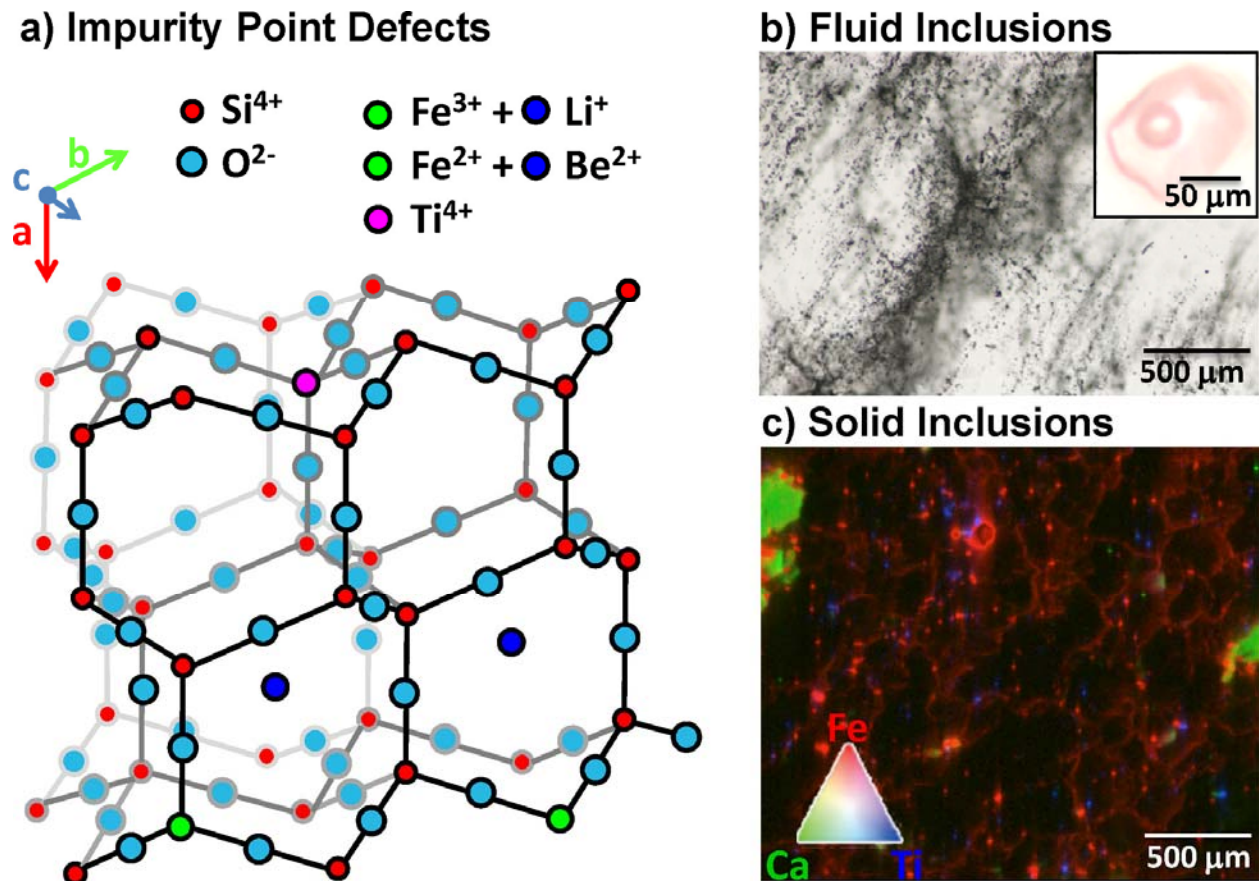


Figure 1.1 Foreign elements in quartz can be found as a) substitutional or interstitial point defects (redrawn from Bragg 1937); b) fluid inclusions; and c) solid (mineral) inclusions.

Trace elements in α -quartz can be incorporated as interstitial or substitutional point defects (Figure 1.1a), fluid inclusions (Figure 1.1b), and solid (mineral) inclusions (Figure 1.1c), such as foreign minerals grown inter- or intra- quartz grains.

Many trace elements can be accommodated as point defects (H, Li, Be, B, Na, Mg, Al, P, K, Ca, Ti, Cr, Mn, Fe, Cu, Ge, Rb, Sr, Ba, Pb, and U [38]); however, their presence is severely limited by the strong Si-O covalent bond. Monovalent (Li^+ , K^+ , Na^+) and divalent (Be^{2+}) ions generally prefer interstitial lattice sites, such as open spaces either in the channels parallel to the c axis (monovalent) or structural defects (mono- and divalent). Divalent atoms are also found as substitutional, occupying Si^{4+} vacancies. Trivalent (B^{3+} , Al^{3+} , Fe^{3+}), tetravalent (Ti^{4+} , Ge^{4+}), and pentavalent (P^{5+}) ions are generally found substituting Si^{4+} . For charge neutrality of the overall crystal, trivalent ions can either form coupled substitutions with pentavalent ones; or are balanced by the presence of nearby monovalent ions. A linear proportionality of trivalent and monovalent ion concentrations ($\text{Al}+\text{Fe} : \text{Li}+\text{Na}+\text{K}$) was suggested [39], yet the role of amphoteric interstitial H was ignored, leaving this hypothesis open to further investigations. Impurity content depends on the specific geological formation of the quartz being considered. Higher crystallization temperatures produce higher purity quartzes than lower crystallization temperatures, suggesting that the solid solubility of extraneous element might be greater at higher temperatures [40]. As the variables affecting natural geological systems are too vast to be considered all simultaneously (*e.g.*, temperature, pressure, pH, all impurities present and their initial concentrations, etc.), controversial relationships between crystallization temperature and impurity solubility are often encountered in geological studies.

Impurity solid solubility is very low because of the strong Si-O covalent bond. Most trace elements segregate to structural defects such as grain boundaries [41] and form minerals with compositions dictated by the elements present at the time of crystallization. Upon addition of impurity elements, formation of fayalite (Fe_2SiO_4) is predicted in the FeO-SiO₂ quasi-phase diagram [42]; contrary, the TiO₂-SiO₂ phase diagram shows no intermediate phase between the TiO₂ and SiO₂ end members [43]; while wollastonite (CaSiO_3) is the first phase formed upon Ca addition to pure SiO₂ [44]. However, impurity concentrations in raw feedstock material relevant for SoG-Si production rarely are high enough to form a silicate. Iron is generally found in solid inclusion such as iron oxides or Fe-rich micas, never in fluid inclusions; titanium in rutile (TiO₂) needles; while calcium might be found either in minerals (*e.g.* CaTiO_3) or in fluid inclusions.

Limited information is available on impurities embedded in raw feedstock materials of industrial relevance [10,11]. Industry selects raw feedstock materials based on bulk chemical analyses rather than microscopic information; moreover, dressing techniques used to remove impurities and foreign minerals prior to utilization are generally confidential. As the impurities present in the initial material dictate the purity of the silicon metal extracted, a deep understanding of impurities is crucial in order to improve the currently used processes.

1.3.2. During Carbothermic Reduction

The stability field of α -quartz ends at 573°C, when entering the stability field of β -quartz [45]. As soon as α -quartz is charged in the furnace, it experiences ~1000°C and it immediately undergoes a fast displacive phase transition to β -quartz. This transformation involves development of micro-domains delineated by Dauphiné twinning, which vibrate and decompose [46]. Upon cooling or quenching, β -quartz readily transforms to α -quartz, either via formation of

Dauphiné twinning [46], or, according to later studies, due to the decrease of thermally induced structural disorder, dominant in β -quartz [47]. β -quartz has a hexagonal structure with space group $P6_422$ or $P6_222$ [25], and lattice parameters $a = 5.01 \text{ \AA}$ and $c = 5.47 \text{ \AA}$ [48]. The nominal stability field of β -quartz is between 573°C and the onset of HP-tridymite formation, at 867°C [49]. Transformation between these two phases is reconstructive and kinetically slow. Some authors claim mineralizing agents (*e.g.* Na, K) are required to initiate HP-tridymite crystallization [50], while others claim β -quartz directly transforms to β -cristobalite at $\sim 1050^\circ\text{C}$ [51]. More recent studies, performed on natural quartz, claim formation of HP-tridymite was never observed [11]. HP-tridymite, with a triclinic crystal structure, belongs to space group $P6_3/mmc$ with lattice parameters $a = 5.03 \text{ \AA}$ and $c = 8.22 \text{ \AA}$ [52]. HP-tridymite transforms to β -cristobalite at 1470°C [25]. If crystallization of HP-tridymite does not initiate at 867°C , β -quartz melts heterogeneously at a metastable melting temperature of 1025°C [53]; β -cristobalite can nucleate via impurities and grow at the expense of the fused silica [54]. β -cristobalite has a cubic crystal structure with $Fd\bar{3}m$ symmetry and lattice parameter $a = 7.16 \text{ \AA}$ [48]. β -cristobalite melts to silica liquid at 1727°C [25].

All phase transition temperatures can be affected by the presence of impurities. Generally, as a multi-component system (silica – trace element), the impurity concentration affects the melting temperature, which in principle can be as low as the eutectic temperature of the multi-component system. Onset of heterogeneous melting occurs locally along grain boundaries [55,56], where impurities preferentially segregate [41] and cluster in foreign minerals.

Impurities behave in β -quartz as previously described for α -quartz. In the high temperature silica polymorphs (HP-tridymite and β -cristobalite), the crystallographic framework is more spacious

and able to accommodate more easily single and especially coupled impurity substitutions. In fact, impurity concentration analyses reveal higher concentrations in these polymorphs than in the lower temperature ones [25].

In high temperature silica polymorph grains, diffusivity of trace elements depends on cation charge. As a general trend, diffusion of univalent cations is faster than divalent cations; similarly, tetravalent cations are found to be slower diffusers than trivalent ones [57]. For example, Ca^{2+} has activation energy of 285 ± 8 kJ/mol and pre-exponential factor of $1.0 \cdot 10^1$ m²/s in the temperature range 600-800°C (original data [58] could not be found; values are reported by [57]). In the temperature range 700-1150°C, Ti^{4+} diffusion in quartz has an activation energy 283 ± 26 kJ/mol and a pre-exponential factor $2.65 \cdot 10^{-8}$ m²/s [59]. Fe^{2+} and Fe^{3+} diffusivity data could not be found; however, diffusion of divalent and trivalent cations is expected to be faster than diffusion of tetravalent cations. Since diffusion data is available for Ca^{2+} and Ti^{4+} it is here assumed that diffusion of Fe^{2+} and Fe^{3+} should be slower than Ca and faster than Ti. A schematic interpretation is provided by [60], where diffusion coefficients are plotted versus temperature for cations of different charge.

Intra-granular diffusion is one diffusion path trace elements can follow. Inter-grain, phase boundaries, and diffusion along fluid inclusion trails are other diffusion paths available to trace elements. A description of diffusion in minerals and melts can be found in [61]. Diffusion along grain boundaries is generally a few orders of magnitude faster than within mineral grains. However, the chemistry of grain boundaries can be very different compared to the adjacent quartz grains and impurity diffusion might be affected by co-presence of other trace elements.

When considering grain boundary diffusion, impurities affect each other by enhancing or hindering diffusivity; mechanisms are still under debate [62].

When the host silica melts, it forms an extremely viscous polymeric melt which is not easily modified by the addition of small amounts of foreign trace oxides. When considering the $\text{Fe}^{2+}\text{O}-\text{SiO}_2$ [42], $\text{Ca}^{2+}\text{O}-\text{SiO}_2$ [44], $\text{Fe}_2^{3+}\text{O}_3-\text{SiO}_2$ [63], as well as $\text{Ti}^{4+}\text{O}_2-\text{SiO}_2$ [43] phase diagrams, a two-liquid region is present at high temperatures. Description of such a system can be found in [64]. Trace elements homogeneously intermix with liquid silicon only after silica reduction. A thermodynamic study of Fe and Ti in molten silicon can be found in [65]; while Ca is presented in [66].

Rather than impurities, previous publications focused on physical [30] and thermo-mechanical properties [11] of the raw feedstock materials, as these properties determine how well the materials will behave in the furnace. They are fundamental to predict whether quartz will explode upon heating or whether it will reach the electrode tips before fully melting. In the former case, exploded quartz produces fines; in the latter, the molten state can be reached higher up in the furnace. In both cases, the permeability of the charge decreases and gas flow is obstructed [11] disrupting optimal industrial operational conditions.

Impurity concentrations are analyzed before and after reduction without linking the behavior of impurities within the reduction process itself. An impurity-based approach has never been considered.

1.3.3. After Carbothermic Reduction

Silicon has a diamond cubic crystal structure that is extremely closed to incorporation of foreign atoms. Impurities can be found as point defects, aggregated in complexes, or as second-phase precipitates. Impurity segregation towards grain boundaries and structural defects decreases crystal disorder and relieves strain fields associated with foreign crystals embedded within the host matrix.

For example, Fe can be found as an interstitial point defect paired with shallow acceptors (*e.g.* B, Al, In, Ga), shallow donors (*e.g.* P, As), or other impurities; in silicide FeSi₂ in a metallic state [67]; or sometimes in an oxidized form, Fe₂O₃ [68,69], co-located with slow diffusing impurities (*e.g.* Ca, Ti, Cr, Mn, Ni) [70]. Reviews on Fe in silicon can be found, for example, in references [18,21,67,70].

1.4. Scope and Structure of this Thesis

The efficiency of silicon-based solar cells is limited by the presence of unintentional impurities, many of which can be removed during an expensive silicon feedstock refining process (*e.g.*, the Siemens process). A deeper understanding of the evolution of impurities, their distribution, and oxidation states throughout the refining processes may enable the discovery of novel removal techniques, especially at the primary stages of the refining process.

The three main characterization methods used are two microscopic analytical techniques, synchrotron-based X-ray fluorescence microprobe and X-ray absorption near edge spectroscopy, and a bulk chemical analysis technique, inductively-coupled mass spectrometry. These are presented in Chapter 2 along with all other experimental details.

1.4.1. Process Description

The scope of the first part of the thesis is to observe and evaluate the behavior of specific detrimental impurities in industrially relevant raw feedstock materials, and to follow them throughout the reduction process up to MG-Si. Towards developing lower-cost methods of silicon refining appropriate for the solar industry, we propose to study distributions, chemical states, and concentrations of impurities at each step along the SoG-Si refining processes. Both Si- and C-bearing raw feedstock materials are presented in Chapter 3; silica during reduction is analyzed in Chapter 4; the extracted silicon after reduction is investigated in Chapter 5.

To achieve this research objective, a strong geological background for the Si-bearing compounds, and some biological knowledge for C-bearing compounds needs to be acquired. The intention is to fuse expertise from different fields to gain understanding and to predict outcome of newly proposed refining techniques.

1.4.2. Process Development

The second research objective is to use the knowledge gained on precise microscopic states, distributions, and concentrations of impurities in raw feedstock materials to propose and to test novel impurity extraction methods, thus improving the refining process and ultimately solar cell material quality. A selective fragmentation technique, which exposes raw feedstock grain boundaries, followed by leaching is presented in Chapter 7. Conclusions and future research possibilities are presented in Chapters 8 and 9, respectively.

2. Characterization Methods

This chapter summarizes all the techniques and equipment used to characterize the samples discussed later. As many of these techniques are standard, only a brief description of sample preparation and of the equipment used is provided. Details are given only for techniques less common within the literature of this field of research.

2.1. Quartz Section Preparation

For the characterization methods employed in this thesis, 30 μm , 200 μm and 300 μm sections of the samples were needed.

30 μm thin sections with a 1 μm finish were prepared according to standard petrographic procedures either by Spectrum Petrographics, Inc (Vancouver, WA, USA) or by the Geology and Mineral Resources Engineering Department at the Norwegian University of Science and Technology (NTNU, Trondheim, Norway). 200 μm thick quartz sections were free standing, double side polished with a 1 μm finish; the thickness was chosen in agreement to investigations performed by [71]. These sections were prepared at NTNU and were investigated in Chapters 5 and 6. A detailed description of the 300 μm thick section preparation, tailored to minimize metallic contamination, is described in Appendix A. These thick sections were prepared by Spectrum Petrographics, Inc and were used primarily for synchrotron based investigations presented in Chapter 4.

2.2. Microscopy

Three different types of microscopy techniques were used: optical, electron, and X-ray based. The first one, optical microscopy, was essential to characterize geological samples; the second one, scanning electron microscopy and electron micro-analyzer, to evaluate morphology as well as chemical composition of surfaces; the third one, synchrotron based micro-focused X-ray fluorescence, to evaluate elemental composition of specimens with high resolution.

2.2.1. Optical Microscopy

Polished 30 μm thin sections were investigated by reflected light and by transmitted cross-polarized light microscopy using a Nikon Eclipse E600 microscope with LUPan objectives at maximum 50x total magnification (Nikon Metrology NV, Leuven, Belgium). A 2 megapixel SPOT Insight IN320 digital camera in combination with a SPOT software (Diagnostic Instruments Inc, Sterling Heights, MI, USA) allowed taking and recording images in real time.

2.2.2. Scanning Electron Microscopy

Surfaces of C-bearing specimens, either C-bearing raw feedstock materials (Chapter 3) or graphite substrates (Chapter 4), were evaluated by scanning electron microscopy (SEM). Secondary electron images provided morphological insight before other investigations were performed, such as micro-focused X-ray fluorescence. Backscattered electron images provided insight on surface compositional differences. In either case, no sample preparation was necessary.

C-bearing specimens (Chapter 3) were evaluated with a Zeiss EVO 55 Environmental SEM (Carl Zeiss MicroImaging, LLC, Thornwood, NY, USA) available in the Center for Nanoscale Systems, Harvard University (Cambridge, MA, USA). Graphite substrates (Chapter 4) were evaluated with a field emission SEM Hitachi SU6600 (Hitachi High-Technologies, Europe GmbH, Krefeld, Germany) available in the Department of Materials Science, NTNU.

2.2.3. Electron Probe Micro-Analyzer

Two different types of samples were investigated with an electron-probe micro-analyzer (EPMA): quartz samples (Chapters 3 and 6) and MG-Si (Chapter 5). The former were 30 μm thin quartz sections prepared as previously described. The latter was an MG-Si surface polished with SiC Struers papers down to a grit size of 5 μm ; then with a polishing diamond spray (DP-Spray M by Struers) and ethyl alcohol to 3 and 1 μm final polishing pads.

A JEOL JXA-8500F (JEOL(Skandinaviska)AB, Sollentuna, Sweden), in the Department of Materials Science at NTNU, was used to collect chemical maps of the samples. This tool is a thermal field EPMA with submicron SEM capability integrated with X-ray analysis. Having a 5 wavelength dispersive X-ray spectrometers (WDS) and an energy dispersive X-ray spectrometer (EDS), it can analyze 5 elements WDS and 16 elements EDS, while collecting backscatter or secondary electron images.

2.2.4. Synchrotron Based X-ray Fluorescence

To determine Fe- spatial distribution, oxidation state, and elemental co-location, we employed micro-focused X-ray fluorescence ($\mu\text{-XRF}$) mapping (Chapters 3 and 4), and chemical mapping [72] (Chapter 4). Chemical mapping identifies oxidation states present by collecting $\mu\text{-XRF}$

maps at specific energies, chosen to maximize pre K-edge feature differences, characteristic of the element under investigation [73-75]. These synchrotron based “photon in, photon out” [72] techniques have low Bremsstrahlung background providing orders of magnitude higher bulk sensitivity than electron-based techniques [76,77] and are capable of characterizing the spatial distribution and chemical nature of nm-sized clusters within cubic millimeters of insulating material [72]. In the past, they have been successfully applied to study elemental distributions in non-conductive rocks and minerals [78], wood samples [79], as well as metallic impurities in multicrystalline silicon (mc-Si) solar cell materials [12,80].

While investigating raw feedstock materials (Chapter 3), different sample preparations were applied according to the type of the material investigated. Si-bearing compounds were cut with a diamond saw blade, polished with SiC paper, and cleaned in ultrasonic baths of acetone, ethanol, and isopropanol. They were then stored in a clean (metal-free) environment until measurements at the synchrotron. C-bearing compounds were either originally provided in small cubes (1 cm³), which were cleaved along the wood veins in a clean, metal free, environment, followed by immediate X-ray microprobe measurements to avoid contamination, or they were provided in small chunks; in this latter case, one piece per batch demonstrating a flat area was used for synchrotron measurements.

For μ -XRF maps presented in Chapter 3, we used beamline 10.3.2 of the Advanced Light Source (ALS) at Lawrence Berkeley National Laboratory (Berkeley, CA). A detailed description of this beamline can be found in [81]. Large area maps were collected at 10 keV incident X-ray beam, 15 x 6 μm^2 beam spot size and 30 x 30 μm^2 pixel size using a Canberra seven-element Ge solid-state detector; high-resolution maps were collected with a 7.3 keV X-ray beam, 6 x 6 μm^2 beam

spot size, and $7 \times 7 \mu\text{m}^2$ pixel size. Fluorescence emission counts were collected for Si, P, K, Ca, Ti, Cr, Mn, Co, Fe, Ni, Cu and Zn. For higher-resolution maps, also discussed in Chapter 3, we used beamline 2-ID-D at the Advanced Photon Source (APS) at Argonne National Laboratory (Argonne, IL), with 10 keV incident beam, a 200 nm diameter spot, and a silicon drift detector. A detailed description of this beamline can be found in [82].

Two National Institute of Standards and Technology (NIST) standards (NIST 1833 and NIST 1832) were measured to convert μ -XRF counts into micrograms per square centimeter ($\mu\text{g}/\text{cm}^2$). Volumetric concentrations ($\mu\text{g}/\text{cm}^3$) were obtained by dividing the map concentration ($\mu\text{g}/\text{cm}^2$) by the X-ray attenuation length (cm). No volumetric concentration could be estimated for the C-bearing compounds, as the conversion between areal and volumetric concentrations requires knowledge of matrix density and porosity. The algorithm used to convert from μ -XRF counts to ppmw is described in Appendix B. A detailed quantitative analysis description can be found in [83] and references therein.

For the investigation presented in Chapter 4, sample preparation has been described in detail in Appendix A. X-ray microprobe analyses were carried out only at ALS beamline 10.3.2 [81]. One large $2000 \times 1000 \mu\text{m}^2$ overview μ -XRF map was collected per sample using a 10 keV incident X-ray beam, a $6 \times 6 \mu\text{m}^2$ beam spot size, $5 \times 5 \mu\text{m}^2$ pixel size. Fluorescence emission counts were collected for Si, P, K, Ca, Ti, Cr, Mn, Co, Fe, Ni, Cu and Zn. Prior to Fe chemical mapping, the energy calibration was carefully checked using an elemental foil first derivative set at 7110.75 eV [36]. Fe chemical mapping was performed on 3 to 5 regions of interest, $500 \times 250 \mu\text{m}^2$ each, chosen from the larger 10 keV map. For each region, a set of five μ -XRF maps (with $6 \times 6 \mu\text{m}^2$ beam spot size, and $5 \times 5 \mu\text{m}^2$ pixel size) were collected at five different energies: pre

K-edge background (7100 eV), Fe⁰⁺ (7110 eV), Fe²⁺ (7113 eV), Fe³⁺ (7117.5 eV), and above K-edge total Fe (7310 eV) [74,75]. Each map was deadtime corrected; sample drifting effects between maps were minimized by registering each map to the 7117.5 eV map. Fe valence state maps were finally obtained by fitting each sequence of maps with a X-ray absorption near edge spectroscopy database comprised of Fe⁰ (Fe foil), Fe²⁺ (moldavite), and Fe³⁺ (mauna loa volcanic glass) spectra recorded at ALS beamline 10.3.2 and relevant to this specific system.

2.3. Spectroscopy

Two different spectroscopy techniques were used. The first one, X-ray absorption near edge structure, allowed identifying oxidation states of selected particles. The second one, Fourier-transform infrared spectroscopy, was of interest to evaluate carbon presence (Chapter 4) in the specimens, as well as geological quartz differences (Chapter 6).

2.3.1. X-Ray Near Edge Absorption Structure

Oxidation states of selected impurity clusters, specifically Fe-, Ti- and Ca-rich particles, were determined by X-ray absorption near-edge structure (μ -XANES) spectroscopy. These measurements were performed at ALS beamline 10.3.2 using a Si(111) monochromator with energy resolution less than 1 eV [81]. K-edge absorption spectra were collected in fluorescence mode, up to 300 eV above the edge, on several spots of interest. Spectra were calibrated using elemental foil first derivative set at 7110.75 eV (Fe), 4966.40 eV (Ti) and 4132.2 eV (Sb for Ca) [84]. Spectra were deadtime corrected, pre-edge background subtracted, and post-edge normalized using standard procedures [85]. Least-square linear combination fitting of the Fe K-edge spectra was performed in the 7010-7410 eV range using a large public database of well

characterized Fe X-ray absorption spectra standards [75] and fine features in the pre-edge region of each spectra was used to infer oxidation state [75,86-88]. μ -XANES was also used to prove the validity of the chemical mapping method, by analyzing particles within the regions scanned in the μ -XRF maps. μ -XANES linear combination fits are subject to errors originating from grain orientation effects and from the fitting procedure itself as described in [89]; the error on the percentages of species present is estimated to $\pm 10\%$. All μ -XANES processing was performed using a suite of custom programs, based on LabVIEW (National Instruments, Austin, TX, USA) software, available at the beamline.

2.3.2. Fourier Transform Infrared Spectroscopy

A Thermo Nicolet 6700 Fourier Transform infrared (FT-IR) spectrometer, with a DTGS-TEC detector ($11000 - 375 \text{ cm}^{-1}$) and a KBr beam splitter (Thermo Scientific, Waltham, MA, USA), was used with a 4 cm^{-1} spectral resolution. Spectra were collected using OMNIC software in the range $400 - 4000 \text{ cm}^{-1}$ wavelength. All measurements were performed at room temperature.

FT-IR was used *to characterize 300 μm thick sections* in reflected mode (Chapter 4). Collected spectra were averaged over 128 scans to minimize signal to noise ratio and background subtracted. $200 \mu\text{m}$ thick quartz sections were evaluated in transmission mode (Chapter 6). Spectra were averaged over 64 scans, corrected for H_2O and CO_2 and background subtracted.

2.4. X-ray Diffraction

X-ray diffraction was used in this thesis to understand solely in a qualitative way crystallographic phases present in quartz samples (Chapter 4). Analyses were performed in the

Department of Materials Science at NTNU. 300 μm thick sections are evaluated using a Bruker D8 Advance X-ray diffractometer (Bruker AXS GmbH, Karlsruhe, Germany) with $\text{CuK}\alpha$ radiation in the range $18\text{-}80^\circ 2\theta$ and a 0.016° step size. Spectra were recorded with a Vântec PSD detector. No quantitative analysis was attempted on spectra collected from this tool, not optimized for silica polymorph differentiation.

2.5. Bulk Concentration Analysis

Bulk impurity concentrations can be measured by two different analytical techniques, inductively coupled plasma mass spectrometry and glow discharge mass spectrometry. The former one is mostly used to analyze raw feedstock materials and silicon, the latter only for silicon as a conductive material is required. The former one was the primary technique used to analyze all samples investigated throughout this thesis.

2.5.1. Inductively Coupled Plasma Mass Spectrometry

Inductively coupled plasma mass spectrometry (ICP-MS) was employed to measure bulk impurity concentrations. Due to the complexity of this technique, several facilities were utilized. Chronologically, these were: Sintef Materials and Chemistry (Trondheim, Norway), Norwegian Crystallites (Drag, Norway), Metron Tech (Burlingame, CA, USA), and the facility in the Chemistry Department at NTNU. Results from Sintef Materials and Chemistry were discarded after performing a round robin test with Norwegian Crystallites: contamination during sample preparation was leading to unreliable results. Results of the round robin test are summarized in Appendix C. Metron Tech performed analyses of samples presented in Chapter 3; data presented in Chapters 5 and 6 was obtained in the NTNU facility.

The NTNU academic laboratory allowed testing and optimizing each process step, from quartz powder preparation, to digestion, dilution, and control sample practice. A detailed description is summarized in Appendix C:

- *Cleaning process and powder preparation:* an initial cleaning process of the quartz pieces followed by fragmentation into smaller lumps by WC jaw crushing; sample powder was then prepared by a) WC vibratory disc milling (Chapter 5); b) agate mortar (Chapter 6); c) electrical fragmentation (Chapter 6).
- *Quartz digestion recipes:* recipes were tailored for quartz powders and to enhance their digestion an UltraCLAVE (Milestone S.r.l., Sorisole, BG, Italy) microwave digestion system was used.
- *Analyses control processes:* along with the samples of interest, each analytical run was paralleled by analyses of blank test tubes to evaluate unintentional contamination, and by analyses of a geochemical reference standard material, Diabase W-2, provided by the U.S. Geological Survey (USGS, Denver, CO, USA).

Analyses were performed with a in a Thermo Scientific Element 2 high resolution Sector Field ICP-MS (Thermo Scientific, Bremen, Germany).

2.5.2. Glow Discharge Mass Spectrometry

Only MG-Si samples (Chapter 5) were examined by glow discharge mass spectrometry (GD-MS). Flat MG-Si surfaces were prepared by polishing with SiC papers down to a polish of 300 μm . Samples were rinsed with acetone and deionized water. Bulk chemical composition was measured with a double focusing Thermo Scientific ELEMENT GD tool (Thermo Scientific,

Bremen, Germany) with ppbw resolution available in the Department of Materials Science and Engineering, NTNU. Before starting the quantitative measurement, samples were pre-sputtered to remove a surface layer ($\sim 10 \mu\text{m}$) along with eventual contamination. The sputtered area of each analysis was about 8 mm in diameter. Each sample was analyzed three times and the average is provided. More details of the GD-MS method can be found in reference [90].

3. Before Carbothermic Reduction: Raw Feedstock Materials

Using synchrotron-based analytical microprobe techniques and bulk chemical analyses, we determine micron scale elemental composition, spatial distribution and oxidation state of impurities in selected Si- and C- bearing raw feedstock materials. Investigated Si-bearing compounds are pegmatitic quartz, hydrothermal quartz and quartzite. Micron-scale clusters containing Fe, Ti, and/or Ca are frequently observed at structural defects in oxidized states at grain boundaries and other structural defects, and in bulk concentrations equivalent to ICP-MS measurements. Investigated C-bearing compounds are pine wood, pine charcoal, and eucalyptus charcoal. Clustered metals are observed only in the charcoal samples. These results are presented in [91].

Impurity clustering implies that industrial processing could be adapted to take advantage of this “natural gettering” phenomenon, expanding the usable range of raw feedstock materials to dirtier, cheaper, and more abundant ones, currently underexploited for SoG-Si production as will be discussed in Chapter 6.

3.1. Raw Feedstock Materials

Three quartz-bearing and four carbon-bearing feedstocks were analyzed. Raw feedstock choice is limited by the availability of relevant industrial samples rather than completeness.

3.2. Silicon Bearing Raw Feedstock Materials

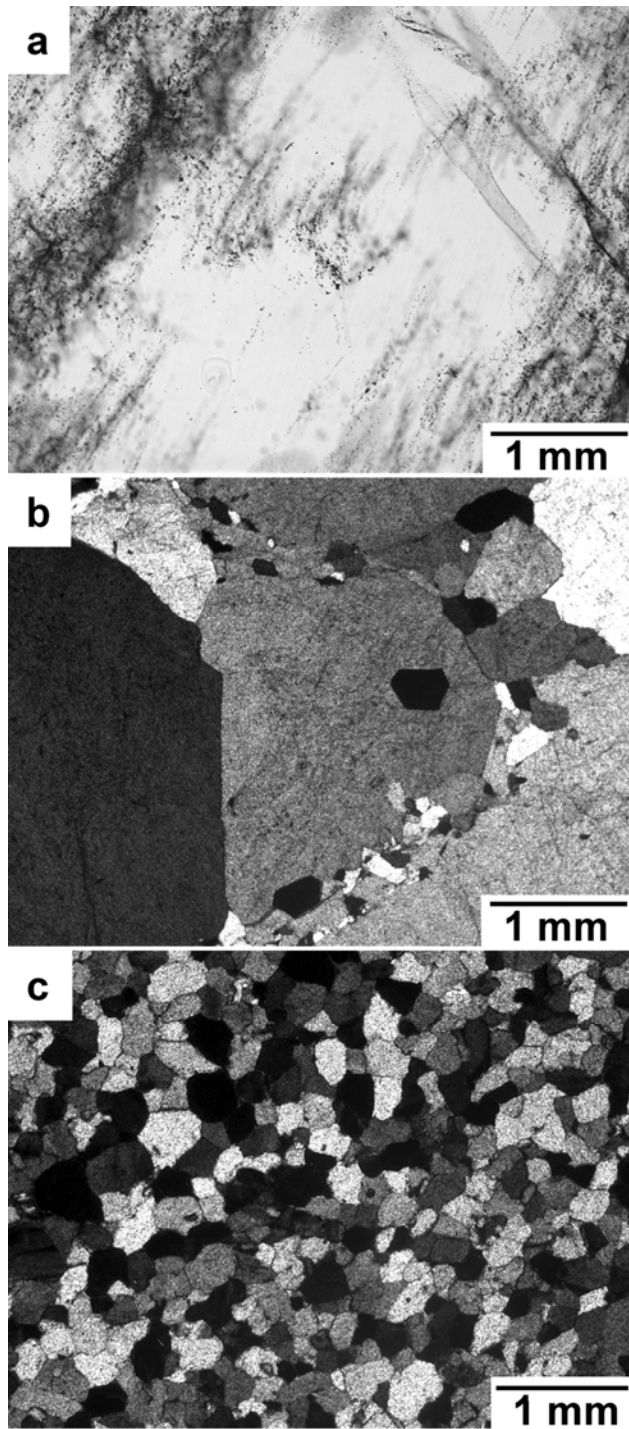


Figure 3.1 Representative optical micrographs in normal (a) and crossed polarized light (b, c) of the silicon-bearing samples: a) pegmatitic quartz; b) hydrothermal quartz; and c) quartzite.

Impurity distribution in Si-bearing feedstock materials is governed by geological formation processes, summarized below and described in detail in Refs. [38,92].

3.2.1. Pegmatitic Quartz

Pegmatitic quartz is an igneous rock-forming mineral. Quartz crystallizes from 500-700°C in a volatile-rich silicate melt yielding fast, long-range diffusion of Si and O ions but few crystal nuclei, resulting in large quartz crystals (cm- to m- scale) [13]. The same long-range diffusion also encourages foreign elements (*i.e.* potentially harmful impurities) to form distinct phases rather than being incorporated in the quartz lattice [13,14].

Pegmatitic quartz shows mm-wide milky-white coloured bands separated by transparent zones, indicating trails of secondary fluid inclusions (Figure 3.1a). Grains are centimeter-sized; structural

defects, fractures and grain boundaries are visible, while other optically-identifiable minerals are rare.

3.2.2. Hydrothermal Quartz

Hydrothermal quartz precipitates directly from aqueous fluids rich in salts, silica ions, and minor compounds. The hydrothermal fluids govern impurity concentration, which is found to range from less than 40 parts per million (ppm) to hundreds [93]. Occasionally, low temperature (300–400°C) hydrothermal fluids infiltrate previously crystallized quartz, whether pegmatitic, hydrothermal or metamorphic, re-crystallizing it to excellent quality [38,92].

Hydrothermal quartz has a milky-white colour due to a high concentration of microscopic fluid inclusions with aqueous saline solutions. A variety of grain sizes are observed (Figure 3.1b); polygonal grains with subgrain formation (*i.e.*, finer-grained crystals along grain boundaries) and grain overgrowth imply partial re-crystallization. Inter- and intra-granular fractures are common; other minerals (*e.g.*, feldspars) are rarely visible.

3.2.3. Quartzite

Quartzite is formed by metamorphosis, typically of sedimentary sand deposits. Unconsolidated quartz-rich sediments are buried and heated during orogenic events and amalgamated into a solid rock at temperatures of 300–700°C and pressures higher than 4000 bars [94]. Contrary to hydrothermal and pegmatitic quartz, foreign minerals comprise several percents of the sediments also re-crystallize during this process, resulting in high impurity concentrations [94], both in the quartz lattice structure and as minute minerals along grain boundaries.

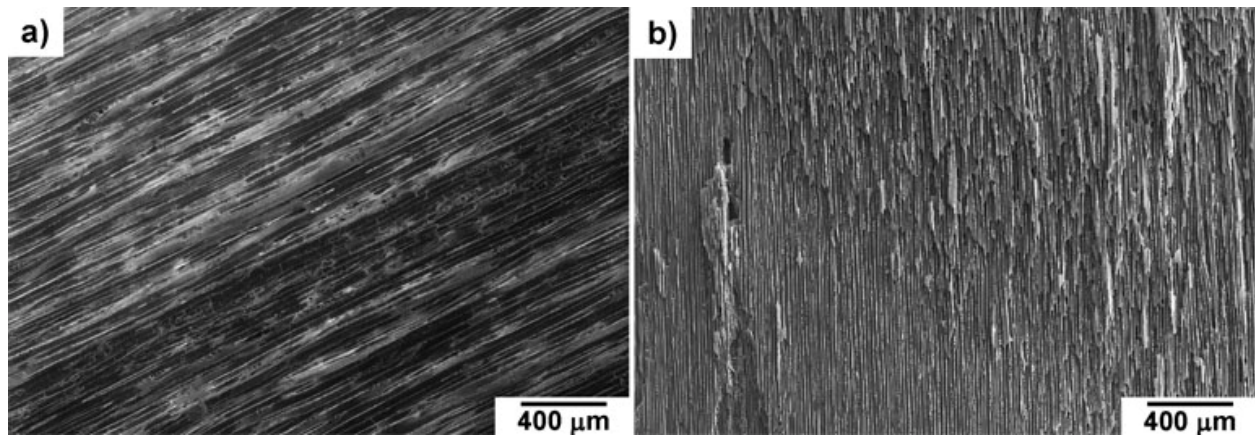


Figure 3.2 Representative SEM micrographs of the carbon-bearing samples: a) pine woodchip; b) pine charcoal.

Quartzite is brown in colour; quartz crystals are medium-grained with discernible grains of foreign minerals (Figure 3.1c); copresence of well-defined rounded or sharp edges and grain overgrowth imply local re-crystallization. Micaceous and other minerals are visible along grain boundaries.

3.3. Carbon Bearing Raw Feedstock Materials

We investigated four carbon-bearing raw feedstocks: pine wood (Figure 3.2a), pine charcoal (Figure 3.2b), Brazilian eucalyptus charcoal [95], and an Indonesian charcoal mixture of several wood types [96]. The pine wood chip is the precursor of the pine charcoal; details of an analogous charcoal formation process can be found in [96].

3.4. Impurity Distribution and Oxidation States

In the following, impurity distributions, oxidation states, and concentrations are organized by element rather than by feedstock material type.

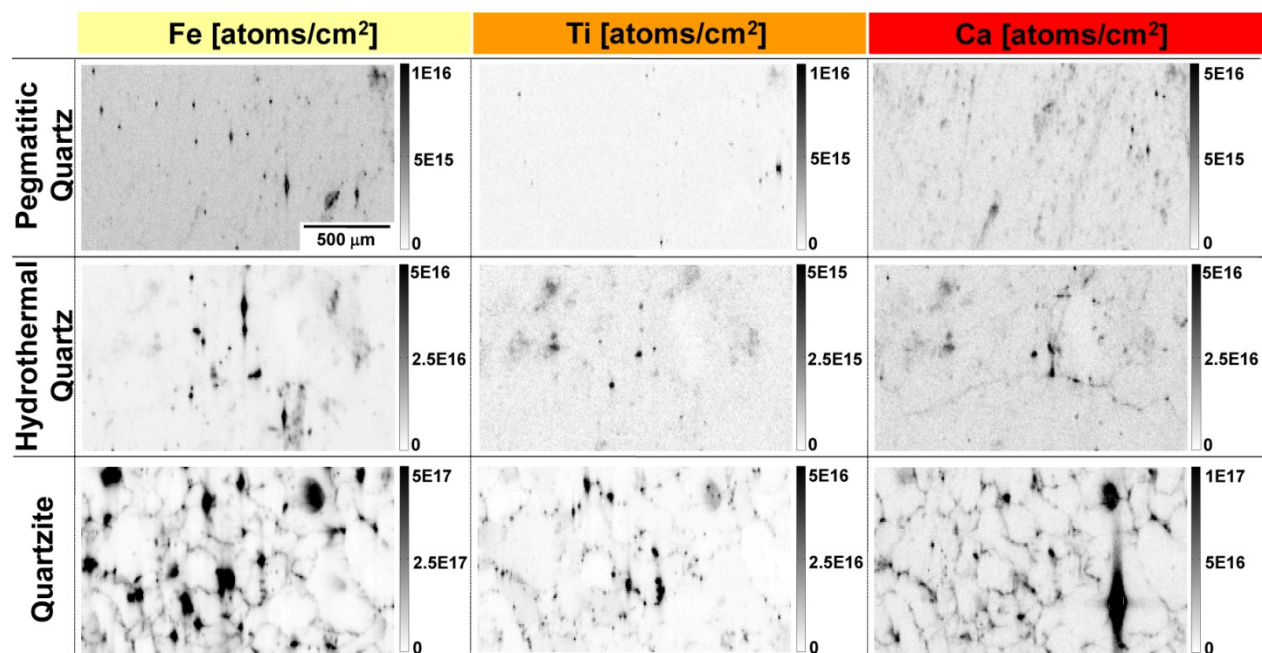


Figure 3.3 μ -XRF maps of silicon-bearing compounds used during silicon refining. Impurities are predominantly seen in clusters, which tend to decorate structural defects. Intensity scale bars are in [atoms/cm²] and are optimized for maximum contrast.

3.4.1. Iron

Fe clusters are detected by μ -XRF in all Si-bearing feedstocks (Figure 3.3, first column) and in some of the C-bearing compounds (Figure 3.4, first column). In pegmatitic quartz, dispersed Fe particles in what is likely an intergranular region are determined by μ -XANES to be ferric (Fe³⁺) species (Figure 3.5a). In the hydrothermal quartz, Fe particles are also distributed throughout the map; comparison with the Ca map suggests that Fe is located predominantly at grain boundaries.

μ -XANES reveals these particles are ferrous (Fe²⁺) species (Figure 3.5b). In quartzite, Fe is present in filament-like nets along grain boundaries (Figure 3.6a) and grain-size inclusions (Figure 3.3). According to μ -XANES analyses, quartzite contains both ferric and ferrous iron-rich clusters (Figure 3.5c). ICP-MS measurements indicate bulk Fe concentrations at or below 20 parts per million weight (ppmw) for pegmatitic and hydrothermal quartz, and above 1000 ppmw

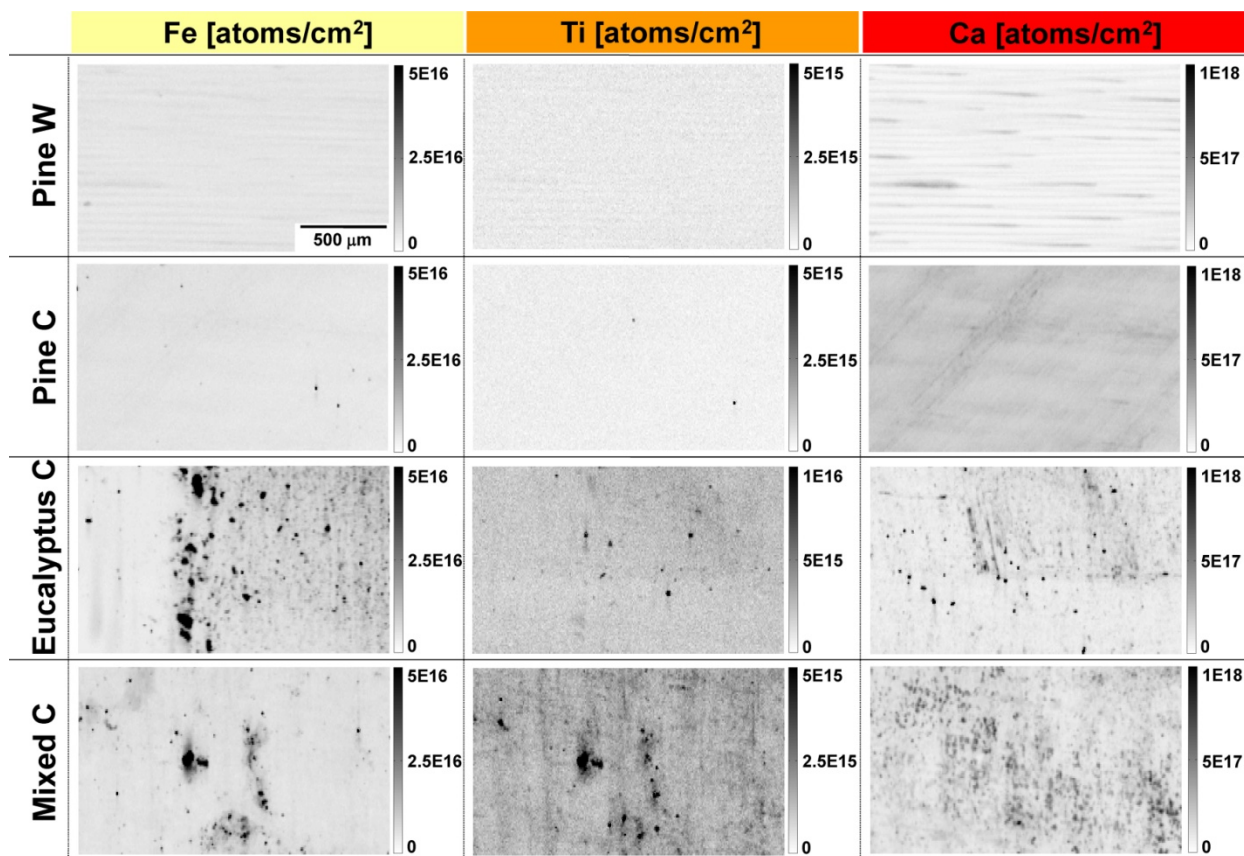


Figure 3.4 μ -XRF maps of carbon-bearing compounds used during silicon refining (“W” stands for woodchip and “C” for charcoal). Impurity clusters can be observed in charcoal samples. Intensity scale bars are in [atoms/cm²] and are optimized for maximum contrast.

for quartzite (Figure 3.7a). Bulk Fe concentrations calculated from μ -XRF maps are comparable to ICP-MS results within a factor of four, suggesting that regions scanned by μ -XRF are representative of each sample as a whole, and that the majority of Fe is contained in second-phase particles.

Fe appears homogeneously distributed along the wood veins in both the pine woodchip and the pine charcoal (Figure 3.4, first column). Fe-rich particles are observed in each of the charcoal samples: in pine charcoal they are either metallic or ferric (Figure 3.5d); in eucalyptus charcoal they are ferric, ferrous, and a mixture of the two (Figure 3.5e); in mixed charcoal they are

predominantly ferric with a few mixed ferric-ferrous particles (Figure 3.5f). ICP-MS measurements (Figure 3.7b) indicate Fe concentrations in the low ppmw for the pine woodchip, pine charcoal, and eucalyptus charcoal, and an order of magnitude higher for the mixed wood charcoal.

3.4.2. Titanium

Ti-rich particles are present in each of the Si-bearing feedstocks (Figure 3.3, second column). In the hydrothermal quartz, some clusters are co-located with Ca along structural defects. In the quartzite, Ti forms circular particles along grain boundaries; Figure 3.4b shows such a nucleus in a high-resolution μ -XRF map. Good agreement between ICP-MS and μ -XRF measurements of bulk Ti is observed (Figure 3.7a), with Ti content increasing from hydrothermal, pegmatitic, to quartzite.

While μ -XRF detects no Ti-rich particles in either of the pine samples (Figure 3.4, second column), a low, homogeneous Ti signal follows the wood veins. ICP-MS confirms low bulk Ti concentrations (Figure 3.7b) in these samples. Ti-rich particles are observed by μ -XRF in the eucalyptus and mixed charcoal samples; ICP-MS correspondingly detects relatively higher bulk Ti concentrations. The oxidation state of Ti determined by μ -XANES is inconclusive in the eucalyptus charcoal; Ti^{4+} is found in the mixed charcoal.

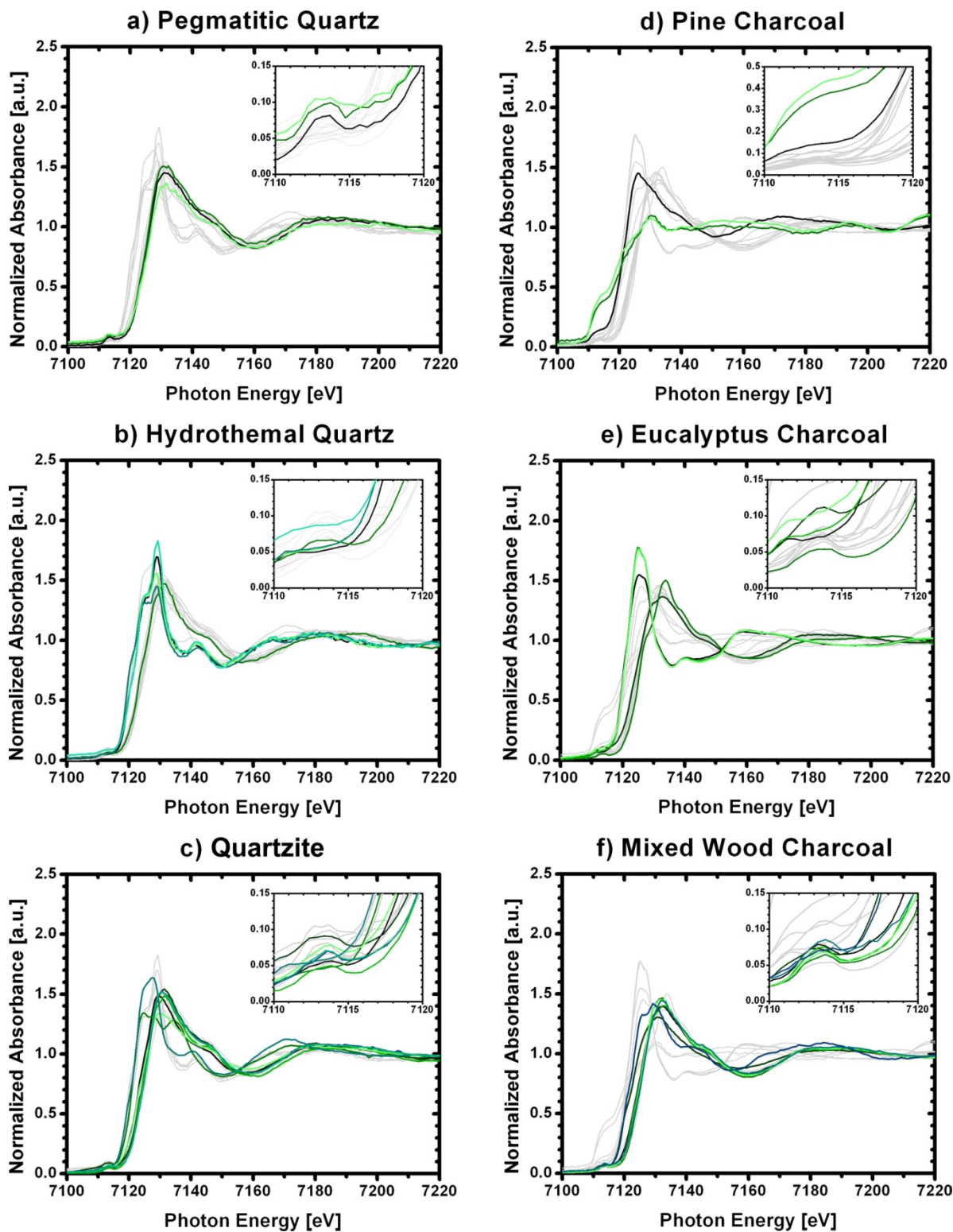


Figure 3.5 Fe K-edge XANES of the Si- (a-c) and C- (d-f) bearing feedstock materials. Fe⁰ peaks at 7110 eV (d), Fe²⁺ at 7111.5 eV (b,c,e), and Fe³⁺ at 7113 eV (a,c,d,e,f); peak splitting between 7111.5 and 7113 eV indicates 2+ and 3+ oxidation state mixing (c,f).



Figure 3.6 μ -XRF map of a grain boundary in quartzite showing distribution of a) Fe, b) Ti, and c) Ca.

3.4.3. Calcium

In the pegmatitic quartz, Ca (Figure 3.3, third column) is closely correlated with the distribution of fluid inclusions. In the hydrothermal quartz, Ca segregates to a textural feature traversing the μ -XRF map, likely a structural defect such as a grain boundary. In quartzite, like Fe, Ca follows grain boundaries in a continuous layer, rather than forming discrete clusters as seen for Ti. For all samples, μ -XANES analyses reveal Ca^{2+} . ICP-MS concentration measurements (Figure 3.7a) reveal an increasing bulk Ca concentration from hydrothermal, to pegmatitic, to quartzite. However, these bulk measurements are systematically lower than those determined by μ -XRF (Figure 3.7a), possibly a result of sampling bias and/or handling.

In both pine samples (Figure 3.4, third column), Ca is distributed along wood veins. In eucalyptus and mixed-wood charcoal, discrete particles containing Ca^{2+} are detected. Bulk Ca concentrations (ICP-MS, Figure 3.7b) range from hundreds to thousands of ppmw for all species, with lowest levels in the pine woodchip.

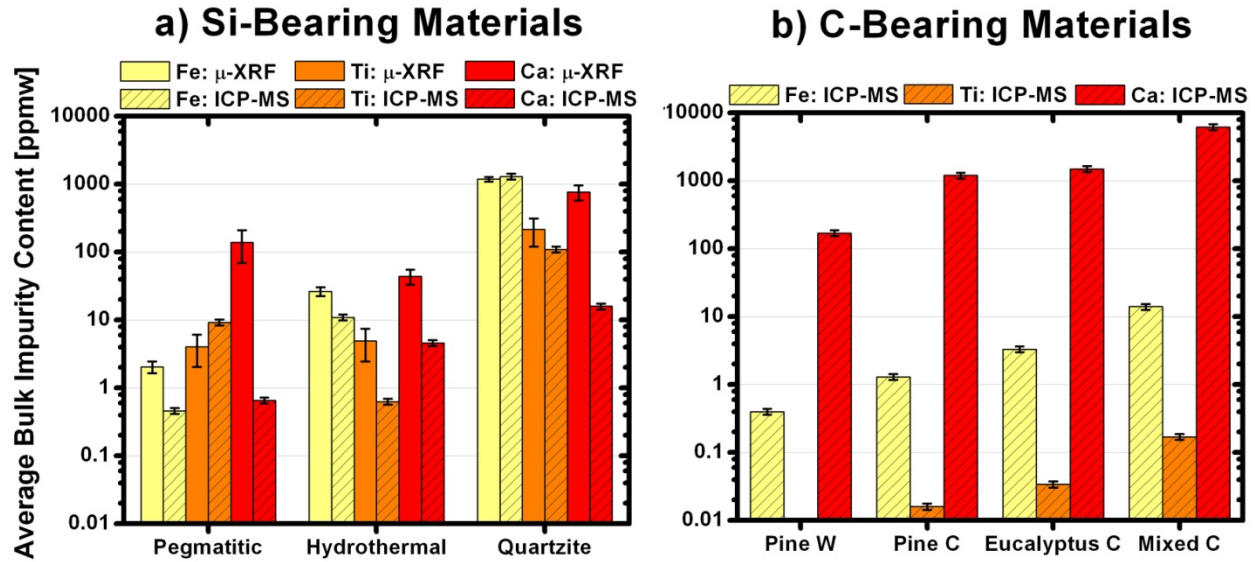


Figure 3.7 Impurity concentration of iron (yellow), titanium (orange), and calcium (red) in the a) Si- and b) C-bearing compounds (“W” stands for woodchip and “C” for charcoal). Results obtained from μ-XRF measurements (full color) are compared to ICP-MS analysis

3.4.4. Elemental Co-Location and Other Impurities

Impurity co-location, inferred via pixel-by-pixel analyses of the μ-XRF maps, can result from interactions (*e.g.*, free energy minimization via precipitation with other elements) or coincidence (*e.g.*, preferred precipitation of two or more elements at the same heterogeneous nucleation site).

In the pegmatitic quartz, co-location of Ti, Ca, and Fe is occasionally observed. It is observed that Ti and Ca interact (*e.g.*, CaTiO_3 , can form in some Fe-rich minerals). Most particles contain Ca, Cr, Fe, Ni, Cu, and Zn. Hydrothermal quartz contains several micron-sized mica based minerals (Fe^{2+}), with traces of Cr, Mn, Cu, and Zn. In Ca-rich particles, Cr, Mn, Fe, Cu, and Zn are also detected.

In quartzite, impurities are often co-located along grain boundaries, albeit with few consistent trends. Ca, Ti, and Fe can be found with traces of K, Cu and/or Zn. Ti-rich clusters often contain Fe, but several other Fe-rich particles do not contain Ti. Ca-rich particles contain Fe but not

necessarily Ti. A higher-resolution μ -XRF image of a grain boundary (Figure 3.6) shows how Fe distributes along the topology of a typical grain boundary; Ti forms a round particle embedded in the Fe; Ca spreads uniformly along the grain boundary and has higher concentration in proximity of the Ti particle.

In the pine woodchip, diffused Fe, Ti, and Ca are co-located along wood veins (Figure 3.4). In the eucalyptus charcoal, a few particles containing Ca and Fe are observed. The mixed wood sample has an abundance of particles with Ca, Ti, and Fe co-located.

3.5. Discussion

While the precise concentrations, oxidation states, and distributions of impurities may vary considerably within quartz deposits and wood sources, we believe the trends reported in this discussion to be generally applicable to a wide range of raw feedstock materials.

The majority of impurities in raw feedstock materials are observed in the form of distinct particles. This is especially true of the Si-bearing feedstock materials, wherein particles are often present at grain boundaries. This conclusion can be inferred from the good quantitative agreement between μ -XRF, which measures impurity concentrations in distinct particles, and ICP-MS, which measures total bulk impurity concentrations (Figure 3.7a). The preponderance of impurities in particles is consistent with reported low solid solubilities of impurity point defects in SiO_2 [38,92,93], and with electronic incompatibilities between impurity atoms and the host matrix [41]. The diffusion of Fe and Ca towards the grain boundaries of quartz has previously been described [38,92]; Ti is also reported to diffuse in quartz, however to a lesser degree [38,59,92,97]. Additionally, some of the detected particles with high melting points are grain-

sized (*e.g.*, in quartzite), indicating that trapping of inclusions during geological formation is another pathway leading to particles of foreign minerals.

In C-bearing compounds, charcoalization causes a higher concentration of second-phase particles (Figure 3.4) and an increase in total impurity content (Figure 3.7b). Although contaminations from handling and from the charcoalization environment are likely responsible, aggregation of pre-existing impurities and/or differences in sample origin (*e.g.*, location in tree) may be contributing factors.

In carbon-bearing feedstocks, the trend of increasing bulk concentration from Ti to Fe to Ca (Figure 3.7b) can be explained by the fact that biological functions prefer divalent ions followed by ions with higher valence [79]. Although impurity concentrations greatly depend on growth environment as well as tissue location within the tree, ICP-MS analyses confirm that concentration of divalent calcium are greater than di- and trivalent Fe followed by tetravalent Ti. A greater understanding of plant biology could lead to naturally purified C-bearing raw feedstock sources.

Reported MG-Si impurity concentrations [98] are often equivalent to or higher than the impurity content measured in the raw feedstock materials herein, suggesting that the current carbothermic reduction process may also contribute a significant amount of impurities. Process contamination is further discussed in Chapter 5.

The observation of distinct particles in raw feedstock materials, often at structural defects, invites conjecture of novel purification processes that exploit this “natural gettinging” phenomenon. Direct introduction into a metallurgical furnace results in the homogenization of feedstock and

impurities, despite the initial phase-separation occurring during natural geological formation or charcoal production.

3.6. Conclusions

Using synchrotron-based microprobe techniques, we analyze microscopic distributions and oxidation states of impurities in silicon and carbon-bearing feedstock materials used in the photovoltaic industry. Within silicon-bearing compounds, comparison between quantitative μ -XRF and ICP-MS suggests the majority of Fe, Ti, and Ca impurities are present in distinct micron- or sub-micron-sized minerals, frequently located at structural defects such as grain boundaries. While the chemical states of impurities vary, they are generally oxidized (*e.g.*, Fe²⁺, Fe³⁺). Impurity concentrations are directly correlated to the geological type of quartz; pegmatitic and hydrothermal quartz have fewer impurities than quartzite. Particles containing Cr, Mn, Fe, Ni, Cu, K, and/or Zn are also detected.

In all carbon-bearing compounds (raw wood and charcoals), Ca is typically diffused uniformly following the veins. In pine wood, Fe and Ti are also diffused uniformly. In contrast, charcoal samples can contain particles of Fe, Ti, and/or Ca. The overall impurity content in the pine charcoal sample is higher than in the pine woodchip, suggesting that the charcoalization process introduces unintentional contamination.

4. During Carbothermic Reduction

Despite the critical dependence of feedstock purification on iron impurity reduction, chemical changes of iron between raw (quartz) feedstock and refined (silicon) feedstock are currently poorly understood. To fill this gap, we investigate the micron-scale distribution and oxidation state of iron in hydrothermal quartz samples during a laboratory-scale simulated reduction process, from room temperature to 1900°C. We used XRD to identify the major mineralogical phases present and we focused on the distribution and oxidation state of Fe using μ -XRF elemental and chemical mapping, and Fe K-edge μ -XANES spectroscopy.

In the untreated quartz, most of the iron is embedded in foreign minerals, predominantly ferric (Fe^{3+}) mica. Upon heating the quartz to 1000°C under industrial-like conditions in a $\text{CO}(\text{g})$ environment, iron is found in ferrous (Fe^{2+}) particles. At this temperature, its chemical state is influenced by mineral decomposition and melting processes, whereas at higher temperatures it is influenced by the molten silicate. As the quartz grains partially transform to cristobalite (1600°C), iron diffuses towards liquid-solid interfaces forming ferric-ferrous clusters. Silica is completely molten at 1900°C and ferric-ferrous clusters result from iron segregation towards interfaces between gas inclusions and molten silica.

4.1. Hydrothermal Quartz

We investigated high-purity hydrothermal quartz currently used for SoG-Si production. To minimize geological differences potentially affecting this study, all analyzed quartz pieces came

from the same initial lump. Furthermore, an untreated piece was used as reference material for the heat treated samples.

4.2. Experimental Procedure

The reducing environment experienced by the quartz in the arc furnace can be experimentally mimicked by reproducing a low oxygen fugacity environment. The heat treatments were performed in a sessile drop furnace with carbon heating elements, constantly flowing CO gas (99.97% purity), and a graphite substrate. Temperature was measured with a Keller PZ40 two color pyrometer operating in the range 900 – 2400°C, with 1% temperature reading uncertainty.

Ten samples, of approximately 3 mm in diameter, were cleaved from a single lump quartz piece, previously cleaned in an ultra-sonic acetone bath. Samples were annealed separately to temperatures ranging between 1000°C and 1900°C in steps of 100°C each. The initial temperature, 1000°C, was reached with a 250°C/min heating rate. Assuming a retention time in a 10 m tall industrial arc furnace of approximately 5.7 hrs [11], a 3°C/min heating rate was used to heat from 1000°C to the final temperature, where each sample was held for 30 minutes, before being quenched to 900°C. The quench occurred faster for the higher temperature samples, *e.g.* 200 and 440°C/min for the samples annealed to 1000°C and 1900°C, respectively. Once the sample reached 900°C, it was removed from the hot zone of the furnace and naturally cooled to room temperature. The entire process occurred in the presence of flowing CO(g). Each sample was monitored during heating using a fire-wire digital video camera (Sony XCD-SX910CR) equipped with a 12× zoom tele-centric lens (Navitar 1-50993D). Each sample was weighted before and after the heat treatment.

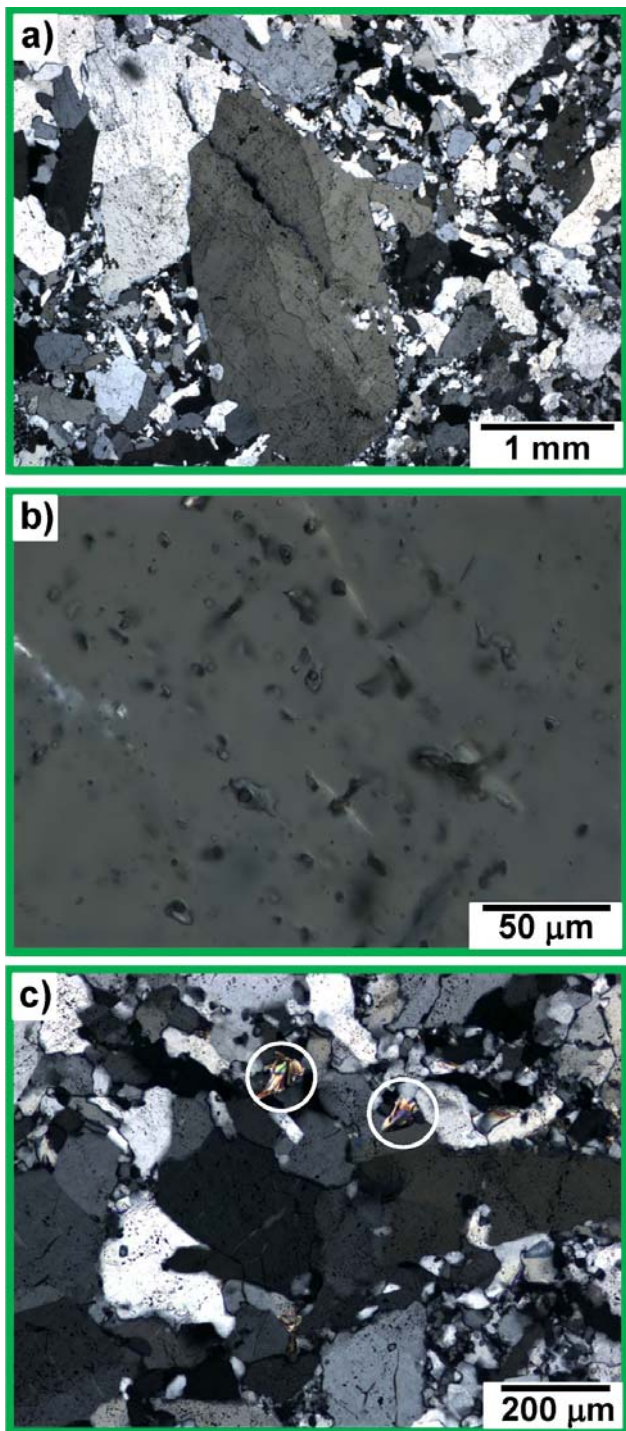


Figure 4.1 Transmitted visible light images of the petrographic thin sections of hydrothermal quartz showing: a) the bimodal grain size distribution; b) H₂O-CO₂ based fluid inclusions; and c) the presence of muscovite crystals (two examples circled in white).

The three samples annealed to 1000°C, 1600°C, and 1900°C were further investigated to determine iron distribution and oxidation state. The 1000°C sample represents the quartz and iron complexes as they are introduced in the furnace; the 1600°C sample represents the iron oxide clusters after melting and the 1900°C sample represents the iron behavior after the host material also reaches molten state (1723°C).

4.3. Results

Results are divided between the SiO₂ host matrix and the Fe embedded within: first, both the crystallographic and mass evolutions of SiO₂ upon heating are presented; second, results on Fe clusters are shown focusing on distribution and oxidation states.

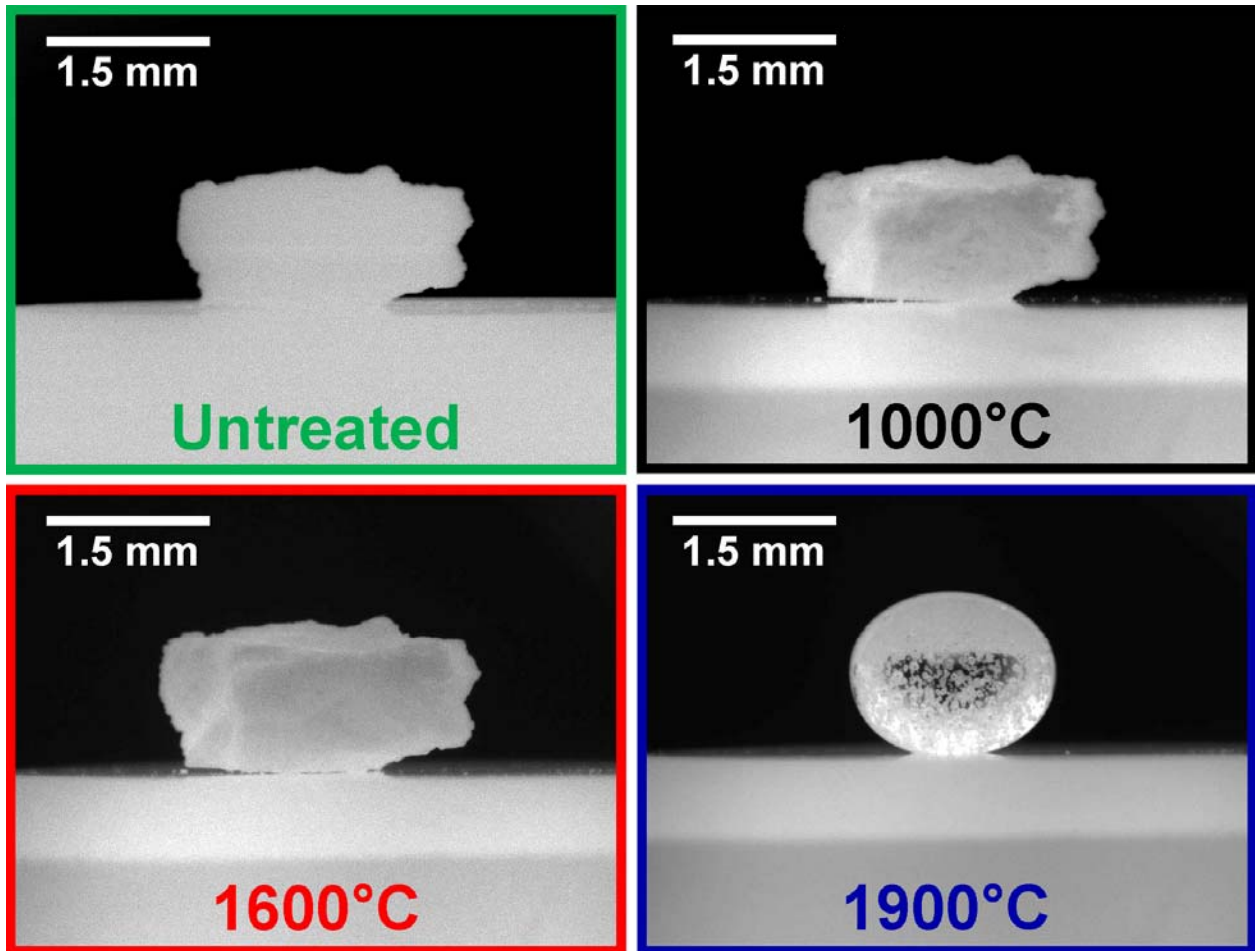


Figure 4.2 Snapshots of the quartz being heated to 1900°C. The silica first expands (1000-1600°C) then contracts into a droplet, typical of the molten state (1900°C).

4.3.1. Host Matrix - Silica

Viewed in transmitted light (Figure 4.1a), the untreated quartz shows a variety of grain sizes. Subgrain formation, where a few large grains are surrounded by smaller ones, suggests fast recrystallization due to high circulation of hydrothermal fluids. Grains have sharp corners and irregular edges; some overgrowth of smaller grains in larger ones is visible. A geological alteration is also confirmed by the abundance of intergranular H₂O-CO₂ fluid inclusions (Figure 4.1b). Mica (muscovite KAl₃Si₃O₁₀(OH,F)₂), grains are visible (Figure 4.1c).

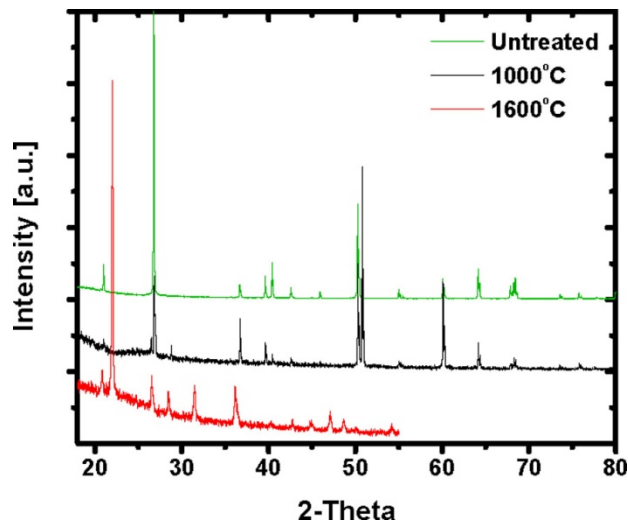


Figure 4.3 Crystalline structure versus annealing temperature: silica is found as quartz in the untreated sample and at 1000°C; it transforms to a mixture of quartz, cristobalite, and molten state at 1600°C. The 1000°C and 1600°C spectra are multiplied by ten and upward shifted.

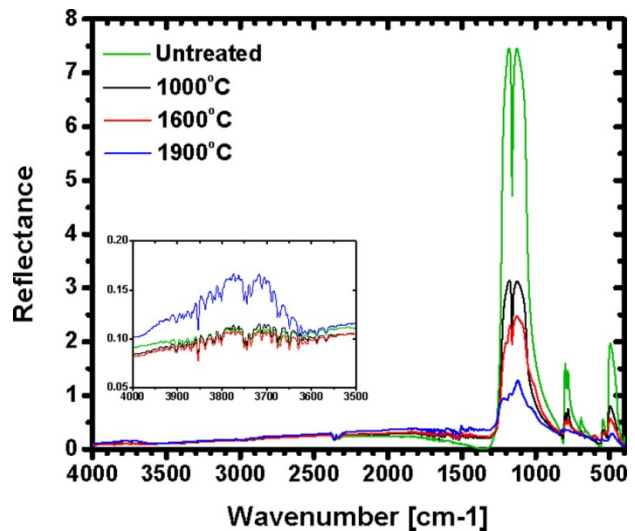


Figure 4.4 Room temperature reflected FT-IR spectra; the untreated quartz FT-IR spectrum is used to infer changes upon annealing in the other three spectra.

As an example of the heating process, Figure 4.2 depicts the sample annealing process at four different temperatures during the anneal: room temperature (green), 1000°C (black), 1600°C (red), and 1900°C (blue). As the temperature increases, a volumetric expansion (1000-1600°C) is followed by a contraction while transforming into a molten drop (1900°C). Opacity is also affected by temperature: prior to complete melting, quartz is opaque-white; the molten state (1900°C) is transparent, with a multitude of gas bubbles.

Analysis of the untreated quartz thick section by XRD detects the presence of α -quartz phase only (Figure 4.3). A reflected FT-IR spectrum of this sample is shown in Figure 4.4. Observation in reflected light reveals the same wide grain size distribution (Figure 4.5a) previously described (Figure 4.1a). Here, black spots are surface voids probably created by the petrographic section preparation process. The sample annealed to 1000°C (Figure 4.5d) shows a similar grain size

distribution and only α -quartz phase (Figure 4.3). Melting is visible in the sample annealed to 1600°C (Figure 4.5g), where channels with linear fabric are the result of quenched molten silica. XRD, consistently with optical observations, detects co-presence of quartz and cristobalite (Figure 4.3); FT-IR depicts presence of cristobalite (Figure 4.4) as per comparison of tridymite spectra collected by [99]. As the quartz grains melt, β -cristobalite crystallizes around the molten channels (Figure 4.5g). The entire sample melts upon further heating to 1900°C (Figure 4.5l). Gas bubbles, due to microscopic cavities, such as pre-existing fluid inclusions visible in Figure 4.1, and to gases introduced during the annealing process, are evenly scattered throughout the sample. The crack cutting horizontally through Figure 4.5l is possibly due to quenching. Upon heating SiO₂ loses mass; as depicted in Figure 4.6a, a loss of 35% is reached with the sample annealed to 1900°C.

4.3.2. Iron

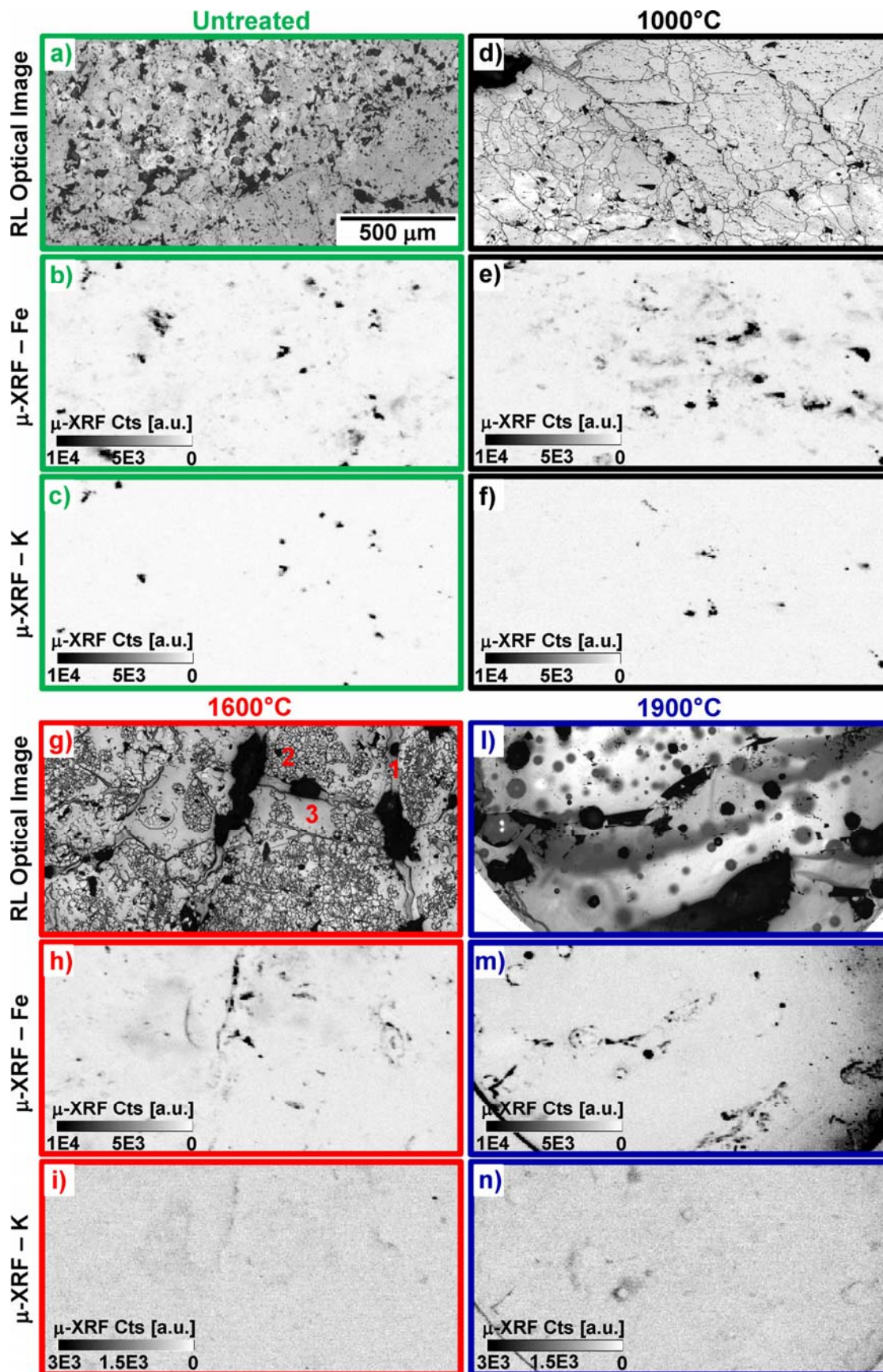
μ -XRF Fe distribution maps are shown in Figure 4.5b, e, h, m along with their optical images counterparts (Figure 4.5a, d, g, l, respectively). Distinct Fe clusters constellate both the untreated quartz (Figure 4.5b) and the sample annealed to 1000°C (Figure 4.5e). Instead, in the sample annealed to 1600°C, Fe segregates towards molten channels, quenched into glass (Figure 4.5h). Similarly, in the sample annealed to 1900°C, Fe decorates the interfaces between the gas bubbles and the surrounding SiO₂ glass (Figure 4.5m). Fe segregation towards interfaces is underlined in the bicolor coded (Fe in blue, Si in red) maps displayed in Figure 4.7. In the sample annealed to 1600°C (Figure 4.7a), Fe lies between the quartz – β -cristobalite and the molten channel (Figure 4.7b); whereas, in the sample annealed to 1900°C (Figure 4.7c), Fe coats gaseous features (Figure 4.7d) as well as the outer layer of the sample in contact with the gas (visible in the lower

left corner of Figure 4.7c). The Fe oxidation state during the heating process is investigated by μ -XANES (Figure 4.8). Initially present in a 3+ valence state, it reduces to 2+ upon heating to 1000°C, exhibiting a pre K-edge peak at 7111.5 eV. Fe is found re-oxidized at higher temperatures: Fe³⁺ is detected in both the 1600°C and 1900°C samples, where the pre K-edge peak is at 7113 eV. However, linear combination fitting of the μ -XANES spectra of these last two samples suggests co-presence of Fe³⁺ and Fe²⁺ (Figure 4.9). As explained in Chapter 2, linear combination fitting has $\pm 10\%$ error and the Fe⁰ resulting from the fitting procedure is within this analytical error.

Co-presence of oxidation states could also be inferred in the Fe chemical maps of the samples (Figure 4.10). However, small sample drifting issues could not be registered perfectly and generated particle edge effects. For this reason, caution should be used when using them to claim oxidation state co-presence.

Compositional point analysis performed on the μ -XRF maps (Figure 4.11) shows that Fe is initially co-located with K, Cr, Cu, and Zn in the untreated quartz, whereas in the sample heated to 1000°C no Zn is found associated with Fe. The samples heated to 1600°C and 1900°C show K, Ca, Ti, Cu and Zn associated with Fe.

Figure 4.5 Transmitted visible light micrographs (a,d,g,l) and corresponding μ -XRF Fe (b,e,h,m) and K (c,f,i,n) distribution maps of untreated, annealed to 1000°C, 1600°C and 1900°C samples, collected at 10keV. The field of view for each sample is 2000 x 1000 μm^2 . The untreated sample (a) has a structure similar to the one of the sample annealed to 1000°C (d). The same is valid for the Fe-rich particles (b and e), which are seen as distinct particles, possibly co-located with muscovite ($\text{KAl}_3\text{Si}_3\text{O}_{10}(\text{OH},\text{F})_2$) crystals seen in transmitted light (Figure 1b); K-rich particles (c and f) are in fact co-located with Fe. In the sample annealed to 1600°C (g), molten silica channels (1) and cristobalite formation (2) are visible around quartz (3); at this temperature, Fe preferentially segregates towards molten features (h). At 1900°C the sample is completely molten and gas bubbles are evenly distributed (l). Fe is found only at interfaces between the gaseous phase and the glassy silica (m). In these latter samples, K mostly volatilized (i, n).



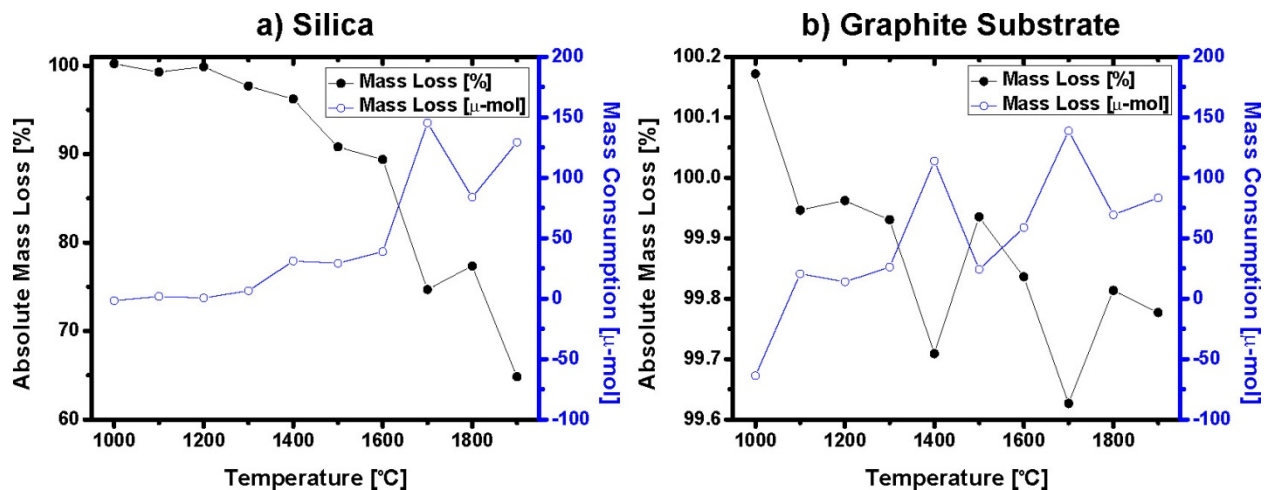


Figure 4.6 Absolute (left axis) and relative (right axis) mass loss of both silica (a) and graphite substrate (b). In the case of silica, mass loss is caused by SiO(g) formation; the graphite substrate mass change is potentially caused by reaction with the reducing gas and with the silica. Lines are only an eye guide. Mass measurement errors fall within the size of the point markers.

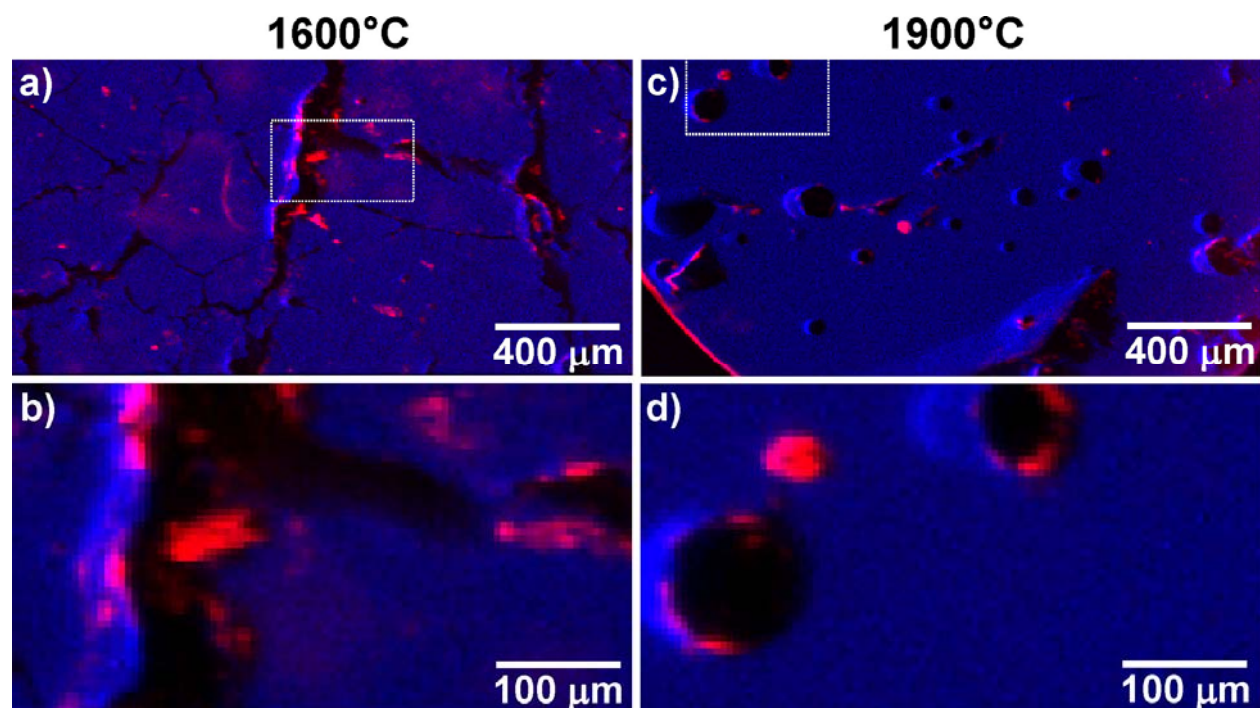


Figure 4.7 Iron (coded in red) segregates preferentially towards interfaces: 10keV μ -XRF maps show Fe located in Si- (coded in blue) deprived molten channels visible in the sample annealed at 1600°C (a) and in gaseous bubbles as well as along the sample interface in the sample annealed at 1900°C (c). Selected sub-regions in a) and c) are shown in the 7.3 keV μ -XRF maps b) and d), respectively. Color intensity reflects XRF counts and is optimized for maximum contrast.

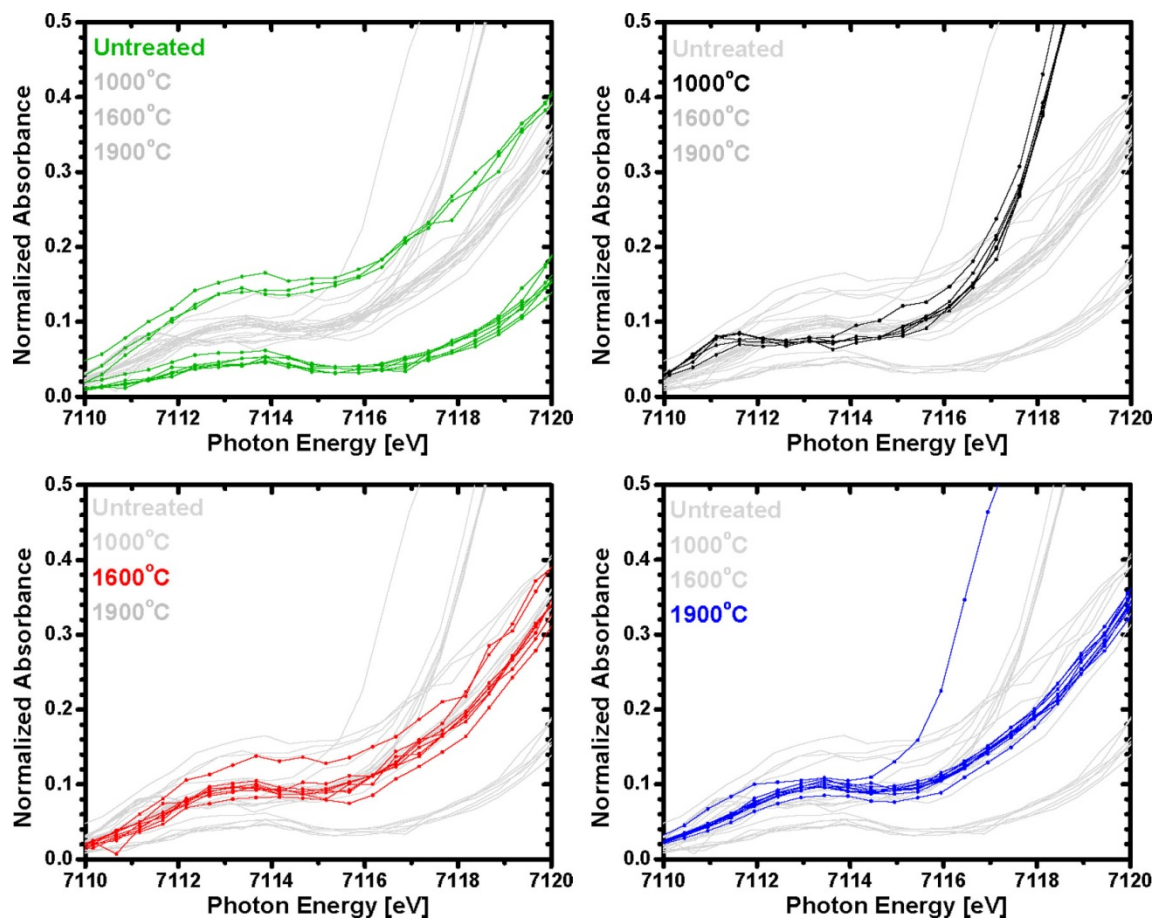


Figure 4.8 Fe pre K-edge μ -XANES peaks: Fe^{3+} peaks at 7113 eV (RT, 1600, 1900°C); Fe^{2+} at 7111.5 eV (1000°C). However, least-square linear combination fitting of the full spectra shows that at high temperatures (1600 and 1900°C) these peaks are the result of a combination of Fe^{3+} and Fe^{2+} (see Figure 4.9).

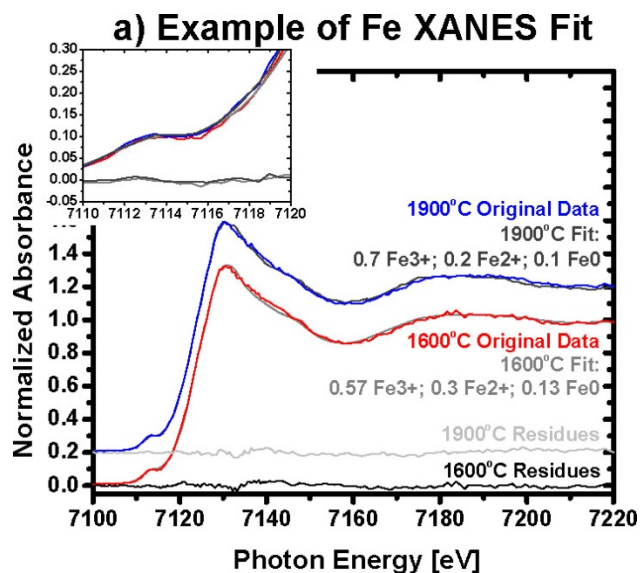


Figure 4.9 Example of a least-square linear combination fit of the μ -XANES of one particle at 1600°C (red) and 1900°C (blue, shifted upwards): co-presence of Fe^{3+} and Fe^{2+} oxidation states is found.

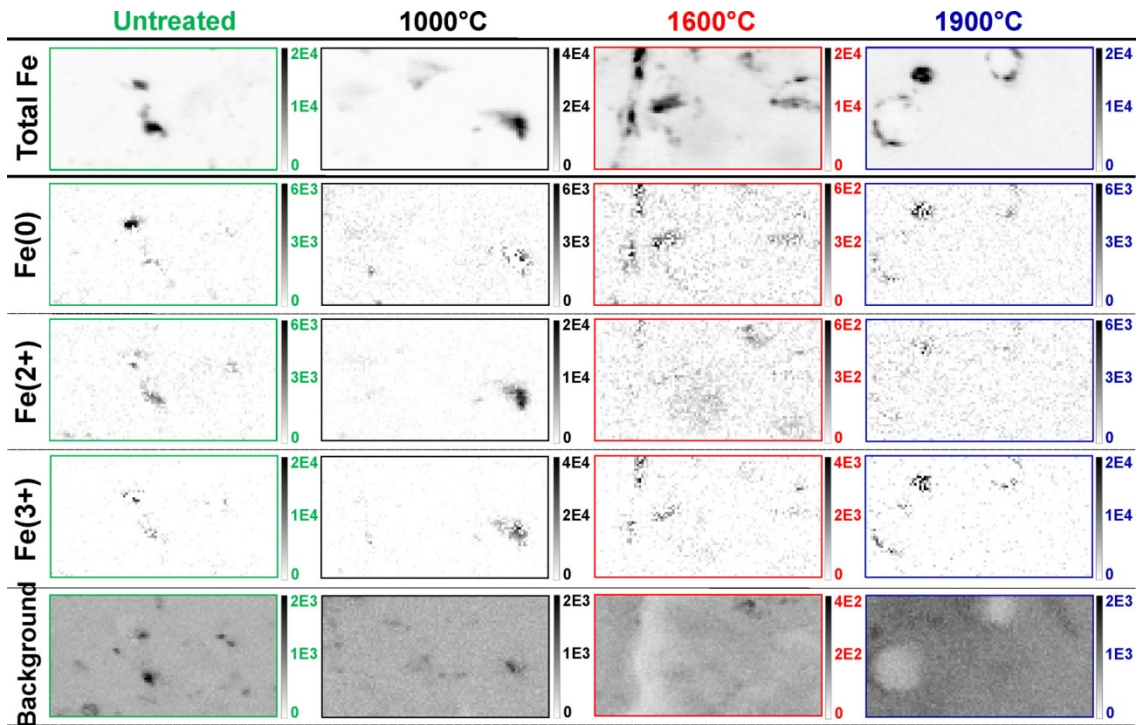


Figure 4.11 μ -XRF chemical maps of the Fe oxidation state evolution. The “Total Fe” (first row) depicts total Fe measured above the K-edge (7.3 keV). This μ -XRF map is then fitted by a XANES database comprising Fe(0), Fe(2+), and Fe(3+) species and split between “Fe(0)” (second row), “Fe(2+)” (third row), and “Fe(3+)” (fourth row). See text for description. All maps measure 500 x 250 μm^2 ; intensity scale bars are in μ -XRF counts and are optimized for optical contrast.

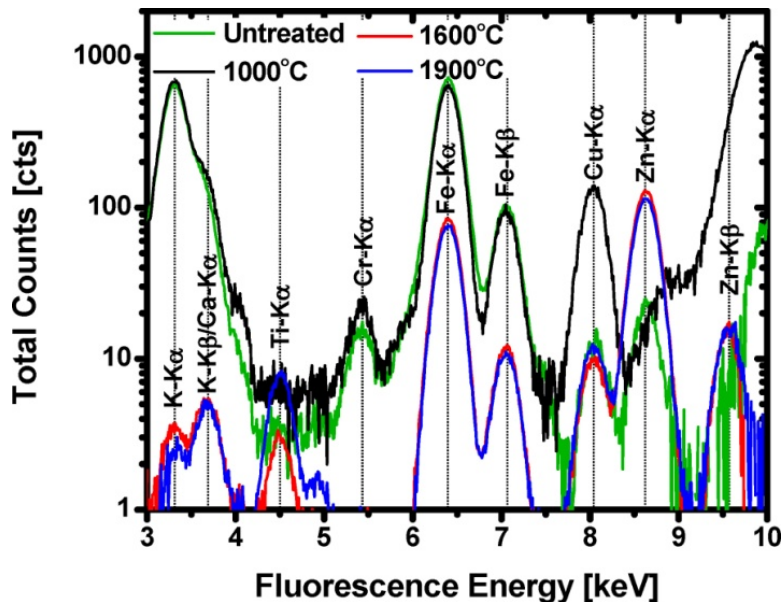


Figure 4.10 Temperature dependent elemental composition of one characteristic Fe-rich particle per sample. Main differences are the presence of: Cr (untreated, 1000°C), Ca and Ti (1600°C, 1900°C).

4.4. Discussion

The effects of the reducing environment are evaluated as a function of the descent of the quartz in the arc furnace. Once the perspective of the environment influencing the quartz is detailed, the discussion shifts first towards the host matrix – silica, as it heats and melts; then towards the iron, the evolution of its distribution and chemical states. In the subsequent sub-sections, general thermodynamic models are offered to describe the experimental observations presented in Section 4.3. Some of this discussion remains tentative, and subject to further experimental confirmation.

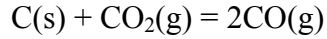
4.4.1. Effect of the Reducing Environment

As the raw feedstock descends in an industrial furnace, it is exposed to ascending reducing gases. Si(l), produced in the crater zone near the electrodes, results primarily from the reaction between SiO(g) and SiC(s).

The reducing ambient present in the laboratory furnace is formed by the CO(g) and by the graphite substrate, C(s); both have an active role in the reduction process by influencing the quartz, and eventually Fe. Contrary to the industrial case, the reducing environment is kept constant throughout the heating process and gaseous by-products are removed from the hot zone without contributing further to the reduction process.

In the presence of CO(g) and C(s), the overall system is mainly described by two reactions occurring simultaneously [100]:





2)

SiO(g) is an intermediate species, whose high partial pressure is needed for Si production [32]. By reacting with C(s), SiO(g) forms SiC(s), which in turn will form Si(l) upon reaction with SiO(g). Reaction 1) implies equi-molar formation of SiO(g) and CO₂(g). According to thermodynamic calculations, SiO₂(s) reduction via CO(g) requires an atmosphere with a gas ratio $p_{\text{CO}_2}/p_{\text{CO}}$ of 10^{-4} - 10^{-5} [9,100]; this ratio implies that minimal CO₂(g) formation quenches the reduction. However, if the CO(g) stream through the furnace removes the CO₂(g), then reaction 1) proceeds and the weight loss measured above 1400°C (Figure 4.6) is caused by SiO(g) formation, solely limited by surface reactions, rather than CO(g) flow condition or quartz particle size [101]. However, CO₂(g) removal implies removal of SiO(g), preventing sufficient SiO(g) partial pressure buildup, necessary to reduce fully the sample.

Reaction 1) is the main reaction leading to formation of SiO(g) on the outer surface of the sample. At the quartz-graphite interface, direct reaction of the SiO₂(s) with C(s) also leads to SiO(g) formation; subsequently, SiO(g) reaction with C(s) could form SiC(s). Yet no SiC(s) is observed (Figure 4.12) and the Si(l) droplets visible at 1400°C result from SiO₂(s) + C(s) = Si(l) + CO₂(g). A thin oxide layer prevents them from wetting the graphite substrate, infiltrating it, and forming SiC(s). Si(l) is metastable in the presence of unconsumed solid carbon and, at higher temperatures, it evaporates or reacts with SiO₂(s) releasing SiO(g). Further reaction between this latter and C(s) is excluded as no SiC(s) was found on the substrate.

Graphite morphological modifications visible in Figure 4.12 are primarily due to reaction 2); at the SiO₂(s) – C(s) interface, CO(g) can be formed or decomposed based on local equilibrium fluctuations. The measured graphite mass loss is caused by reaction with CO₂(g) to produce

CO(g), or by CO(g) decomposition followed by diffusion of C(s) in the SiO₂(s,l) and by CO₂(g) removal.

4.4.2. Silica Evolution

The initial quartz is formed by a multitude of grains with α -quartz crystalline structure. According to the phase diagram of the SiO₂ crystalline polymorphs [49], as soon as the quartz is shock heated to 1000°C, it transforms to β -quartz through a fast displacive phase transition (573°C) and it enters the hexagonally-packed (HP)-tridymite stability field (870°C). Instead of HP-tridymite, only α -quartz is detected (only the α - phase can be measured at room temperature, as the β - phase is unstable and transforms to α - phase upon quenching [102]). Instead, the lack of HP-tridymite might be caused by either a too fast heating rate (250°C/min) to allow the slow reconstructive phase transition to occur, or the lack of mineralizing agents needed to seed HP-tridymite crystallization [103].

As a multi-component system (quartz – trace element), impurity concentration affects the melting temperature, which in principle can be as low as the eutectic temperature of the multi-component system. Onset of heterogeneous melting occurs locally along grain boundaries [55,56], where impurities preferentially segregate [41] and cluster in foreign minerals, as observed in Figures 4.5b, e. In addition to the crystallographic phase change, at 1000°C melting is expected at grain boundaries decorated with impurities, in grains with high concentrations of impurities and at boundaries separating adjacent grains of different minerals (*e.g.* quartz – mica). Local melting cannot be excluded, even though glassy features and droplets are not observed by optical microscopy (Figure 4.5d).

Mimicking the descent in the industrial furnace, quartz is heated from 1000°C to 1600°C (3°C/min), where it reaches the β -cristobalite stability field (1470-1723°C) [49]. This reconstructive phase transition causes the volumetric expansion visible in Figure 4.2. Quartz can melt incongruently at a metastable melting temperature of 1425°C [53] and slowly transforms, via a liquid intermediate phase, to β -cristobalite from the external molten grain surface inwards (Figure 4.5g). As molten features appear, diffusion of impurities and gaseous species becomes favorable through molten silica paths, potentially affecting β -cristobalite formation by enhancing (oxygen [54]) or hindering (carbon [55]) propagation of the β -cristobalite-liquid silica interface. Due to conflicting mechanisms, such as the large superheating quartz can sustain [55,56] versus the small samples used; or impurity diffusion [54,55,104] and heat diffusion versus interface kinetics [53], transition to β -cristobalite is incomplete. This is verified by the simultaneous presence of quartz, β -cristobalite, and melt detected by XRD and optical microscopy (Figure 4.5g).

Near the furnace electrodes, where temperatures exceed the nominal melting temperature of β -cristobalite (1723°C), silica is in the liquid stability field [49]. The sample annealed to 1900°C is completely molten and forms a droplet on the graphite substrate (Figure 4.2). As the heating process is performed outside equilibrium conditions, the obtained molten state can result either from β -cristobalite formation which then melts, or from molten silica channel growth prior to complete transformation to β -cristobalite. The final sample retains a transparent, oxidized appearance (Figure 4.2 and Figure 4.5l) with gas bubbles evenly distributed, indicating that the pre-existing CO₂ based fluid inclusions diffused through the sample and that gaseous products of the reaction at the silica-graphite interface have in-diffused. Due to a small temperature gradient

between the substrate and the top of the sample (a few °C), gases and C that in-diffuse at the SiO₂-graphite interface, ascend in circular patterns created by Marangoni's effect. Gases and C react with the surrounding silica and remain trapped in the viscous droplet forming the bubbles visible in Figure 4.5l. A gas bubble crosscut would show a gas void surrounded by an amorphous boundary layer, rich in impurity clusters, such as Fe-bearing particles (Figure 4.5m and 4.7d), and SiOH molecules, separating the gas phase from the SiO₂ glass.

4.4.3. Evolution of Distribution and Oxidation State of Iron

In the untreated quartz, Fe is predominantly embedded in muscovite grains (Figure 4.1c), as also confirmed by K co-location (Figure 4.5b). Fe-rich muscovite, K₂(Fe,Mg)₄(Al,Si)₈O₂₀(OH,F)₄, is a dioctahedral mica. Fe, with Mg, replaces Al in octahedral sites in either a 2+ or 3+ valence state [105,106], with 3+ favored in this substitution. The pre- K-edge feature of Fe-rich micas is orientation dependent, affecting both the peak intensity and energy [107,108]. However, a clear predominance of Fe³⁺ is confirmed by the single Fe pre- K-edge peak at 7113 eV (Figure 4.8).

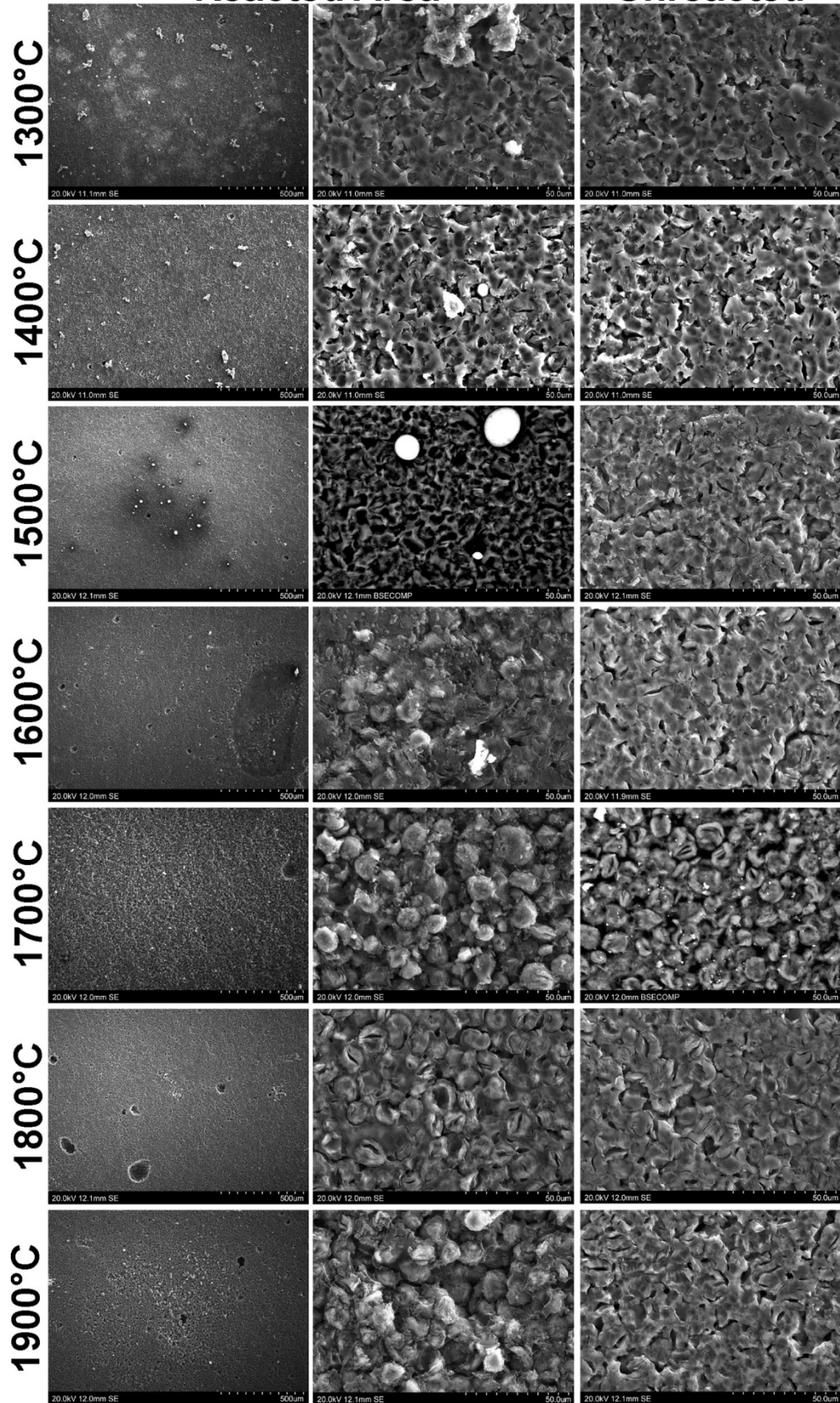
Similarly, at 1000°C, Fe is still embedded in distinct grains (Figure 4.5d and e). Yet, muscovite, an OH⁻ bearing mica, which decomposes before melting, has a decomposition onset lower than 600°C. Decomposition can lead to formation of corundum (Al₂O₃), K-feldspar (KAlSi₃O₈), and water [109]. With only 30 min at 1000°C, the sample starts undergoing delamination (exfoliation) and decomposition (structural breakdown) leading to formation of Fe oxides [110].

Within a quartz solid matrix, species formed from the parent muscovite are diffusion-limited and

Figure 4.12 SEM images of the graphite substrates after being heated in CO(g) with SiO₂. The first column shows the area in contact with the SiO₂; the second column, details of the reaction between the silica and the graphite; the third column, an area far from the reaction zone. See text for reaction description.

Reacted Area

Unreacted



K is still visible in clusters (Figure 4.5f). Upon quenching to 900°C and slowly cooling to room temperature, the Fe²⁺ present (Figure 4.8) might be caused by local rearrangement of the decomposed muscovite, independently of the reducing environment used during the heat treatment. Moreover, Gibbs free energy minimization predicts the stability of Fe²⁺.

As the muscovite melts, chemical zonation occurs while an MgO- and F-rich boundary melt forms in contact with it [111]. Until muscovite is present, this boundary melt is immiscible with the boundary melt formed by the SiO₂ [64,112]. At 1600°C and 1900°C, muscovite is completely dissolved and its boundary melt disappears, intermixing with the SiO₂ melt (Figure 4.5i, n). Similarly, Fe homogenizes in the SiO₂ melt (Figure 4.5h and 4.7). After the quench, Fe²⁺ is present (Figure 4.9), even though the oxidized form is still predominant at both 1600°C and 1900°C: re-oxidation of Fe from 2+ to 2+/3+ could be correlated with the formation of a liquid-glassy silica phase.

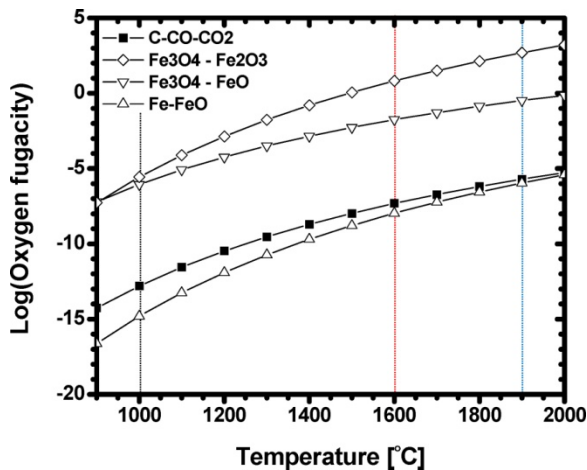


Figure 4.13 Stability of the Fe oxidation state based on the oxygen fugacity. At 1600°C and 1900°C, the stability field of Fe⁰ is thermodynamically approached. Fe data from Ohmoto 1977; C-CO-CO₂ data from Jakobsson 1994 .

If the system were in equilibrium with the carbon substrate, oxygen fugacity of the system could be used to infer the presence of oxidation states (Figure 4.13). Using Fe stability fields provided by [113] and the C-CO-CO₂ stability field provided by [114], a mixture of Fe²⁺ and Fe³⁺ is expected in the magnetite (Fe³⁺₂Fe²⁺O₄) – wüstite (Fe²⁺) stability field. However, at higher temperatures, as the CO + O₂ = CO₂ equilibrium approaches (without entering) the iron (Fe⁰) –

wüstite (FeO) stability field, Fe^{2+} is thermodynamically stable. Even though reduction of iron is thermodynamically predicted at these high temperatures in the presence of a $\text{CO}(\text{g})$ atmosphere, conditions far from equilibrium and failure to reduce silica to silicon lead to only partial reduction of Fe. As predicted by oxygen fugacity calculations, the amount of initial Fe^{3+} should decrease in favor of Fe^{2+} ; this is indeed seen experimentally with respect to the initial quartz.

4.5. Conclusions

Metallic impurities are detrimental to Si solar cell performance, yet they are already present in the raw feedstock material currently exploited for SoG-Si production via carbothermic reduction. With the goal of broadening the knowledge of metallic impurities at an earlier stage of the refining process, we mimicked the reduction process and evaluated it from a twofold perspective: the host material, quartz, and a metallic impurity, iron.

The initial raw feedstock material, quartz, transforms to a mixture of quartz, β -cristobalite, and melt (1600°C), before reaching a completely molten state (1900°C). $\text{Si}(\text{l})$ formation is found at relatively low temperatures (1400°C) but it disappears due to its instability in the presence of $\text{C}(\text{s})$. Insufficient intermediate species, $\text{SiC}(\text{s})$ and $\text{SiO}(\text{g})$, prevent formation of $\text{Si}(\text{l})$ at higher temperatures leaving the majority of the sample oxidized. The measured mass loss is caused by $\text{SiO}(\text{g})$ formation and removal.

Iron is predominantly clustered in foreign minerals present in the quartz and its oxidation state is influenced by its hosting mineral. In this specific case, Fe is present in distinct muscovite crystals with predominance of Fe^{3+} . At 1000°C , Fe is affected by the boundary melt formed by decomposition of muscovite and is found as Fe^{2+} . At higher temperatures, muscovite disappears

and Fe, predominantly oxidized, diffuses in the molten silica (1600-1900°C) segregating towards interfaces. Contrary to thermodynamic expectation, Fe is oxidized until late in the reduction process as the silica melt protects it from gases present in the furnace, hence minimizing its reduction, only partially measured at high temperatures.

5. After Carbothermic Reduction: Metallurgical Grade Silicon

Investigations regarding trace elements in quartz [25,115,116] and studies regarding detrimental impurities in silicon [21,70] can be found in the literature. As extracted today, MG-Si (> 98%) contains impurities from both the raw feedstocks and the environment extraction process.

Industrial information regarding the raw feedstock and the derived MG-Si is generally withheld and reports regarding how impurities are affected by the refining process are unavailable to the scientific community. To fill this gap, bulk chemical analyses (ICP-MS and/or GD-MS) of the quartz and of the MG-Si industrially extracted from it are presented and compared. While considering other major sources of impurities, we highlight the importance of clean raw feedstock materials.

5.1. Materials and Method

Two samples were provided by a MG-Si producer: the initial quartz and the extracted MG-Si. Unfortunately, no other information regarding these samples was provided and the following description is solely based on microscopy and bulk chemical investigations.

Transmitted cross polarized light microscopy was used to evaluate the quartz sample. Polished MG-Si surfaces were investigated by SEM and EPMA to evaluate elemental co-location. ICP-MS analyses were performed on both materials; GD-MS analyses were performed only on the

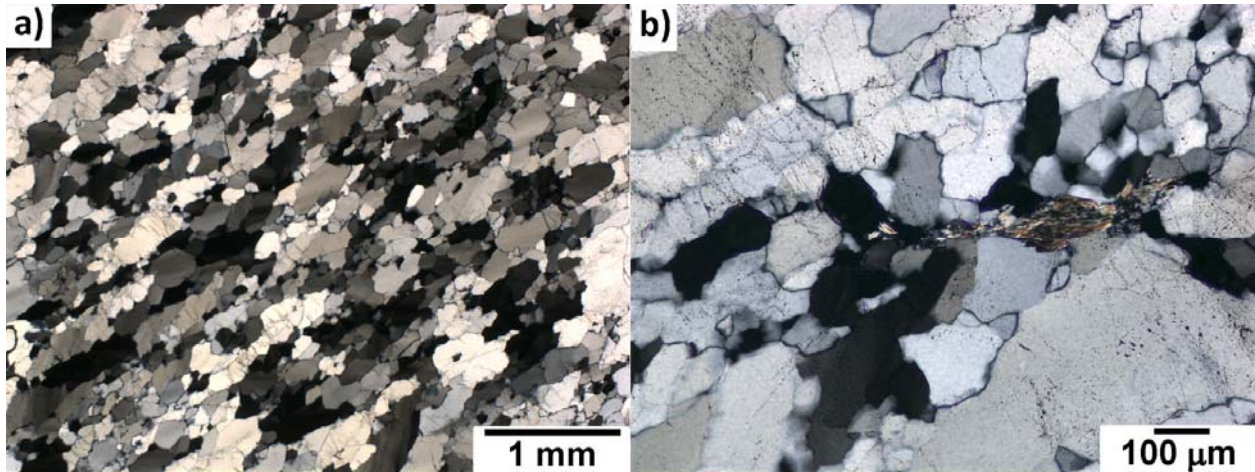


Figure 5.1 Two transmitted light images of petrographic thin sections of the quartzite used to extract the metallurgical-grade silicon discussed in this chapter. During metamorphism, quartz grains re-aligned following a shearing direction. Trails of fluid inclusions (black dots) perpendicular to the shearing direction and a foreign mineral are visible in b).

MG-Si samples. These values are also reported as comparison and validation of the two analytical techniques.

5.2. Observations

Results are presented first for quartz, then for MG-Si. Microscopy-based observations of the material are followed by impurity concentration results. Comparison of the two materials and hypotheses regarding impurity clustering as well as contamination sources are presented in the discussion.

5.2.1. Quartzite

The initial quartz is milky-white in colour. Viewed in transmitted cross polarized light, quartz grains are preferentially aligned in a common shearing direction, in response to a local stress field (Figure 5.1a). During and after shearing, the quartzite underwent partial recrystallization:

grain edges depict subgrain recrystallization (small quartz grains formed along the edges of larger quartz grains), which should relieve the shear tensions accumulated in the quartz lattice structure. Recrystallization is also inferred by the presence of 120° triple junctions between grains. Grains have inequigranular (uneven) to seriate (gradual and continuous variation in grain size) texture with anhedral edges and lobate grain boundaries. Trails of fluid inclusions perpendicular to the shearing are visible as well as foreign mineral grains (Figure 5.1b).

ICP-MS analyses (Figure 5.2) reveal this is a high-purity raw feedstock material with only high concentrations of Ca and Al (Al not shown). All other elements have ppmw or sub-ppmw concentrations.

5.2.2. Metallurgical-Grade Silicon

The MG-Si chunk provided has an uneven surface that shows dendritic crystal growth, yet it has no crucible lining particles. This suggests a surface layer that underwent a fast top-down solidification process, in agreement with casting solidification performed by MG-Si producers [9].

SEM images (Figures 5.3 a, d, and g) depict areas with multi-crystalline silicon. Grain boundaries are decorated with impurities; Figures 5.3 c, f, and i focus on selected areas chosen in the large area images: Al, Ca, and Fe are predominant with minor traces of Ti. The second-phase precipitates show internal elemental segregation, as clearly visible in Figure 5.3e, where a phase rich in Al and Ca with presence of some Si is adjacent to an Fe-, Si- rich one. Moreover, Ti is found only co-located with Fe and Si.

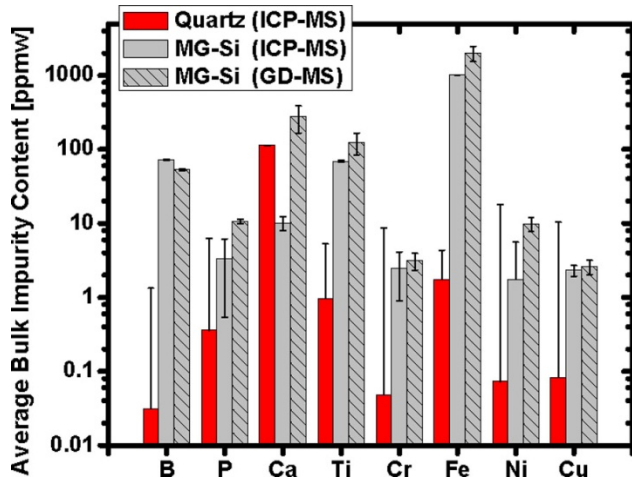


Figure 5.2 Impurity bulk concentration analyses. Impurities in quartzite (red) are compared to the ones obtained in the MG-Si (gray). For this latter, ICP-MS (gray) analyses are compared to GD-MS (textured gray).

Chemical bulk analyses of this MG-Si reveal impurities are all well above the ppmw level (Figure 5.2). GD-MS values confirm ICP-MS results; only the Ca concentration is significantly different between the two bulk techniques. ICP-MS analyzes 0.35 mg of material, while the GD-MS sputtering beam covers a fairly large area and depth. Averaging over a larger area, more grain boundaries will be analyzed, increasing the Ca peak. However, Ca is an

extremely difficult element to measure with GD-MS due to several peak interferences and the higher concentration measured could result from both factors.

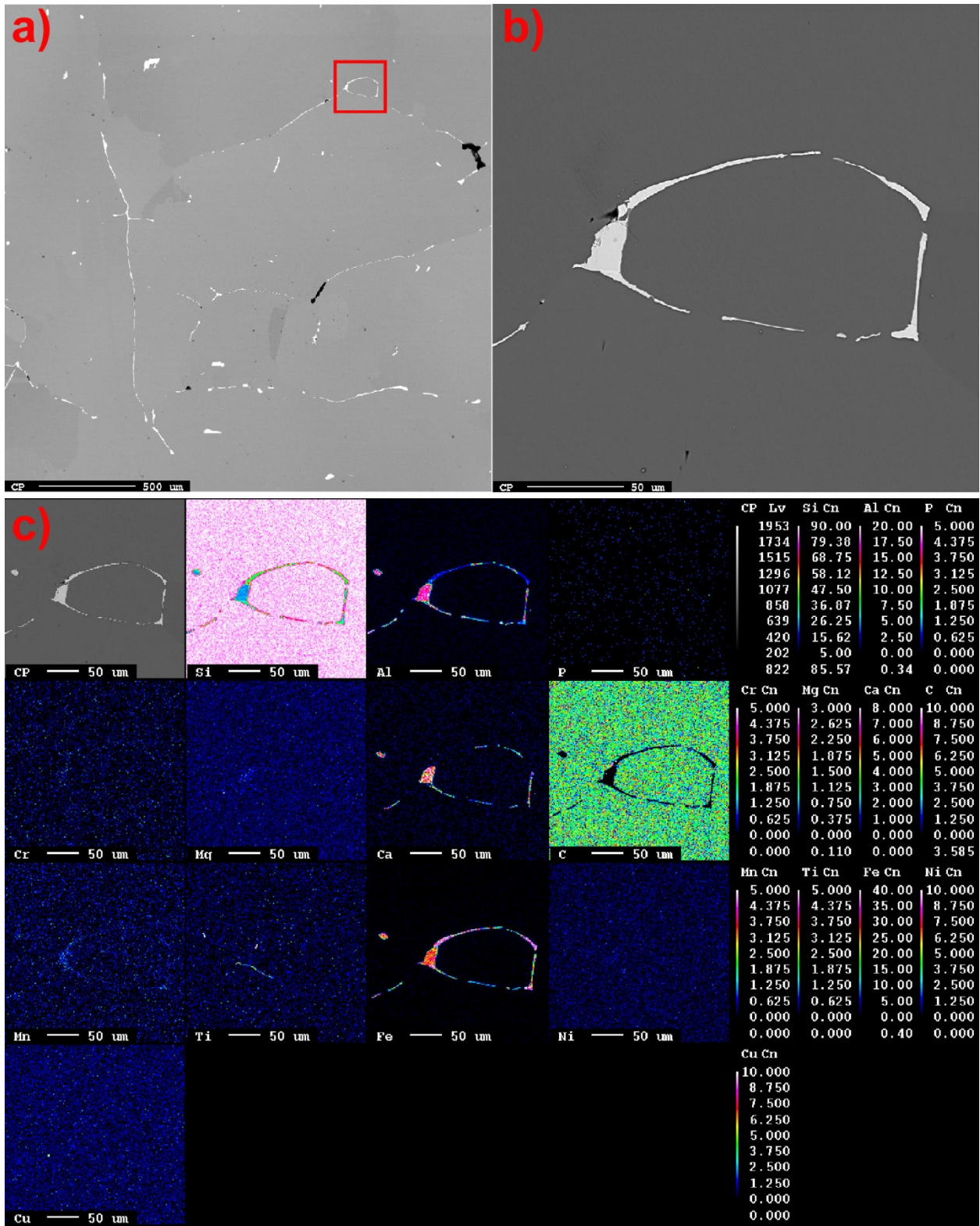


Figure 5.3 MG-Si SEM image (a) showing several silicon grains with impurities decorating grain boundaries. A selected sub-region (b) is analyzed by EDX (c): its chemical composition shows Al and Ca co-located with Fe and with some Ti. Three different areas are analyzed (a, d, g) and the same co-location pattern is observed (c, f, i). Concentrations are in mass percent.

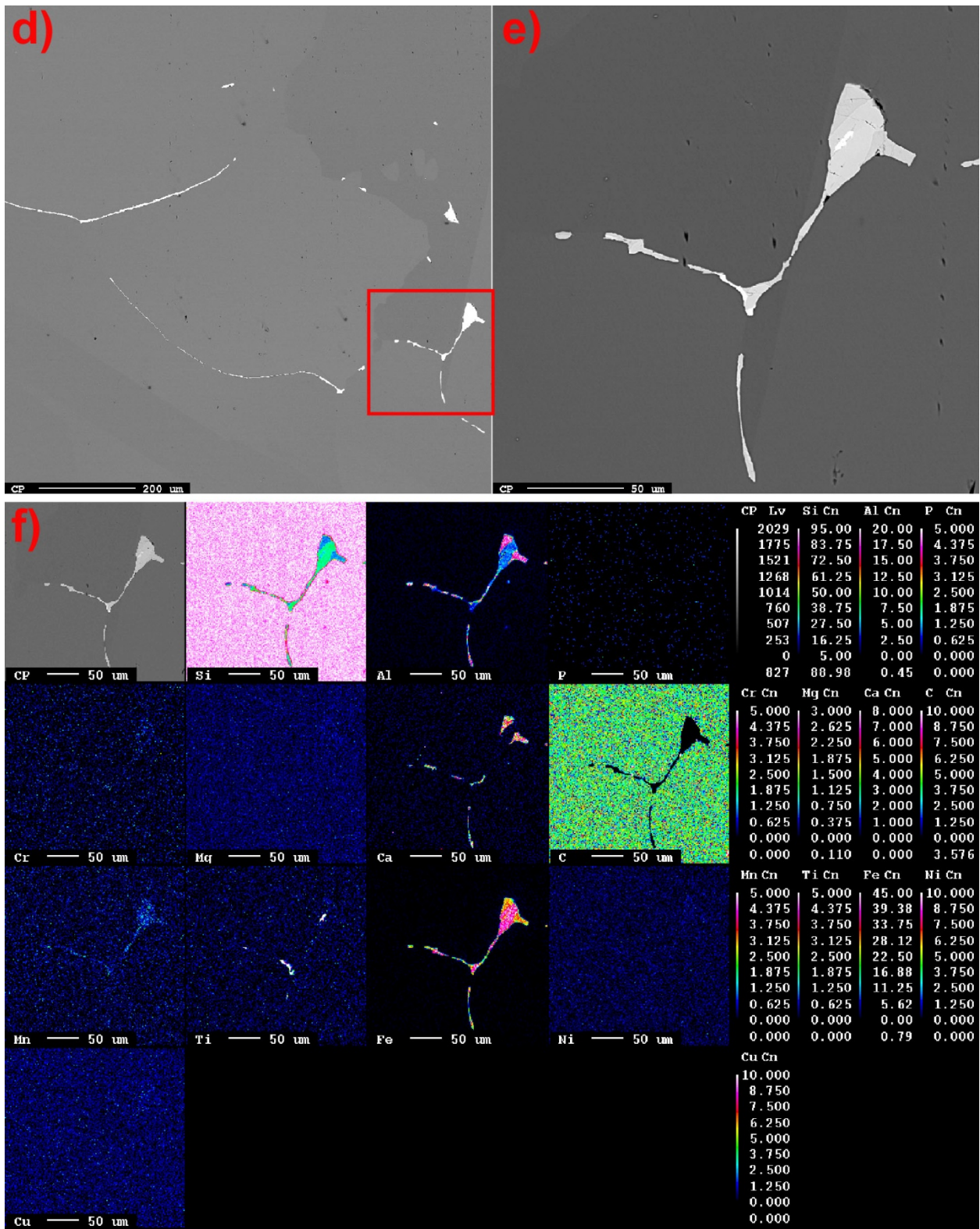


Figure 5.3 (cont.)

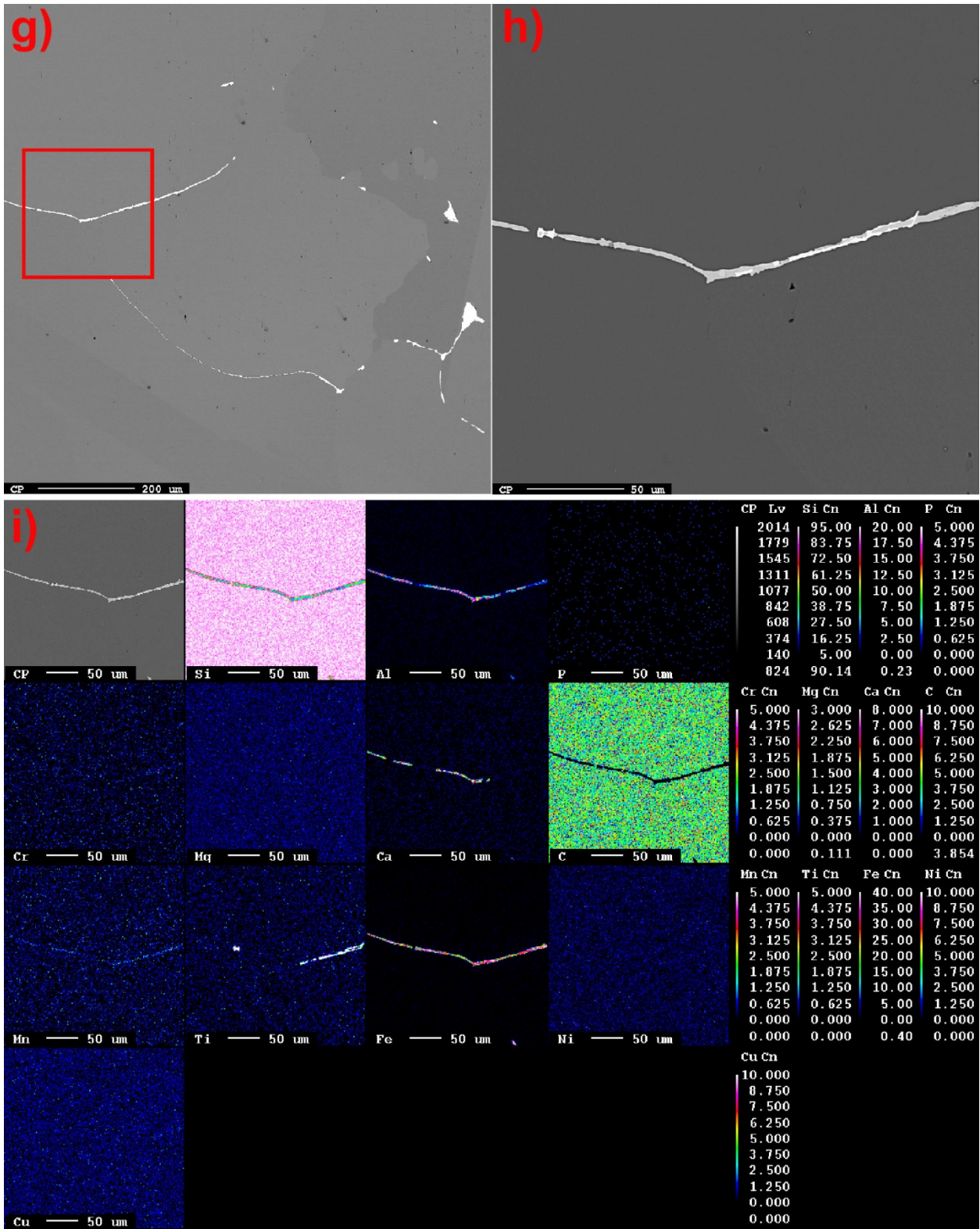


Figure 5.3 (cont.)

5.2. Discussion

Both crystallographic structures are relatively close to incorporating point defects. Most impurities segregate towards structural defects and grain boundaries where impurities either form mineral inclusions (quartz) or second-phase precipitates (silicon). Minerals in quartz are generally oxidized (*e.g.* oxidation state analysis presented in Chapter 3); in silicon, both reduced (silicides) and oxidized clusters can be detected [70].

SiCaAl intermetallic phases along silicon grain boundaries are detected by [117] (not found, referenced in [9]). CaSi_2 is also predicted to precipitate at grain boundaries and should act as an impurity collector [118]; for example, Ca addition before Si solidification is evaluated as a sink to remove phosphorus by [119]. However, impurity metal clusters analyzed by μ -XRF and μ -XANES in [70] suggest that co-location of Fe with slow diffusing species such as Ca, Ti, Cr, Mn, and Ni are often found in oxidized clusters rather than reduced silicides. Oxygen, with solid solubility of 10^{17} - 10^{18} cm^{-3} , can precipitate during cooling and behave as a sink for other impurities [70]; furthermore, an oxide is more stable than a silicide. From these references and our results, we infer that clusters present at grain boundaries might be oxidized in a silicate phase.

Impurity concentrations in the raw feedstocks play a key role in the purity of the tapped MG-Si. The carbothermic process will inevitably add impurities to the MG-Si and the concentration added by the raw feedstocks needs to be as low as possible, to keep the total amount within post-reduction refining possibilities. For this reason, certain types of quartzites (such as the one presented in Chapter 3) are discarded as the post-reduction refining would be too demanding to obtain SoG-Si purity. Especially, while an increase of metallic impurities can be cured by

directional solidification during silicon ingot growth, an increase in B and P is more difficult to control with post-refining methods.

When considering chemical analyses of impurities, Fe, for example, increases from low ppmw in the quartz to 1000 ppmw in the MG-Si. An increase in metallic impurities can be explained by the casting process, by the electrodes, and by the foundry environment. Casting is usually performed on moulds either of silicon material fines, iron, or of the metal produced. If an iron mould is used, the Fe content of the silicon produced is highly affected by the solidification environment, as we measured here. As Fe-Si alloys and MG-Si are commonly produced in the same plants, this possibility should be considered. Electrodes, with a steel casting, are known to be an unavoidable source of iron contamination as well as of other metals and carbon. Lastly, as previously also noted in [120], the foundry environment itself contributes to a spike in contamination. Mirroring the purification of crucible lining materials during multi-crystalline Si ingot fabrication [121,122], comparable cost-effective reductions in MG-Si impurity content may be achieved from purifying certain furnace/casting components and improving handling protocols.

5.3. Conclusions

Even though quartz is oxidized, silicon reduced, and they have different crystallographic structures, impurities behave similarly between them. They predominantly cluster along grain boundaries, where they either form minerals (given the right amount of time and species combinations), or second-phase precipitates.

The initial low- to sub- ppmw concentrations measured in the high-purity quartz are found to increase drastically after the carbothermic reduction process. This leads to infer that storage and handling before insertion in the submerged electric arc furnace, furnace and its electrodes, tapping, silicon casting are all responsible for the additional unintentional contamination found in the MG-Si.

6. Process Development: Quartz Leaching

Si-bearing rocks used as raw feedstock materials in SoG-Si production introduce unwanted impurities in the silicon refining process. As efficient removal before reduction would ease the post-reduction refining burden, we aim in this study at lowering impurity concentrations in dirtier, currently unexploited silica, to acceptable levels for direct use in UMG-Si production. For this reason, a low purity quartzite is considered and tested in parallel to two high-purity hydrothermal quartzes. Grain boundaries, commonly known as reservoirs of incompatible elements [41], are exposed via a selective comminution process, electric fragmentation. Once grain boundaries are exposed, we test four leaching recipes to remove impurities at room temperature.

6.1. Introduction

Nowadays high-purity silicon is sought for photovoltaic applications, yet its production and purification rely on its extraction from raw materials that are natural impurity getters. It is well established that what enters the submerged electric arc furnace must exit it, either via a gaseous phase or intermixed with the liquid silicon. Hence, high-purity quartzes with low trace element content, such as high-purity hydrothermal quartzes, are strategic commodities for silicon producers. Quartzite deposits are the most naturally abundant and cheapest source of silica. However, their high trace element concentrations disqualify them from being used for SoG-Si production.

The low solid solubility of impurities in silicon [123] predicts that most will segregate towards grain boundaries. Upon exposure by comminution methods, an acid treatment can remove them. In fact, acid leaching has been used to purify MG-Si since 1927, when Tucker suggested it as a viable method to purify MG-Si [124]. After his pioneering work, considerable effort was dedicated to test several etching recipes based on HCl, HNO₃, H₂SO₄, HF and their mixtures; with temperatures ranging between 50-80°C and etching times of 1-100 h [125-130]. However, comparison of results leads to believe that the origin of the MG-Si dictates the leaching outcome [129]; a comparison of impurity concentrations in MG-Si of different sources can be found in [15].

Similarly, quartz has a closed crystallographic structure to impurity accommodation and most segregate towards grain boundaries. While structural impurities cannot be easily removed [131], fluid inclusions spontaneously decrepitate upon heating releasing fluids [11]. Most of the metallic deleterious impurities found in the final solar cells are found in solid inclusions in the raw materials. Hence, as in the silicon case, leaching of quartz predominantly targets solid inclusions present along grain boundaries. Previous studies used combinations of either inorganic or organic acids. Within the reported etching recipes, HF, HCl, HNO₃, H₂SO₄, and H₂C₂O₄ (oxalic) acids are the most commonly used ones, even though H₂SO₄ or HCl can contaminate with SO₄²⁻ and Cl⁻, and therefore should be avoided. Experimental etching temperatures range between room temperature and 110°C, etching times range between a few minutes up to several hours. Table 6.1 summarizes some of the available studies and by no means is a complete literature survey.

Table 6.1 Examples of leaching recipes reported in the literature.

Initial Material	Tested Recipes	Etching time, Temperature	Reference
Boehmite bauxite (γ -AlO(OH))	7, 10M HCl	30°C	Patermarakis 1989 [132]
	4, 7, 10 M HCl	60°C	
	4, 4.5, 7, 9.3 M HCl	0-25 h; 90°C	
Pretreated ¹ quartz sand	H ₂ C ₂ O ₄	8 h; 30, 80°C	Ubalini 1996 [133]
Kaolin (silicate mineral)	H ₂ C ₂ O ₄ : 0.0015-0.25 M H ₂ SO ₄	6 h; 60, 90°C	Vegliò 1996 [134]
Kaolin	0.1, 0.25 M H ₂ SO ₄	30, 150 min; 70, 90°C	Vegliò 1997 [135]
Silica sand (α -quartz)	0.1-0.5 M H ₂ C ₂ O ₄ /K ₂ C ₂ O ₄	3 h-4 d; 25-100°C	Taxiarchou 1997 [136]
Quartz	H ₂ SO ₄	1 h; 20, 90°C	Vegliò 1998[137]
	H ₂ SO ₄	0-5 h; 90°C	
	H ₂ SO ₄ :H ₂ C ₂ O ₄	0-5 h; 90°C	
Ilmenite (FeTiO ₃)	HCl	7.5-120 min; 100- 110°C	Lanyon 1999 [138]
Quartz (silica sand)	H ₂ C ₂ O ₄	15 min-20 h; 80°C	Vegliò 1999 [139]
Kaolin	0.05, 0.1, 0.15 M H ₂ C ₂ O ₄	90 min; 100°C	Ambikadevi 2000 [140]
	0.15 M H ₂ C ₂ O ₄	5-30 d; 27°C	
	0.15 M H ₂ C ₂ O ₄ + FeSO ₄ ·7H ₂ O	15-90 min; 100°C	
	0.15 M H ₂ C ₂ O ₄ + 0.1-0.5 M H ₂ SO ₄	15-90 min; 100°C	
Chromatographic Silica	0.1% HCl	30 min, 18h	Barrett 2001 [141]
	0.1% HF	30 min, 18h	
Hematite (Fe ₂ O ₃), magnetite (Fe ₃ O ₄)	H ₂ C ₂ O ₄	10-120 min; 25-100°C	Lee 2006 [142]
Fe-oxides, Fe-clay minerals	0.05-0.5 M H ₂ C ₂ O ₄	0-120 min; 100°C	Lee 2007 [143]

¹ Natural material that has been purified by one or more of the following methods: floatation, physical separation, magnetic separation.

Kaolin + quartz	0.2, 0.6, 1 M H ₂ C ₂ O ₄	2 h; 80°C	Arslan 2009 [144]
Pretreated ¹ silica powder	0.2 M oxalic pH 1.5	4 h; 95°C	Lee 2009[145]
	0.2 M oxalic pH 2.5	4 h; 95°C	
	Aqua regia	8 h; 80°C	
	2.5% HCl:HF	8 h; 80°C	
	1% HCl:HF	8 h; 80°C	
Purified ¹ silica sand	H ₂ C ₂ O ₄	0-30 min; 50-95°C	Du 2011 [146]

The most considered variables are the recipe, the pH, the etching temperature and its duration. Most studies report using micrometer sized powders, yet no details are given regarding comminution techniques. Among the literature, Vegliò [139] evaluated grinding time (particle size) with respect to leaching efficiency. As noticed in the case of MG-Si, the initial material plays a key role in the interpretation of results.

6.2. Principles of Electrical Fragmentation

The basic physical principle exploited in electrical fragmentation is that rocks have very low tensile strength. As an example, quartzite can have compressive and tensile strengths of 222.5 MPa and 17.6 MPa, respectively [147]. Electrical breakdown causes tensile strain which in turn is fundamental to obtain electrical disintegration. High voltage pulses are discharged directly in the rock contacted by electrodes and surrounded by water. While the water acts as an insulator, the high current density waves are confined in the rock and travel between the electrodes leading to electrical breakdown in four consecutive steps occurring at supersonic velocity: first, creation of locally excited states (formation stage); second, intra-molecular bond breakage with local rock sublimation and formation of plasma channels (tree formation); third, plasma channel growth in

the anode-cathode direction (tree growth); fourth, as the electrodes are bridged, plasma channel expansion and surge in conductivity (electrical breakdown). This last stage can be followed by electrical disintegration if the channel expansion generates sufficient tension along its radial planes. The magnitude of the electrical field, the pulse energy, and the duration of the field are fundamental parameters that affect disintegration efficiency.

In quartz, an anisotropic semiconducting material, the direction of the principal conductive channel and the subsequent plasma capillary growth are influenced by rock integrity and by the presence of foreign minerals. Grain boundaries separating different mineral phases with different permittivity are generally mechanically weak, and their surfaces are more conductive enhancing plasma channel propagation, electrical breakdown and disintegration.

Detailed description of the theory of electrical fragmentation and of its application to mineral liberation can be found in [147-151].

6.3. Materials

Three types of Si-bearing raw feedstock materials were investigated. Two were high-purity quartzes. The first one is a hydrothermal quartz (HQ) currently used in SoG-Si production; details regarding this sample were provided in Chapter 4 (section 4.3.1). The second one is a hydrothermal vein quartz (HVQ) provided by Nordik Mining ASA (Oslo, Norway) still unexploited industrially, but promising for SoG-Si production due to its low trace element content. The third raw feedstock is a low purity quartzite (Q) currently used for MG-Si production; details regarding this sample were provided in Chapter 3 (section 3.1.3).

6.4. Experimental Procedure

All samples were provided in small lumps (a few cm in diameter). Initial untreated samples were collected before electrically fragmenting and leaching the rest of the batches. Powders of the untreated materials were prepared in a pre-cleaned and pre-conditioned agate mortar. ICP-MS analyses of the initial materials were used to evaluate the whole process and to control the impurity content through the different steps.

6.4.1. Electrical Fragmentation

As a comparative study, we fragmented all three quartz types to liberate grains of 0.3 mm (0.2-0.5 mm), the average grain size present in the quartzite. Electric fragmentation was performed at SELFRAG AG (Kerzers, Switzerland). The equipment has a high voltage power supply, high voltage pulse generator, a reaction chamber, and a process vessel. To ensure minimal contamination, the reaction chamber and process vessel were cleaned according to the following procedure, which was repeated before each different quartz batch. i) The process zone was showered with water. ii) The process vessel was filled with water and treated with 100 high voltage discharges. iii) The process vessel was filled with HVQ quartz and treated with 200 high voltage discharges. This step was used as a pre-conditioning treatment of the vessel. iv) The process zone was showered with water. v) The process vessel was filled with water and treated with 100 high voltage discharges. Following these vessel cleaning steps, fragmentation of the quartz was a two step process. The quartz was pre-crushed to ~2 mm with high voltage discharges (25 V applied to HVQ, 137 V to HQ, and 147 V to Q); fractions of the sample that were smaller than 0.5 mm were sieved from the coarse target material, which was then

fragmented to less than 0.5 mm. All fines produced were collected and later sieved to isolate 0.2-0.3 mm liberated grains.

6.4.2. Wet Etching

Four recipes were tested: organic aqua regia in two different dilutions, 20:1 DMF:SOCl₂; 3:1 DMF:SOCl₂; Na₂B₄O₇ in H₂O at its room temperature solubility limit; and 4:1 HCl:HF.

Anhydrous N,N-dimethylformamide (DMF), HCON(CH₃)₂; thionyl chloride, SOCl₂; and anhydrous sodium tetraborate, Na₂B₄O₇ all had purity ≥ 99% (Sigma-Aldrich, Oslo, Norway). HCl and HF were with semiconductor grade acids. The first three recipes were tested for 5 minutes, the last one for 30 seconds. For each etching experiment, 1 gram of quartz was inserted in 20 mL of solution at room temperature. After the etching step, each quartz batch was rinsed with deionized water and dried in air before being digested for ICP-MS analysis.

6.5. Results and Observations

Figure 6.1 depicts the three quartzes used in this investigation. Hydrothermal quartz has a milky-white colour due to a high concentration of microscopic fluid inclusions. Viewed in transmitted light (Figure 6.1a), it shows a variety of grain sizes. Subgrain formation, where a few large grains are surrounded by smaller ones, suggests fast re-crystallization due to high circulation of hydrothermal fluids. Grains have sharp corners and irregular edges; some overgrowth of smaller grains in larger ones is visible. A geological alteration is also confirmed by the abundance of intergranular H₂O-CO₂ fluid inclusions. Mica, muscovite KAl₃Si₃O₁₀(OH,F)₂, grains are visible.

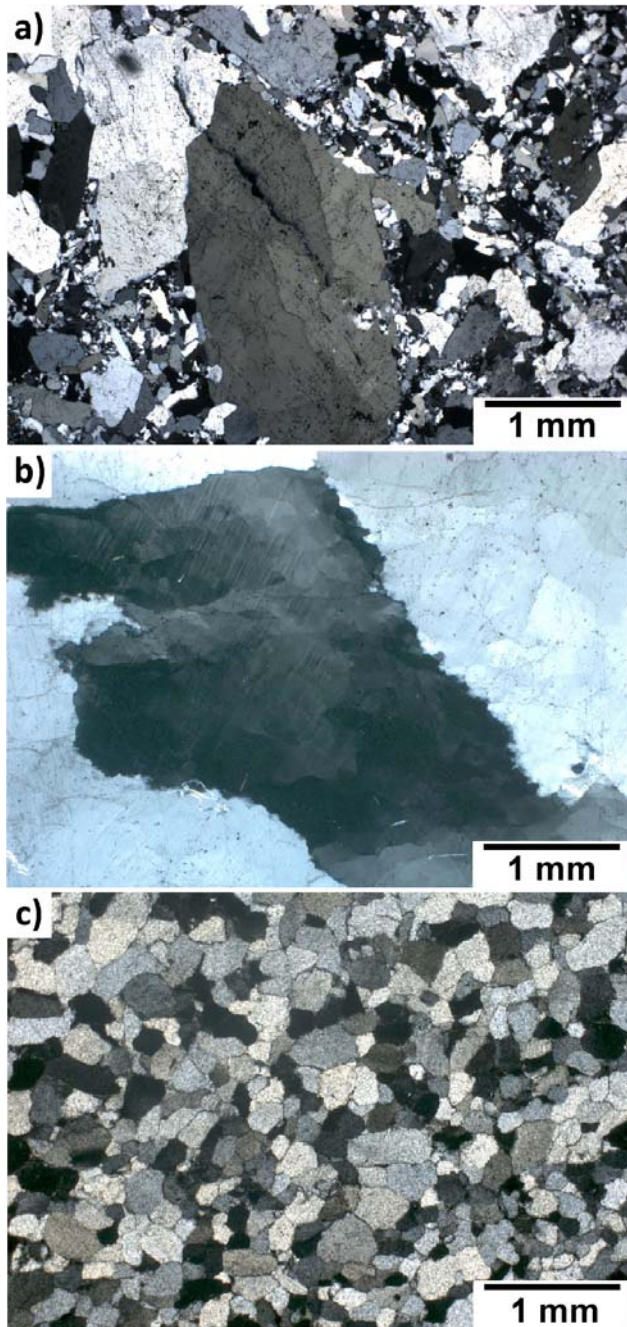


Figure 6.1 Transmitted light images of petrographic thin sections of a) hydrothermal quartz; b) hydrothermal vein quartz; and c) quartzite.

Hydrothermal vein quartz is glassy transparent. In transmitted light (Figure 6.1b), grains depict seriate interlobate texture and intra- and inter- granular cracks of several generations as well as fluid inclusion trails are visible. The quartz was subjected to geological alteration; this is inferred by the presence of bulging recrystallization, subgrain rotation recrystallization, and grain boundary migration recrystallization. Orthoclase, KAl_3SiO_8 , and Fe-rich muscovite, $(Fe,Mg)KAlSi_4O_{10}(OH)_2$, grains are visible and they mostly located at grain boundaries.

Quartzite is brown in colour; quartz crystals are medium-grained with discernible grains of foreign minerals (Figure 6.1c); co-presence of well-defined rounded or sharp edges and grain overgrowth imply local re-crystallization. Micas and other minerals are visible along grain boundaries.

6.1.1. Bulk Impurity Flow

Bulk impurity concentrations of the initial materials and of the post-treated ones were measured at two different times. Comparison of the ICP-MS blanks (Figure 6.2a) and of the USGS Diabase W-2 reference geomaterial (Figure 6.2b) tested in the two runs raised some ICP-MS comparability concerns.

Higher blanks were detected in the second round of experiments. This leads to infer that concentration values measured during the second run might be higher due to measurement error. However, throughout the second batch, this error is constant and values can be compared. Explicitly, the raw (initial) materials of the hydrothermal quartz (Figure 6.3a) and of the quartzite (Figure 6.3c) were measured during the first analytical round, all other analyses shown during the second. Moreover, in the hydrothermal vein quartz (Figure 6.3b), analyses of Al and Fe after sieving resulted in negative concentrations; these numbers were discarded as outliers.

ICP-MS analyses after each step of the process are depicted in Figure 6.3. Sample preparation is evaluated in the raw materials (yellow), after electrical fragmentation (orange), and after sieving (red). Impurity concentrations after electric fragmentation of hydrothermal vein quartz (Figure 6.3b) were not measured; rather, concentrations were measured only after sieving.

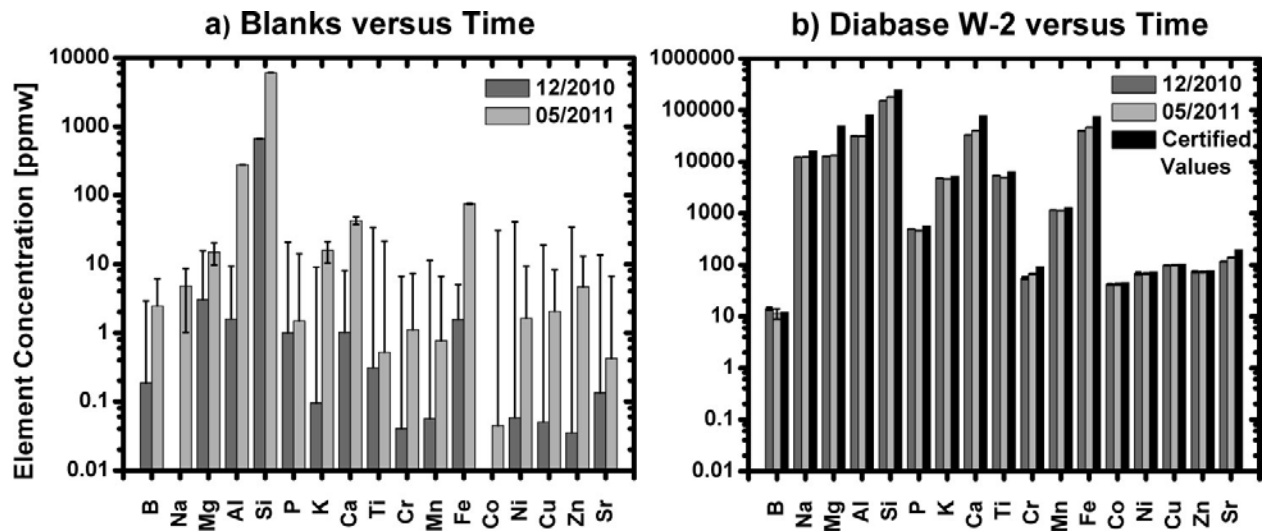
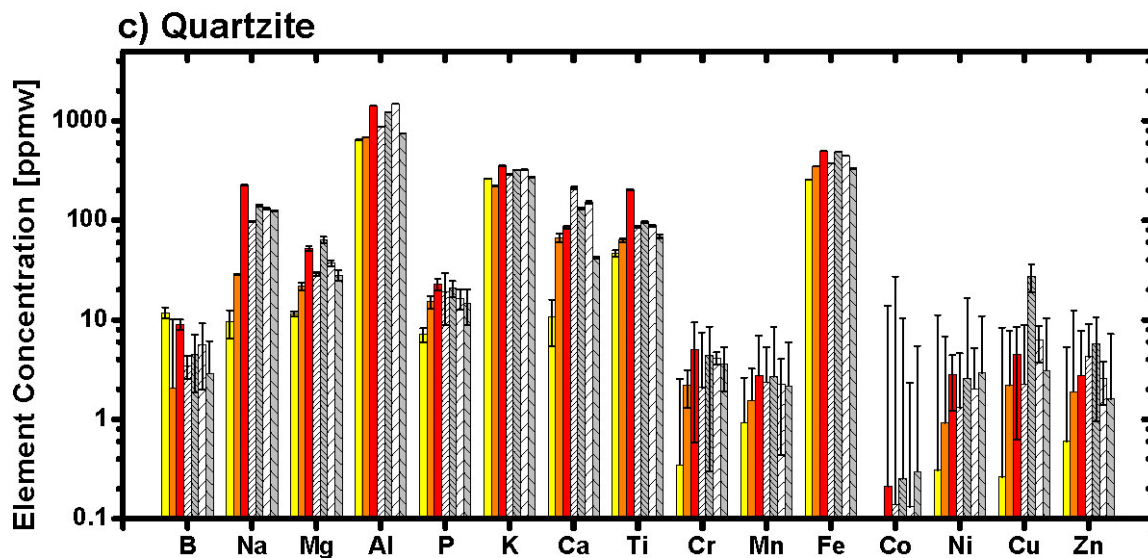
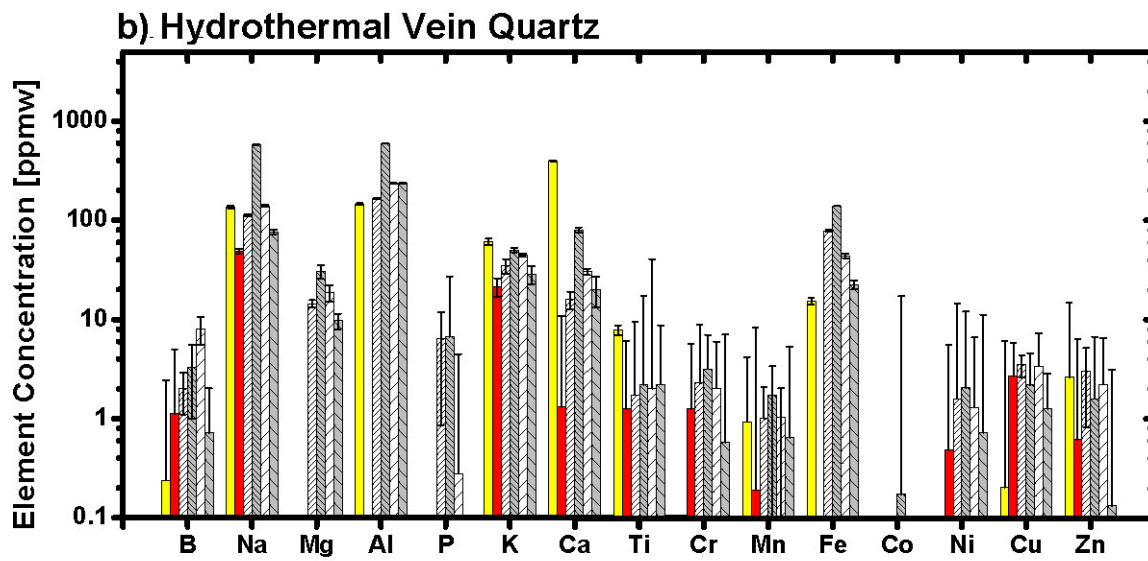
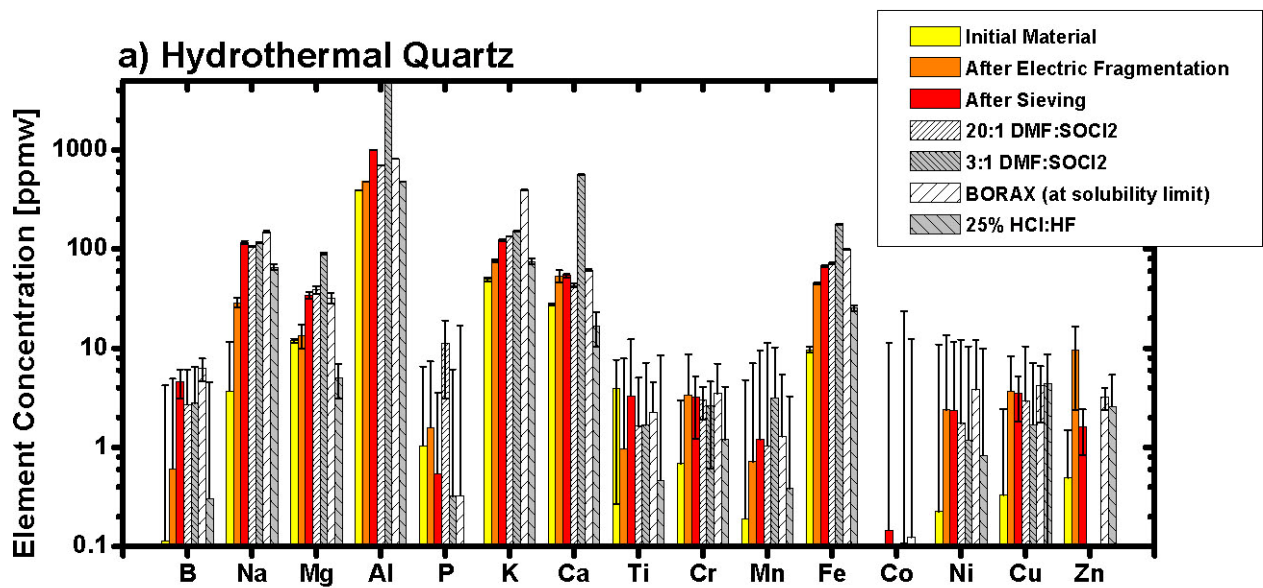


Figure 6.2 ICP-MS test blanks and b) USGS Diabase W-2 reference geomaterial. Comparison of two analytical measurements performed at different times.

Since measurement error might have affected the second ICP-MS round, the initial values of hydrothermal quartz (a) and quartzite (c) might lose comparability with respect to the process steps that followed. For this reason the fragmentation might seem to have caused contamination. Fragmentation is expected to add contamination as the electrodes are made of steel. Contamination from this type of process should be detectable in the hydrothermal quartz (a) rather than in the quartzite (c), as the former is a high-purity material and any contamination spike should be easily detectable. For this reason, the contamination given by fragmentation is higher in (a) than in (b). However, the fragmentation process should also liberate foreign minerals from the quartz matrix. By sieving, these impurities should be discarded. In fact, when comparing the initial value of hydrothermal vein quartz (b) to values after sieving, the clear trend is that impurity concentrations diminish, as expected. Yet according to (a) and (b) sieving is another source of contamination. Industrial implementation of this technique would easily avoid sieving contamination as sieves would be used only for a specific application, unlike the sieves used during this trial.

Of the four tested leaching recipes, “4:1 HCl:HF” is the one that removed most impurities even though it was performed at room temperature and the etching time was extremely short (30 sec). With this temperature-time choice, comparison with literature [145] would have predicted no impurity removal. The two different dilutions of the organic aqua regia (DMF:SOCl₂) gave very different results. When comparing concentrations after sieving and etching, “20:1 DMF:SOCl₂” shows a hint of impurity removal; probably longer leaching times, or higher temperatures would have increased the removal. “3:1 DMF:SOCl₂” showed a similar result in the quartzite, but it increased concentrations in all elements in the hydrothermal vein. Finally, “Borax”, at its room temperature solubility limit in water, behaved similarly to “20:1 DMF:SOCl₂” in the quartzite, and similarly to “3:1 DMF:SOCl₂” in the hydrothermal quartz.

Figure 6.3 ICP-MS analyses of the impurity concentrations in a) hydrothermal quartz, b) hydrothermal vein quartz, and c) quartzite, as the initial material (yellow) is electrically fragmented (orange), sieved (red) and finally leached. Four leaching recipes are tested (white and gray).



These results suggest that impurity removal cannot be thought of as pure elements (or its simple oxide) being removed, rather minerals that depending on crystal composition and exposed crystallographic surfaces will behave differently to the etching recipes. Minerals present in the hydrothermal quartz (predominantly muscovite) behave differently to the tested recipes than the ones present in the quartzite (predominantly feldspars). Hence, recipes should be tailored to the quartz deposit of interest. When materials tested are natural (*i.e.* geological samples as here), differences between foreign minerals present will lead to different etching results: previously reported results (*e.g.* references in Table 6.1) greatly differ among each other for this reason.

Industrial implementation of this process would require further investigations, especially in the following fields. First, after electrical fragmentation, the initial raw material will have sub-mm diameter, *e.g.* it becomes what industry defines as “fines”. Industry would need to implement the fragmentation process to minimize contamination and material loss, as well as to guarantee breathing protection from silica fines. Secondly, post-etch fines cannot be inserted directly into a submerged electric arc furnace without being compressed into pellets/briquettes. If fines are inserted, gases can get trapped in the furnace eventually leading to explosions. Moreover, pellets/briquettes need to maintain compactness until they reach the bottom of the furnace to avoid formation of a sticky layer near the furnace top that would also prevent gas escape.

6.6. Conclusions

We observed in Chapter 3 that trace elements are mainly found in mineral inclusions located at grain boundaries. With the end goal of expanding the usable range of raw feedstocks used for SoG-Si production to dirtier and more abundant quartzites, we used a selective fragmentation technique, electrical fragmentation, to expose the grain boundaries and then leach them to

remove impurities. The selective fragmentation step proved to be the key in removing impurities via leaching: a few seconds of room temperature acid treatment, rather than hours at relatively high temperatures proved enough to remove noticeable amounts of impurities.

Within the time-temperature and chemistries chosen for these leaching tests, the inorganic, acidic leach proved to be the most effective one with respect to both the organic aqua regia and the Borax. Recipes targeting selected minerals could achieve even better impurity removal rates.

7. Conclusions

Using synchrotron-based microprobe techniques and bulk chemical analyses, we investigated Fe, Ti, and Ca starting from Si- and C- bearing raw feedstock materials to MG-Si, via carbothermic reduction.

We conclude that the investigated impurities, before and during the early stages of the carbothermic reduction process, are primarily embedded in foreign micron- or sub-micron-sized mineral inclusions. These minerals are primarily located at structural defects (such as grain boundaries) and they dictate impurity oxidation states. While the chemical states of impurities vary, they are generally oxidized (*e.g.*, Fe^{2+} , Fe^{3+}). Particles containing Cr, Mn, Fe, Ni, Cu, K, and/or Zn are also detected. We found that bulk impurity concentrations are directly correlated to the geological formation history of the quartz: pegmatitic and hydrothermal quartz have fewer impurities than quartzite. In C-bearing compounds, Ca typically follows wood veins. In wood, Fe and Ti are diffused uniformly. In contrast, charcoal samples can contain particles of Fe, Ti, and/or Ca. The overall impurity content in the pine charcoal sample is higher than in the pine woodchip, suggesting that the charcoalization process introduces unintentional contamination.

During later stages of the reduction process, the host foreign minerals decompose, melt, and then fully dissolve, and impurities become part of the silica melt. Yet, due to the immiscibility of impurity oxides in the silica melt, impurities tend to cluster along solid-liquid interfaces between crystalline and molten silica; and at higher temperature, along liquid-gas interfaces between silica and gaseous inclusions. Contrary to thermodynamic expectation, Fe is found oxidized until

late in the reduction process; as the silica melt protects it from gases present in the furnace, hence minimizing its reduction, only partially measured at high temperatures.

After reduction, the initial low- to sub- ppmw concentrations measured in the precursor high-purity quartz increase drastically in the MG-Si. The refining process is responsible for the increased contamination. Yet, most impurities are clustered at grain boundaries and a leaching process could remove them.

After analyzing the extraction process, we conclude that industry should take advantage of the preferential clustering of impurities in foreign minerals along grain boundaries in the raw feedstock materials. A selective fragmentation technique, electrical fragmentation, can be used to expose grain boundaries and a leaching process can remove deleterious impurities. The selective fragmentation step proved to be a key step in removing impurities via leaching: a few seconds of room temperature acid treatment, rather than hours at relatively high temperatures as so far reported, are enough to remove noticeable amounts of impurities. This pre-reduction process would lift the burden from post-reduction refining processes nowadays heavily exploited, leading to an economical benefit.

8. Future Work

This thesis covered a few steps of the long impurity journey in the solar cell silicon value chain. A few suggestions for the next steps are:

- *Analytical implementations (Chapter 2)*

First, μ -XRF/ μ -XANES – surface contamination: throughout investigations, metallic iron (a.k.a. unwanted contamination) proved difficult to get rid of. Unfortunately, most equipment is made of stainless steel, whether it is equipment to polish surfaces or to measure impurities. Commonly, before measurements, one would perform an acidic etch to remove such unwanted contamination. However, an acid etch might interfere with the oxidation state of surface particles, especially when using surface-sensitive techniques. Implementing sample preparation protocols is fundamental in obtaining reliable and repeatable results. The protocols presented in this work should be further investigated to rule out all possible forthcoming problems. Pre-sputtering and vacuum measurements might be an alternative solution; however, the beamlines used in this thesis were not equipped for such measurements.

Second, ICP-MS – reliability: each ICP-MS measurement proved different and this caused confusion, and interpretation of results became difficult. Naturally crystallized materials have homogeneity effects that will affect measurements; however, it is of fundamental importance to rule out unintentional contamination due to powder preparation, digestion, dilution, and measurement. This work suggests a sample preparation method. This method should be further implemented and tested to ensure reliability of further analyses.

- *Raw feedstock materials choice (Chapter 3)*

Each chapter presented different raw materials. It would be scientifically important to gain an overview perspective over the entire process using the same raw materials. The reason is that impurities, as previously mentioned, are highly affected by the host

minerals they are embedded in: using the same initial raw feedstock would allow minimizing differences in experimental conditions.

- *Re-designing the carbothermic reduction simulated process (Chapter 4)*

Obtaining Si in a laboratory scale furnace proved very challenging. The reduction process presented here lacked the final reducing step: building up enough intermediate species required to form Si(l).

First, as the real submerged electric arc furnace works as a counter-reactor furnace in dynamical cycles of stocking, charging, and tapping; to be realistic, a laboratory scale experiment should take this into account.

Second, in the attempt of evaluating oxidation states during the reduction process, different quenching effects should be evaluated. High temperature *in-situ* studies are extremely difficult to perform, especially if the reaction environment is reactive; this might be an interesting scientific future path to explore.

- *Unintentional impurities during reduction (Chapter 5)*

We showed how MG-Si produced from high-purity quartz had thousand ppmws of impurities. This is due primarily to the furnace, its lining, the environment and, especially, to the electrodes and the casting methods. All these would require further investigations.

- *Selective fragmentation: next steps (Chapter 6)*

To effectively remove impurities from Si-bearing raw feedstocks, quartz selective fragmentation proved to be a key process step before leaching. It exposed grain boundaries allowing the leaching to be as effective as possible. As such, it should be further pursued in conjunction with the testing of acidic recipes. First, each batch of raw materials will have predominance of one or only few minerals. It is currently difficult to envision one single etching recipe that might work with all raw feedstocks. Recipes should target specifically these minerals. Second, before exploring high temperature options, leaching in an ultra-sonic bath should be considered.

- *From quartz to SoG-Si*

We investigated selected impurities, from quartz to MG-Si. SoG-Si is a few refining steps further, though it is being used for PV applications, rather than MG-Si. These steps need to be evaluated in connection to the raw feedstock materials, a link still missing. Toward this goal, a strong industrial partnership is needed as Si produced in a laboratory scale furnace will fail to be representative.

Appendix A

Thick Section Preparation for μ -XRF Investigations

When performing μ -XRF analyses, as well as other chemical microscopic investigations, such as electron beam micro analyses, samples with flat surfaces are required. Moreover, when mapping the chemical composition of the specimen on a micron scale, potential sources of contamination during the specimen preparation should be evaluated carefully. Unfortunately, the preparation of 30 μm or 300 μm rock sections requires specialized tool that have metallic components. In light of this, it is fundamental to follow the same preparation for all samples investigated, minimizing possibilities of random contamination and allowing comparison between samples.

At the synchrotron, only 300 μm sections were investigated to preserve fluid inclusions. The following procedures were used to prepare all samples analyzed by μ -XRF. They are the result of discussions with Dr. A. Lanzirotti, scientist at beamline BNL X26A; and with Dr. M. DePangher at Spectrum Petrographics, Inc (Vancouver, WA). The 30 μm thin sections were prepared both by Spectrum Petrographics, Inc (Vancouver, WA) and by the Geology department at NTNU (Trondheim, Norway). In both facilities, thin sections were prepared following similar procedures, yet these sections, mostly used for optical investigations have not been evaluated as the 300 μm ones.

A.1. 300 μm Thick Section Preparation

Two different preparations are investigated depending on the characterization planned: the first one is for μ -XRF measurements only (one side polished) where the section remains attached to the glass slide; the second one is optimal for a combination of μ -XRF and μ -XRD (double side polished), where the section is detachable from the glass slide.

A.1.1. μ -XRF (one side polished)

- Sample is embedded in resin (Scotchcast electrical resin)
- Resin is cured; then cut to expose target face
- Target face is exposed and ground flat with 100 grit and 180 grit fixed diamond disks (diamonds embedded in Ni-brass alloy) and then lapped with 25 micron aluminum oxide on a cast iron lap
- Target face is then "painted" with Scotchcast and cured
- Target face is finished using 40 micron fixed diamond (diamonds bonded with Ni-alloy to resin backing)
- Finished target face is glued (Elmers Crazy superglue) to a slide (Suprasil #2 slides from Heraeus Amersil)
- Most of the billet is cut away with a thin diamond blade
- Grinding:
 - First grinding step is with a bronze-bonded diamond cup grinder
 - Second step is 25 micron alumina on cast iron lap
 - Third step is 18 micron alumina on cast iron lap

- Fourth step is 10 micron fixed diamond bonded with Ni-alloy to a resin backing
- Polishing with 1/2 micron diamond paste on a felt cloth

A.1.2. μ -XRF – μ -XRD (double side polished)

This procedure was discussed and optimized; however, it was never used in this thesis. It is reported here for reference and future improvements.

- Sample is embedded in resin (Scotchcast electrical resin)
- Resin is cured; then cut to expose target face
- Target face is exposed and ground flat with 100 grit and 180 grit fixed diamond disks (diamonds embedded in Ni-brass alloy) and then lapped with 25 micron aluminum oxide on a cast iron lap
- Target face is then "painted" with Scotchcast and cured
- Target face is finished using 10 micron fixed diamond (diamonds bonded with Ni-alloy to resin backing)
- Finished target face is glued (Elmers Krazy superglue) to a slide (Suprasil #2 slides from Heraeus Amersil)
- Most of the billet is cut away with a thin diamond blade
- Grinding:
 - First grinding step is with a bronze-bonded diamond cup grinder
 - Second step is 25 micron alumina on cast iron lap
 - Third step is 18 micron alumina on cast iron lap

- Fourth step is 10 micron fixed diamond bonded with Ni-alloy to a resin backing
- Polishing with 1/2 micron diamond paste on a felt cloth

A.2. Cleaning procedure prior to arrival at the Beamline: quartz thin section with/out slide

- All steps performed with nitrile gloves and Teflon tweezers
- [Removal of slide from quartz section: acetone ultrasonic bath ~10-15 min]
- Solvent cleaning in ultrasonic bath:
 - 10 min in acetone
 - DI H₂O rinse
 - 10 min in ethanol
 - DI H₂O rinse
 - 10 min in isopropanol
 - DI H₂O rinse
- Thin section wrapped in clean room cloth and inserted in a new sealable plastic bag

A.3. Mounting the quartz thin section with/out slide [at the Beamline]

- All steps performed with nitrile gloves and Teflon tweezers

- Space used for mounting on the table at the beamline covered with large Kimwipe paper
- Sample holder available at the Beamline cleaned with acetone
- Thin section mounted on the sample holder using Kapton tape only before characterization starts
- Sample holder is immediately inserted in the beam for data collection

Appendix B

From μ -XRF counts to ppmw

Measured μ -XRF counts [cts/s] of a specific element can be converted to parts per million weight [ppmw] within the sample matrix. This implies converting a two dimensional map to a surface concentration [$\mu\text{g}/\text{cm}^2$]. Given the nature of the interaction process of X-rays with matter, this two dimensional map contains three dimensional information. Assuming the information depth is equivalent in average to one attenuation length, the two dimensional concentration can be expanded to a volumetric concentration [$\mu\text{g}/\text{cm}^3$]. From here, the final conversion to [ppmw] is straightforward. A detailed description of analysis and a rigorous mathematical approach can be found in [83].

The Matlab code and its embedded Gaussian function are provided below to replicate this conversion. The code aims at performing the conversion from [cts/s] to [ppmw] after having subtracted noise and taken into account measurement effects. The approach of the algorithm can be summarized as follows. The μ -XRF map is loaded and dead time corrected [cts/s]; with the pixel data, a histogram of the element of interest (frequency versus cts/s) is generated. A noise peak is created by mirroring the left side of the histogram peak onto its the right side. This new peak is fitted with a Gaussian distribution (frequency versus cts/s), which represents noise and it is subtracted from the initial area, giving the total detected element. This area represents the metal signal in [frequency]. This value is weighted by the pixel intensity [cts/s] and the average [cts/s] is computed by the number of scanned pixels [cts/s/Io]. This value is normalized by the average Io and dwell time [cts/s/s/Io]. NIST [$(\mu\text{g}/\text{cm}^2) * (\text{cts}/\text{s}/\text{Io})$] standards are used to

convert to $\mu\text{g}/\text{cm}^2$. Assuming only one attenuation length [cm], the concentration of the element [$\mu\text{g}/\text{cm}^3$] is computed. Lastly, this concentration is converted from $\mu\text{g}/\text{cm}^3$ to ppmw by using the matrix density.

B.1. Main Code

```
%% Constants
clear all
close all
clc
warning off

% pre-loaded functions (do not modify)
[map1832] = loadSingleXRFFMap; % 2008-09 Standards 1&2 multi 000 7.3keV DT.xrf
[map1833] = loadSingleXRFFMap; % 2008-09 Standards 1&2 multi 003 7.3keV DT.xrf

norm_Ca = XRF_NIST(map1832,8,5)
norm_Ti = XRF_NIST(map1833,10,6)
norm_Fe = XRF_NIST(map1833,5,9)

% norm_Mn = XRF_NIST(map1832,6,8)
% norm_K = XRF_NIST(map1833,12,4)

%% these values need to be modified according to the input files

[sample] = loadSingleXRFFMap;
element = 5; % check map header (sample.header)
% Ca = 8; Ti = 10; Fe = 5
params.opts_fit = 'fit_gauss'; % user chooses between 'no_fit' or 'fit_gauss'
alpha = 40.3576*10^-4; % [cm] Fe in SiO2 at 45deg incoming beam
% alpha = 14.6819*10^-4; % [cm] Ti in SiO2 at 45deg incoming beam
% alpha = 8.32474*10^-4; % [cm] Ca in SiO2 at 45deg incoming beam

normalization = norm_Fe; % choose from norm_Ca, norm_Ti, norm_Fe
bin = 1; % bins width in the histogram in [XRF cts/s]

%% nothing below this line should be modified

close all

A = 6.0221e+023; % [atom/mol] avogadro's number
density = 2.634; % [g/cm3] SiO2 density
% pixel = 7*7; % [micron^2] pixel area
% beam = 6*6; % [micron^2] beam area (100 x 50 slits)

el = sample.channel{element};
```

```

size_el = size(el,1)*size(el,2); % Map size (# of pixels in map area)

dwell = sample.dwell/1000; % [s] dwell time of the map
avg_Io = mean(abs(sample.Io)); % average Io

params.bin = bin;
params.normalization = normalization;
params.dwell = dwell;
params.avg_Io = avg_Io;
params.size = size_el;
params.alpha = alpha;
params.A = A;
params.density = density;

% [norm_sample] = dwellTimeAndIoCorrection(sample, 'PIP_XRF_dir'); % Dwell-I0 correction

[ppmw,a1,b1,c1] = XRF_GaussianFit(el(:),params);

% Norm_map = norm_sample.channel{element}*normalization; % [microgr/cm2]
% XRF Map Normalization

figure
    surf(el) % Iron; x-y: map area; z axis: [microgr/cm2]
    % az = 90;
    % el = 90;
    % view(az, el)
    % colormap (flipud(jet))
    % axis([0 size(el,2) 0 size(el,1) 0 max1_Fe])
    % set(gca,'FontName','Times','FontWeight','bold','FontSize',25)
    % xlabel('Pixels','FontWeight','bold','FontName','Times','FontSize',25)
    % ylabel('Pixels','FontWeight','bold','FontName','Times','FontSize',25)
    % zlabel('Intensity [\mug/cm^2]','FontWeight','bold','FontName','Times','FontSize',25)
    % title('\mu-XRF Map -- Iron','FontWeight','bold','FontName','Times','FontSize',30)
    % colorbar

g = fspecial('gaussian',[10 10],5);

% el_thresh = el;
% el_thresh(el<(b1+c1))=0;

el1 = imfilter(el,g,'replicate','same');
el1 = imfilter(el1,g,'replicate','same');

%mask = roicolor(el,b1+c1,max(el(:)));
%imagesc(el1.*mask);
%el_thresh = el1;
%el_thresh(el<(b1+c1))=0;
%imagesc(el_thresh)

el1max = colfilt(el1,[10 10],'sliding',@max);

```

```

el_ind = find(el1max==el1 & el>(b1+c1));
[ci,cj]=ind2sub(size(el1),el_ind);

figure; surf(el,'LineStyle','none');
hold on; plot3(cj,ci,el(el_ind),'og');
axis([0 400 0 200 0 1000]);

col{1}='og';
col{2}='ob'; col{3}='om'; col{4}='oy'; col{5}='oc';

nclust=3;
kk=kmeans(el(:),nclust);
kkimg = reshape(kk,size(el));
figure; imagesc(kkimg);

kkmask = roicolor(kkimg,2,3);
kklabel = bwlabel(kkmask);

for bb=1:max(kklabel(:));
    clear dot_ind
    dot_ind = find(kklabel==bb);
    dot_area(bb) = length(dot_ind);
end

figure; imagesc(el); hold on;
for ii=1:nclust;
    clear inds ki kj
    inds = find(kk==ii);
    [ki,kj]=ind2sub(size(el),inds);
    plot(kj,ki,col{mod(ii,5)+1});
end

```

B.2. Gaussian Function

```

function [ppmw,a1,b1,c1]=XRF_GaussianFit(elem,params,a1,b1,c1);

med_el = median(elem(:));
max_el = max(elem(:));
ratio_el = round(max_el/med_el);

figure(1); hold on;
% hist(elem(:),ratio_el*100);
% [n,m]=hist(elem(:),ratio_el*100);

% x axis (m): bins in [XRF cts/s]; bin width = 1 XRF cts/s;
% y axis (n): pixel frequency;
bin = params.bin;
bin_width = 0:bin:max(elem(:));
hist(elem(:), bin_width);

```

```

[n,m]=hist(elem(:),bin_width);
max_yrange = max(n)+10;
axis([0 2*med_el 0 max_yrange]);
xlabel('XRF cts/s'); ylabel('pixel frequency')

switch params.opts_fit
case 'fit_gauss'
    [max1_y,max1_x] = max(n);
%     manual_max = 3034; % on y axis
%     max1_x = find(n==manual_max); %in pratica max1_y indice == find(n==manual_max)

    pt_list_x_left = m(1:max1_x);
    pt_list_x_right = m(max1_x)+(m(max1_x)-pt_list_x_left);

    pt_list_y_left = n(1:max1_x);
    pt_list_y_right = n(1:max1_x);

    pt_list_x = [pt_list_x_left,pt_list_x_right];
    pt_list_y = [pt_list_y_left,pt_list_y_right];

    figure(2);
    plot(pt_list_x,pt_list_y,'o')
    xlabel('XRF cts/s'); ylabel('pixel frequency');
    title('Generated Noise peak -- Left: initial noise data; Right: mirrored data')

%% Gaussian Fit

if nargin<3;
    figure(2);
    cfit = fit(pt_list_x',pt_list_y','gauss1');

    cfit
    a1 = cfit.a1;
    b1 = cfit.b1;
    c1 = cfit.c1;
end

figure(1); hold on;
gauss_fit = a1.*exp(-((m-b1)./c1).^2);
plot(m,gauss_fit,'-r','LineWidth',3);
axis([0 2*med_el 0 max_yrange]);
xlabel('XRF cts/s'); ylabel('pixel frequency');
title('Gaussian fit of Noise superimposed on the initial histogram')
%% Noise subtraction = Method 1

data_difference = n - gauss_fit; % detected signal minus noise signal
figure(3);
hist(elem(:),bin_width); hold on % total detected signal of metal
plot(m, gauss_fit, '-r', 'LineWidth',3); hold on % noise signal detected
plot(m, data_difference, '-g', 'LineWidth',3); hold on % real metal in the sample
axis([0 2*med_el 0 max_yrange]);

```

```

xlabel('XRF cts/s'), ylabel('pixel frequency');
legend('Initial Content', 'Noise', 'Noise Subtracted')

% real metal: difference between area of histogram - area of noise
% over the entire sampled area
real_metal = sum(data_difference.*m); % [(pixel frequency)*cts/s]

% size of map [total number of spots where data was taken]
size = params.size;
% average total metal content per unit flux in [cts/s/lo]
avg_metal = real_metal/size

dwell = params.dwell;
avg_lo = params.avg_lo;
metal = avg_metal/dwell/avg_lo;

case 'no_fit'

data_difference = n; % real metal in the sample = total detected signal [cts/s]
real_metal = sum(data_difference.*m); % [(pixel frequency)*cts/s]

% size of map [total number of spots where data was taken]
size = params.size;
avg_metal = real_metal/size % [cts/s/lo]

dwell = params.dwell;
avg_lo = params.avg_lo;
metal = avg_metal/dwell/avg_lo;

a1 = [];
b1 = [];
c1 = [];
end

%% Information depth:

normalization = params.normalization;
alpha = params.alpha;
A = params.A;
density = params.density;

%% [micrgr/cm2] to [ppmw] Conversion:

Normal = metal*normalization; % [microg/cm2]

Vol = Normal/alpha; % [microg/cm3]

gcm3 = Vol*(10^-6); % [g/cm3]

ppmw = gcm3/density*1000000 % ppmw

```

Appendix C

ICP-MS Preparation and Analysis

C.1. Sample Preparation

Quartz, as used in this thesis, is a natural mineral, industrially exploited for metallurgical and solar grade silicon production. All samples, being of industrial interest, were provided without a mining, transporting, or handling history. For this reason, standard procedures to pre-clean and prepare powders were evaluated and implemented. Moreover, etching recipes to digest samples were also evaluated.

C.1.1. Initial Cleaning

The initial quartz chunks are cleaned from previous unknown treatments (mining, transporting) and/or handling. An acidic etch ($\text{HNO}_3\text{:HF}$, 9:1) is used to remove both metallic and organic contamination on the surface, followed by a deionized water rinse. The etch length is unimportant as far as it is long enough to etch off a few μm of quartz. If instead, for research purposes, the “as is” quartz needs to be evaluated, a solvent cleaning procedure removes only organic material deposited on the samples, such as contamination due to handling with bare hands or containers used to store samples prior to the investigation. An ultrasonic bath of acetone, followed by ethanol, and finally by isopropanol is standard. Each step is followed by a deionized water rinse. In both cases, quartz pieces are allowed to dry before proceeding to the next preparation steps.

C.1.2. Crushing Quartz Pieces

If the initial quartz lumps are big (~ tens of cm in diameter), a WC jaw crusher is used to fragment them into smaller pieces (~ few cm), suitable for either mechanical crushing (such as a vibratory disc mill) or electrical fragmentation. A WC jaw crusher is preferred over a conventional stainless steel crusher to minimize metallic contamination. The WC blades of the crusher are wiped with acetone; the crusher is cleaned with compressed air, and then conditioned with material from the same quartz batch. Only quartz lumps are collected; powder produced during this crushing step is discarded.

C.1.3. Powder Preparation by Vibratory Disc Mill (Method 1)

A WC vibratory disc mill is subsequently used to prepare quartz fine powder. The disc mill is cleaned with acetone and conditioned with material of the same batch, before preparing the powder used for chemical analyses. Once the powder is ready, it is collected in silicone closed tubes. This method is preferred over the next one, when a big batch of material is being prepared. As in the case of the jaw crush, a WC disc mill is preferred over a stainless steel one when transition metals are of analytical interest. This method is preferred over the next one when large quantities of powder are being prepared.

C.1.4. Powder Preparation by Agate Mortar (Method 2)

The cleanest way to prepare a powder is by using an agate mortar. To ensure cleanliness of the mortar, the inner surface and the pestle are cleaned with HCl to remove all previous unintentional contamination traces. This is followed by preparing powder of SiO₂ (99.9%) glass beads and by repeating this step three times to condition homogeneously (and in a repeatable manner) the mortar. The SiO₂ powder is removed by an acetone rinse. Depending on the quantity

of sample available, it is suggested to condition the mortar with the sample of interest. This can be done by preparing powder of the sample, by discarding the powder, and by collecting powder only after the third batch. If more samples need to be prepared, the mortar needs to be cleaned between each sample with the procedure described above. Powders are stored in contamination free containers (plastic tubes with caps generally work) until digestion.

C.1.5. Powder Preparation by Electrical Fragmentation (Method 3)

This sample preparation method is described in Chapter 6.

C.2. Digestion and Dilution

Acidic etch recipes, used for quartz digestion, are designed for specific quantities of powder; hence, samples are weighted before digestion (35 mg). Here, three different strengths of HF:HNO₃ are investigated:

- HNO₃ (1.73 mL) + HF (0.5 mL);
- HNO₃ (1.73 mL) + HF (1.0 mL);
- HNO₃ (2.5 mL) + HF (1.0 mL).

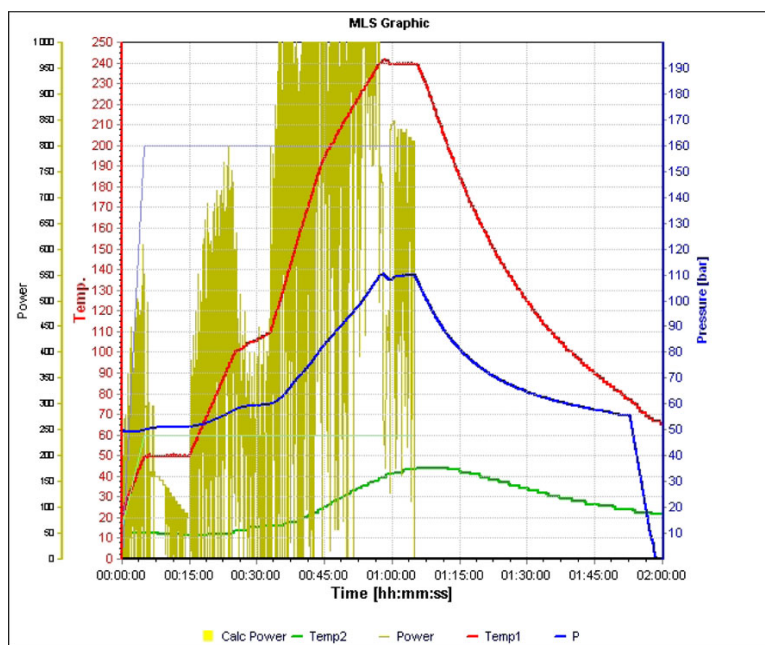


Figure C.1 Autoclave temperature (red) – pressure (blue) profile.

These recipes digest quartz at appreciable rate when heated. For this reason, each test tube was then heated in a controlled temperature-pressure vessel according to Figure C.1. Samples are checked after the high temperature, high pressure treatment to verify the they are completely dissolved and no

sediments are present. The

dissolved sample, with the acidic solution, is then diluted with deionized water to 250 mL and transferred to a 25 mL Teflon flask where it is stored until analysed. The three test recipes are shown in Figure C.2 where two test recipes are tested without the addition of quartz (a); while all are tested with the addition of quartz (b). HNO_3 (1.73 mL) + HF (0.5 mL) is chosen for all subsequent analyses.

In the NTNU HR-ICP-MS facility, three consecutive steps (digestion, dilution, and storage) are performed to digest and dilute the samples and these are performed in three different types of Teflon containers. ICP-MS analysis of blank vessels reveals whether these are contaminated. A blank vessel contains the same acid mixture used to digest the samples, without containing sample.

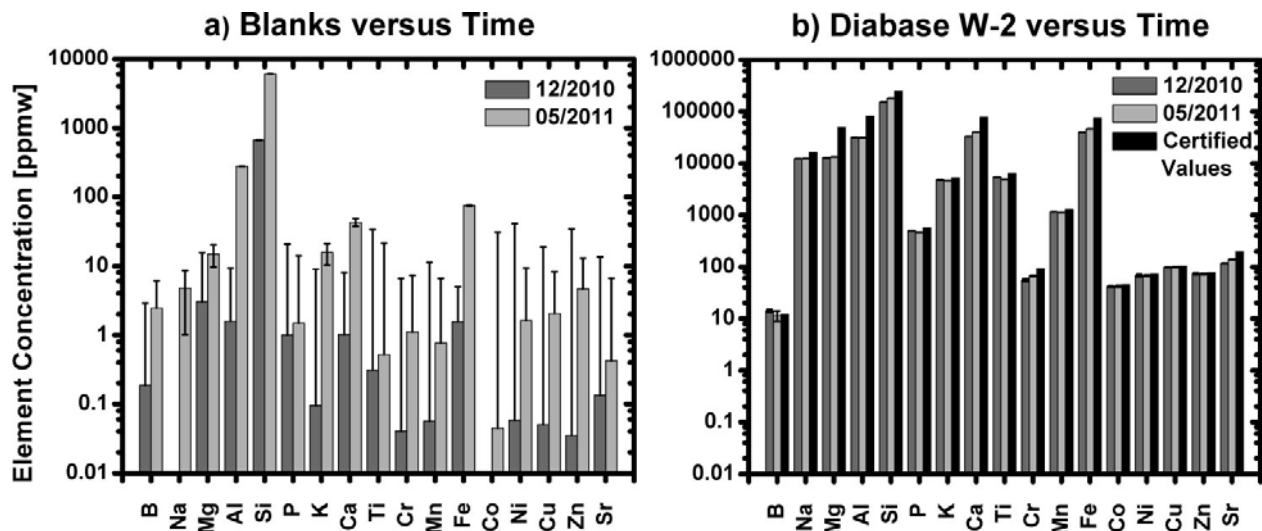


Figure C.2 Blanks (a) and Diabase W-2 reference material (b) versus chemical analysis date.

Acidic digestion is performed in Teflon vessels. A batch of 40 vessels is used for all digestion processes. Vessels are filled with diluted acid and deionized water and they are treated overnight in the ultraclave with the same heating profile shown in Figure C.1. Before starting a new digestion process, they are filled twice with deionized water and rinsed. Samples are inserted in them while being weighted. The sample transfer and weight measurement occur in a laminar flow fume hood used only for this purpose; no tools are used to transfer samples from the tubes they are preserved in to the Teflon vessels. Hence, no unintentional contamination should occur during sample transfer and weight measurement. However, the majority of contamination generally comes from these vessels, due to sample reaction with the acids and eventual residues. For this reason, blanks are always measured in parallel to the samples of interest.

Dilution of the samples is performed in a 250 mL Teflon flask. One single flask is used for this purpose. The flask and its cap are completely filled three times with deionized water before diluting the next sample.

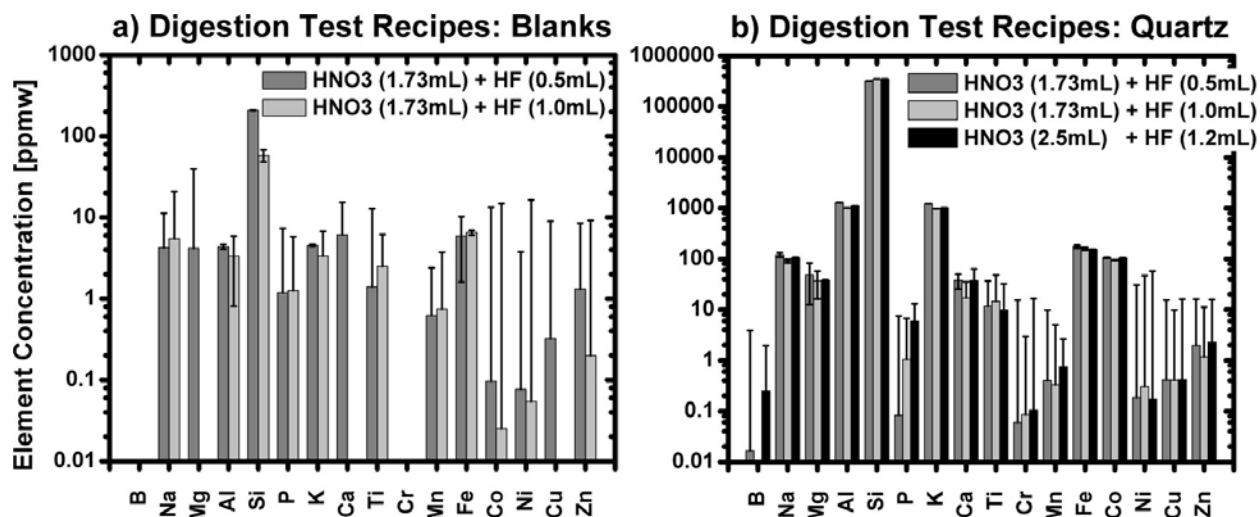


Figure C.3 Test recipes for quartz digestion: a) blank analysis of two of these recipes, b) quartz analysis for all three recipes.

Storage of the diluted sample occurs in 25 mL Teflon flasks. A batch of 100 such flasks is stored with a mixture of diluted acid until filled and rinsed three times with water, and used to store the new samples.

An example of blank analyses is shown in Figure C.3a, whereas analyses of the reference material, Diabase W-2, are depicted in Figure C.3b. Two analytical rounds (12/2010 and 05/2011) are plotted to compare time related differences, which are clearly visible in the blanks, more prone to variations, rather than in the reference material.

C.3. Reference materials

When measuring impurity concentration in quartz via ICP-MS, a reference material is always measured. The National Institute of Standards and technology (NIST) has a wide selection of characterized synthetic materials, or from the United States Geological Survey (USGS), which provides natural (geological) reference materials. Here, Diabase W-2 from USGS is preferred for

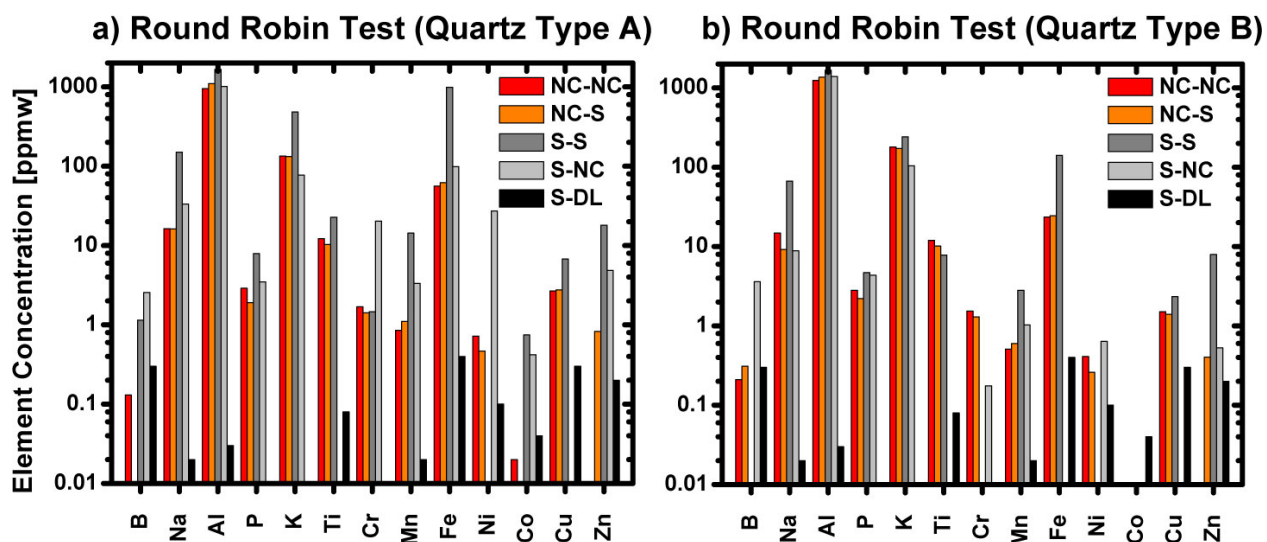


Figure C.4 ICP-MS Round Robin Test between Norwegian Crystallites (NC) and Sintef Materials and Chemistry (S) of two different batches of hydrothermal quartz. Legend notation: “X–Y” = sample digested at “X” then analyzed at “Y”; “S-DL” stands for detection limit at Sintef.

three reasons: a) it is a natural sample; b) the concentration values are similar to the ones expected in the analyzed samples; furthermore, c) it is provided in powder.

C.4. Round Robin Test and Comparison with μ -XRF results

Two analytical laboratories participated in a Round Robin test of two types of quartz, named A and B: an industrial laboratory, Norwegian Crystallites (NC); and a research laboratory, Sintef Materials and Chemistry (S). While the former one preferred keeping digestion procedure and equipment used disclosed, the latter used a Perkin Elmer Elan DRC II.

Quartz pieces (a few mm in diameter) were provided to both laboratories. Digestion was performed in one laboratory; both laboratories would then analyze the solution. The other laboratory would then perform the digestion; and both again analyzed the digested solution. This method allows comparing results of digested and analyzed material within the same facility and

the effect of having another laboratory prepare the digested solution. Test results are shown in Figure C.4, where X-Y denotes the sample was digested at X and analyzed at Y.

As both A and B quartz types are natural minerals, they are intrinsically inhomogeneous. For this reason, small concentration differences are expected among measurements performed in different laboratories simply due to material composition within the amount analyzed. However, some of the values observed, especially in quartz A, cannot be explained by inhomogeneity and a different explanation is provided.

In Figure C.4a, quartz A, dissolved and analyzed at NC (NC-NC, dark orange), shows consistently lower concentrations than when dissolved and analyzed at S (S-S, dark gray). Quartz A dissolved at NC and analyzed at S (NC-S, light orange) has concentration values of the same order of magnitude of the dissolved ones analyzed at NC. Samples digested at S and analyzed at NC (S-NC, light gray) have concentrations lower than when analyzed at S, but higher than when digested at NC. These trends suggest that S has contamination issues during sample preparation occurring prior to the analytical measurement (samples prepared and digested at NC show similar concentration whether they are analyzed at NC or S). Furthermore, the constant higher concentration values found when digested and analyzed in S suggests that also the instrument calibration might be wrong.

Hydrothermal quartz B chemical compositions are shown in Figure C.4b. While in quartz A, NC-NC generally showed lower elemental concentrations than S-S, in the case of quartz B, this is not always the case. For Al, P, K, Ti, and Cu the two analyses provide similar results. However, B, Ti, Fe, and Zn need additional consideration: B concentration, as measured by NC-NC and NC-S, is very close to the detection limit of S.

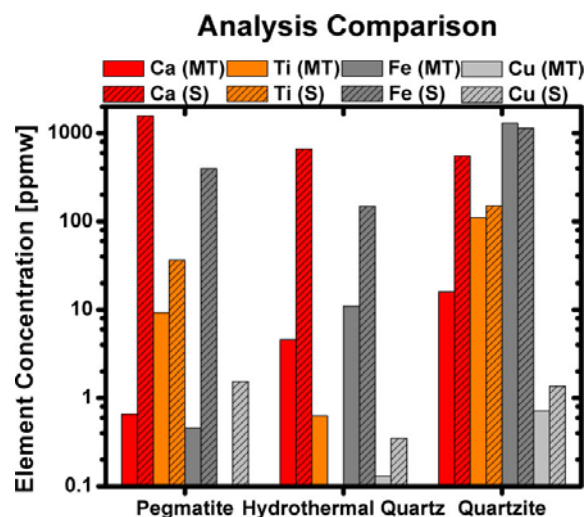


Figure C.5 ICP-MS analyses of four elements in three different types of quartz: high-purity pegmatite, hydrothermal quartz, and quartzite. Result comparison of two analytical facilities: Metron Tech (“MT”, full colour) and Sintef Materials and Chemistry (“S”, textured colour).

ICP-MS Detection Limit	Sintef Materials and Chemistry [ppmw]	Metron Tech [ppbw]
Ca	30	2
Ti	0.08	1
Fe	0.4	2
Cu	0.3	1

Table C.1 Differences in detection limits of the two facilities.

However, S-NC detects higher signal not replicated by S-S. If the increased S-NC signal were due to contamination, S-S should also report a value higher than the detection limit. Even though S-S measures Ti, S-NC doesn’t detect any; this is also visible in quartz A and remains unexplained. Fe has a similar outcome: S-NC detects no Fe. Opposite to Ti, this is not the case for quartz A. The opposite trend is found for Zn, where S-S and S-NC, and NC-S all detect Zn, while NC-NC detects none.

A second analytical comparison was performed with a different set of quartz samples. Sintef Materials and Chemistry analyses were also compared to a commercial laboratory: Metron Tech (Burlingame, CA, USA), was chosen to analyze the three quartz samples, high-purity pegmatite, high-purity hydrothermal quartz, and quartzite. At Metron Tech, before digestion, quartz samples were treated with an acidic etch to remove surface contamination (~ 2 µm). The measurements

were repeated twice and the average is provided in Figure C.5 (full colour) compared to the results obtained from Sintef Materials and Chemistry (textured colour). The two facilities have different resolution capability highlighted by the order of magnitude detection limit differences (Table C.1). For the Metron Tech analyses, measurement error is estimated to be $\pm 50\%$ and $\pm 10\%$, respectively, for values 5 and 10 times higher than the detection limit. No error estimate is available for the Sintef measurements.

Due to the natural geological formation of these samples, the quartzite is expected to be homogeneous over a smaller length scale compared to the other two samples. Among the three samples, this quartz type, being the most impurity rich, will have the highest concentration of all investigated elements. Moreover, elemental concentrations should be far above eventual contamination levels of both facilities, providing a comparison baseline. It is found that concentrations of Ti and Fe measured by MT and S have the same order of magnitude, while Ca shows two orders of magnitude difference, MT being lowest.

Ca, as well as Fe, is extremely difficult to avoid during sample preparation prior to chemical analysis. Ca contamination translates also to the other two samples, the pegmatitic and hydrothermal quartz, where a three order of magnitude difference is measured in the pegmatitic quartz and a two order of magnitude difference in the hydrothermal quartz. Similarly, Fe, with concentrations above contamination level in the quartzite, is also higher in the two high-purity samples: a three order magnitude difference is seen in the pegmatite, and two order magnitude difference is found in the hydrothermal quartz.

As in the round robin test, the Sintef laboratory analysis reveals contamination issues. Analyses become reliable only in samples with elemental concentrations far above the contamination base level.

Bibliography

1. Davis JR, Jr., Rohatgi A, Hopkins RH, Blais PD, Rai-Choudhury P, McCormick JR, Mollenkopf HC. Impurities in silicon solar cells. *IEEE Transactions on Electron Devices* 1980; **27**: 677-687.
2. Pizzini S. Towards solar grade silicon: Challenges and benefits for low cost photovoltaics. *Solar Energy Materials and Solar Cells* 2010; **94**: 1528-1533.
3. Bishop JW. Microplasma breakdown and hot-spots in silicon solar cells. *Solar Cells* 1989; **26**: 335-349.
4. Kwapil W, Gundel P, Schubert MC, Heinz FD, Warta W, Weber ER, Goetzberger A, Martinez-Criado G. Observation of metal precipitates at prebreakdown sites in multicrystalline silicon solar cells. *Applied Physics Letters* 2009; **95**: 232113.
5. Tang K, Øvrelid EJ, Tranell G, Tangstad M, Thermochemical and Kinetic Databases for the Solar Cell Silicon Materials in *Crystal Growth of Si for Solar Cells*, Vol. 14 Eds: Nakajima K, Usami N, Springer Berlin Heidelberg, 2009, 219-251.
6. Hofstetter J, Lelièvre JF, del Cañizo C, Luque A. Acceptable contamination levels in solar grade silicon: From feedstock to solar cell. *Materials Science and Engineering: B* 2009; **159-160**: 299-304.
7. Braga AFB, Moreira SP, Zampieri PR, Bacchin JMG, Mei PR. New processes for the production of solar-grade polycrystalline silicon: A review. *Solar Energy Materials and Solar Cells* 2008; **92**: 418-424.
8. Ceccaroli B, Lohne O, Solar Grade Silicon Feedstock in *Handbook of Photovoltaic Science and Engineering*, Eds: Luque A, Hegedus S, Wiley, 2003.
9. Schei A, Tuset JK, Tveit H. *Production of High Silicon Alloys*, Tapir Vorlag. Trondheim, 1997.
10. Myrhaug EH, *Non-fossil reduction materials in the silicon process - properties and behaviour* Ph.D. Thesis in Department of Materials Technology, Norwegian University of Science and Technology, Trondheim, Norway 2003.
11. Aasly K, *Properties and behavior of quartz for the silicon process*, Ph.D. Thesis in Department of Geology and Mineral Resources Engineering, Norwegian University of Science and Technology, Trondheim, Norway 2008.
12. Buonassisi T, Istratov AA, Pickett MD, Heuer M, Kalejs JP, Hahn G, Marcus MA, Lai B, Cai Z, Heald SM, Ciszek TF, Clark RF, Cunningham DW, Gabor AM, Jonczyk R, Narayanan S, Saunar E, Weber ER. Chemical natures and distributions of metal impurities in multicrystalline silicon materials. *Progress in Photovoltaics: Research and Applications* 2006; **14**: 512-531.

13. Coletti G, Kvande R, Mihailitchi VD, Geerligs LJ, Arnberg L, Ovreid EJ. Effect of iron in silicon feedstock on p- and n-type multicrystalline silicon solar cells. *Journal of Applied Physics* 2008; **104**: 104913.
14. Macdonald D, Tan J. Impurities in solar-grade silicon. *Proceedings of the Device and Process Technologies for Microelectronics, MEMS, Photonics, and Nanotechnology IV*, Canberra, ACT, Australia, 2007; 68000X.
15. Istratov AA, Buonassisi T, Pickett MD, Heuer M, Weber ER. Control of metal impurities in "dirty" multicrystalline silicon for solar cells. *Materials Science and Engineering: B* 2006; **134**: 282-286.
16. Coletti G, Bronsveld PCP, Hahn G, Warta W, Macdonald D, Ceccaroli B, Wambach K, Le Quang N, Fernandez JM. Impact of Metal Contamination in Silicon Solar Cells. *Advanced Functional Materials* 2011; **21**: 879-890.
17. Tang K, Øvreid E, Tranell G, Tangstad M. Critical assessment of the impurity diffusivities in solid and liquid silicon. *JOM Journal of the Minerals, Metals and Materials Society* 2009; **61**: 49-55.
18. Weber ER. Transition metals in silicon. *Applied Physics A: Materials Science & Processing* 1983; **30**: 1-22.
19. Rohatgi A, Davis JR, Hopkins RH, Rai-Choudhury P, McMullin PG, McCormick JR. Effect of titanium, copper and iron on silicon solar cells. *Solid-State Electronics* 1980; **23**: 415-422.
20. Rohatgi A, Hopkins RH, Davis JR, Jr.; . The properties of polycrystalline silicon solar cells with controlled titanium additions *IEEE Transactions on Electron Devices* 1981; **28**: 103-108
21. Graff K. *Metal impurities in silicon-device fabrication* Springer-Verlag. 1995.
22. Petter K, Djordjevic-Reiss J, Hoffmann V, Bauer M, Buchovska I, Vlasenko T, Beringov S. NAA results for UMG-Si from different sources and qualities. *Proceedings of the Workshop on Arriving at well-founded SoG silicon feedstock specifications, Crystal Clear Project*, Amsterdam, 2008;
23. Martin C, Ndzogha C, Morin F, Bouche J-B, Rancoule G. Detrimental effect of alkaline impurities on fused silica crucible during multi-crystalline ingot growth. *Proceedings of the 3rd International Workshop on Crystalline Silicon Solar Cells (CSSC-3)*, Trondheim, Norway, 2009;
24. Okamoto H. Ca-O (calcium-oxygen). *Journal of Phase Equilibria* 2001; **22**: 87-87.
25. Heaney PJ. Structure and chemistry of the low-pressure silica polymorphs. *Reviews in Mineralogy and Geochemistry* 1994; **29**: 1-40.
26. Danes F, Saint-Aman E, Coudurier L. The Si-C-O system. *Journal of Materials Science* 1993; **28**: 489-495.
27. Jacobson N, Opila E. Thermodynamics of Si-C-O system. *Metallurgical and Materials Transactions A* 1993; **24**: 1212-1214.

28. Nagamori M, Malinsky I, Claveau A. Thermodynamics of the Si-C-O system for the production of silicon carbide and metallic silicon. *Metallurgical and Materials Transactions B* 1986; **17**: 503-514.
29. Wiik K, *Kinetics of reactions between silica and carbon*, Dr. Ing. Thesis in Institutt for Uorganisk Kjemi, Norges Tekniske Høgskole, Trondheim, Norway 1990, 220.
30. Andersen V, *Reaction mechanism and kinetics of the high temperature reactions in the silicon process*, MS Thesis in Materials Science and Engineering, Norwegian University of Science and Technology, Trondheim 2010, 89.
31. Andersson M, *Reaction mechanisms in the ferrosilicon production process: results from an industrial furnace excavation*, MS Thesis in Chemical Engineering and Geosciences / Process Metallurgy, Luleå University of Technology, Luleå, Sweden 2009, 207.
32. Filsinger DH, Bourrie DB. Silica to Silicon: Key Carbothermic Reactions and Kinetics. *Journal of the American Ceramic Society* 1990; **73**: 1726-1732.
33. Tveit H, Halland T, Landrø K-I, Johansen ST, Ravary B. The tapping process in silicon production. *Proceedings of the Silicon for the Chemical Industry VI*, Loen, Norway, 2002; 39-46.
34. Kadkhodabeigi M, Tveit H, Johansen ST, in *Seventh International Conference on CFD in the Minerals and Process Industries*, Melbourne, Australia 2009.
35. Rosenqvist T, Tuset J. Discussion of "thermodynamics of the Si-C-O system for the production of silicon carbide and metallic silicon. *Metallurgical and Materials Transactions B* 1987; **18**: 471-472.
36. De Vries A. Determination of the Absolute Configuration of alpha-Quartz. *Nature* 1958; **181**: 1193-1193.
37. Levien L, Prewitt CT, Weidner DJ. Structure and elastic properties of quartz at pressure. *American Mineralogist* 1980; **65**: 920-930.
38. Larsen RB, Henderson I, Ihlen PM, Jacamon F. Distribution and petrogenetic behaviour of trace elements in granitic pegmatite quartz from South Norway. *Contributions to Mineralogy and Petrology* 2004; **147**: 615-628.
39. Graetsch H, Flörke OW, Miehe G. Structural defects in microcrystalline silica. *Physics and Chemistry of Minerals* 1987; **14**: 249-257.
40. Hurst VJ, Storch SP. Regional variation in the cell dimensions of metamorphic quartz. *American Mineralogist* 1981; **66**: 204-212.
41. Hiraga T, Anderson IM, Kohlstedt DL. Grain boundaries as reservoirs of incompatible elements in the Earth's mantle. *Nature* 2004; **427**: 699-703.
42. Wu P, Eriksson G, Pelton AD, Blander M. Prediction of the thermodynamic properties and phase-diagrams of silicate systems - evaluation of the FeO-MgO-SiO₂ system. *ISIJ Int.* 1993; **33**: 26-35.

43. Kaufman L. Calculation of multicomponent ceramic phase diagrams. *Physica B+C* 1988; **150**: 99-114.
44. Taylor JR, Dinsdale AT. Thermodynamic and phase diagram data for the CaO-SiO₂ system. *Calphad* 1990; **14**: 71-88.
45. Tuttle OF. The variable inversion temperature of quartz as a possible geologic thermometer. *American Mineralogist* 1949; **34**: 723-730.
46. Van Goethem L, Van Landuyt J, Amelinckx S. The α - β transition in amethyst quartz as studied by electron microscopy and diffraction. The interaction of Dauphiné with Brazil twins. *Physica Status Solidi (a)* 1977; **41**: 129-137.
47. Tucker MG, Keen DA, Dove MT. A detailed structural characterization of quartz on heating through the alpha-beta phase transition. *Mineralogical Magazine* 2001; **65**: 489-507.
48. Keskar NR, Chelikowsky JR. Structural properties of nine silica polymorphs. *Physical Review B* 1992; **46**: 1.
49. Swamy V, Saxena SK, Sundman B, Zhang J. A thermodynamic assessment of silica phase diagram. *Journal of Geophysical Research* 1994; **99**: 11787-11794.
50. Fenner CN. The stability relations of the silica minerals. *Am J Sci* 1913; **s4-36**: 331-384.
51. Mosesman MA, Pitzer KS. Thermodynamic Properties of the Crystalline Forms of Silica. *Journal of the American Chemical Society* 1941; **63**: 2348-2356.
52. Kihara K. Thermal change in unit-cell dimensions, and a hexagonal structure of tridymite. *Zeitschrift für Kristallographie* 1978; **148**: 237-253.
53. Scherer G, Vergano PJ, Uhlmann DR. A study of quartz melting. *Physics and Chemistry of Glasses* 1970; **11**.
54. Ainslie NG, Morelock CR, Turnbull D, in *Symposium on Nucleation and Crystallization in Glasses and Melts*, American Chemical Society, 1962, 97-107.
55. Ainslie NG, Mackenzie JD, Turnbull D. Melting kinetics of quartz and cristobalite. *The Journal of Physical Chemistry* 1961; **65**: 1718-1724.
56. Uhlmann DR. On the internal nucleation of melting. *Journal of Non-Crystalline Solids* 1980; **41**: 347-357.
57. Cherniak DJ. Diffusion in Quartz, Melilite, Silicate Perovskite, and Mullite. *Reviews in Mineralogy and Geochemistry* 2010; **72**: 735-756.
58. Frischat GH. Cation transport in quartz crystals- 3, (Kationentransport in Quarzkristallen). 1970; **47**: 364-368.
59. Cherniak DJ, Watson EB, Wark DA. Ti diffusion in quartz. *Chemical Geology* 2007; **236**: 65-74.

60. Brady JB, Cherniak DJ. Diffusion in Minerals: An Overview of Published Experimental Diffusion Data. *Reviews in Mineralogy and Geochemistry* 2010; **72**: 899-920.
61. Zhang Y, Cherniak DJ, Eds., *Diffusion in minerals and melts*, Vol. 72, Mineralogical Society of America, 2010.
62. Dohmen R, Milke R. Diffusion in Polycrystalline Materials: Grain Boundaries, Mathematical Models, and Experimental Data. *Reviews in Mineralogy and Geochemistry* 2010; **72**: 921-970.
63. Phillips B, Muan A. Phase Equilibria in the System CaO-Iron Oxide-SiO₂, in Air. *Journal of the American Ceramic Society* 1959; **42**: 413-423.
64. Thompson AB, Aerts M, Hack AC. Liquid Immiscibility in Silicate Melts and Related Systems. *Reviews in Mineralogy and Geochemistry* 2007; **65**: 99-127.
65. Miki T, Morita K, Sano N. Thermodynamic properties of titanium and iron in molten silicon. *Metallurgical and Materials Transactions B* 1997; **28**: 861-867.
66. Miki T, Morita K, Sano N. Thermodynamic properties of aluminum, magnesium, and calcium in molten silicon. *Metallurgical and Materials Transactions B* 1998; **29**: 1043-1049.
67. Istratov AA, Hieslmair H, Weber ER. Iron and its complexes in silicon. *Applied Physics A: Materials Science & Processing* 1999; **69**: 13-44.
68. McHugo SA, Thompson AC, Mohammed A, Lamble G, Perichaud I, Martinuzzi S, Werner M, Rinio M, Koch W, Hoefs H-U, Haessler C. Nanometer-scale metal precipitates in multicrystalline silicon solar cells. *Journal of Applied Physics* 2001; **89**: 4282-4288.
69. Buonassisi T, Istratov AA, Marcus MA, Lai B, Cai Z, Heald SM, Weber ER. Engineering metal-impurity nanodefects for low-cost solar cells. *Nature Materials* 2005; **4**: 676-679.
70. Istratov AA, Buonassisi T, Weber ER, Structural, Elemental, and Chemical Complex Defects in Silicon and Their Impact on Silicon Devices in *Into the Nano Era*, Vol. 106 (Ed: Huff HR, Springer Berlin Heidelberg, 2009, 79-112.
71. Muller A, Koch-Muller M. Hydrogen speciation and trace element contents of igneous, hydrothermal and metamorphic quartz from Norway. *Mineral Mag* 2009; **73**: 569-583.
72. Marcus MA. X-ray photon-in/photon-out methods for chemical imaging. *Trends in Analytical Chemistry* 2010; **29**: 508-517.
73. Westre TE, Kennepohl P, DeWitt JG, Hedman B, Hodgson KO, Solomon EI. A Multiplet Analysis of Fe K-Edge 1s → 3d Pre-Edge Features of Iron Complexes. *Journal of the American Chemical Society* 1997; **119**: 6297-6314.
74. Bonnin-Mosbah M, Métrich N, Susini J, Salomé M, Massare D, Menez B. Micro X-ray absorption near edge structure at the sulfur and iron K-edges in natural silicate glasses. *Spectrochimica Acta Part B: Atomic Spectroscopy* 2002; **57**: 711-725.

75. Marcus MA, Westphal AJ, Fakra SC. Classification of Fe-bearing species from K-edge XANES data using two-parameter correlation plots. *Journal of Synchrotron Radiation* 2008; **15**: 463-468.
76. McHugo SA, Thompson AC, Flink C, Weber ER, Lambie G, Gunion B, MacDowell A, Celestre R, Padmore HA, Hussain Z. Synchrotron-based impurity mapping. *Journal of Crystal Growth* 2000; **210**: 395-400.
77. Buonassisi T, Istratov AA, Marcus MA, Heuer M, Pickett MD, Lai B, Cai Z, Heald SM, ER. W. Local measurements of diffusion length and chemical character of metal clusters in multicrystalline silicon. *Solid State Phenomena* 2005; **108-109**: 577-584.
78. Manceau A, Marcus MA, Tamura N. Quantitative Speciation of Heavy Metals in Soils and Sediments by Synchrotron X-ray Techniques. *Reviews in Mineralogy and Geochemistry* 2002; **49**: 341-428.
79. Berglund A, Brelid H, Rindby A, Engstrom P. Spatial distribution of metal ions in spruce wood by synchrotron radiation microbeam X-ray fluorescence analysis. *Holzforschung* 1999; **53**: 474-480.
80. Buonassisi T, Istratov AA, Peters S, Ballif C, Isenberg J, Riepe S, Warta W, Schindler R, Willeke G, Cai Z, Lai B, Weber ER. Impact of metal silicide precipitate dissolution during rapid thermal processing of multicrystalline silicon solar cells. *Applied Physics Letters* 2005; **87**: 1-3.
81. Marcus MA, MacDowell AA, Celestre R, Manceau A, Miller T, Padmore HA, Sublett RE. Beamline 10.3.2 at ALS: a hard X-ray microprobe for environmental and materials sciences. *Journal of Synchrotron Radiation* 2004; **11**: 239-247.
82. Cai Z, Lai B, Yun W, McNulty I, Khounsary A, Maser J, Ilinski P, Legnini D, Trakhtenberg E, Xu S, Tieman B, Wiemerslage G, Gluskin E. Performance of a high-resolution x-ray microprobe at the Advanced Photon Source. *AIP Conference Proceedings* 2000; **521**: 31-34.
83. Mantler M, Willis JP, Lachance GR, Vrebos BAR, Mauser K-E, Kawahara N, Rousseau RM, Brouwer PN, Quantitative Analysis in *Handbook of Practical X-Ray Fluorescence Analysis* Eds: Burkhard B, Kanngiesser B, Langhoff N, Wedell R, Wolff H, Springer-Verlag, 2006, 309-410.
84. Kraft S, Stuempel J, Becker P, Kuertgens U. High resolution X-ray absorption spectroscopy with absolute energy calibration for the determination of the absorption edge energies. *Review of Scientific Instruments* 1996; **67**: 681-687.
85. Kelly SD, Hesterberg D, Ravel B, Analysis of soils and minerals using X-ray absorption spectroscopy in *Methods of Soil Analysis, Part 5—Mineralogical Methods*, Eds: Ulery AL, Drees LR, Soil Science Society of America, Madison, WI 2008, 367-464.
86. Wilke M, Partzsch GM, Bernhardt R, Lattard D. Determination of the iron oxidation state in basaltic glasses using XANES at the K-edge. *Chemical Geology* 2005; **220**: 143-161.
87. Farges F, Brown GE, Rehr JJ. Ti K-edge XANES studies of Ti coordination and disorder in oxide compounds: Comparison between theory and experiment. *Physical Review B* 1997; **56**: 1809.

88. Waychunas GA. Synchrotron radiation XANES spectroscopy of Ti in minerals: Effects of Ti bonding distances, Ti valence, and site geometry on absorption edge structure. *American Mineralogist* 1987; **72**: 89-101.
89. Westphal AJ, et al. Mixing Fraction of Inner Solar System Material in Comet 81P/Wild2. *The Astrophysical Journal* 2009; **694**: 18.
90. Di Sabatino M, Dons AL, Hinrichs J, Arnberg L. Determination of relative sensitivity factors for trace element analysis of solar cell silicon by fast-flow glow discharge mass spectrometry. *Spectrochimica Acta Part B: Atomic Spectroscopy* 2011; **66**: 144-148.
91. Bernardis S, Newman BK, Di Sabatino M, Fakra SC, Bertoni MI, Fenning DP, Larsen RB, Buonassisi T. Synchrotron-based microprobe investigation of impurities in raw quartz-bearing and carbon-bearing feedstock materials for photovoltaic applications. *Progress in Photovoltaics: Research and Applications* 2011; DOI: 10.1002/pip.1126.
92. Larsen RB, Jacamon F, Kronz A. Trace element chemistry and textures of quartz during the magmatic hydrothermal transition of Oslo Rift granites. *Mineralogical Magazine* 2009; **73**: 691-707.
93. Larsen RB, Polvé M, Juve G. Granite pegmatite quartz from Evje-Iveland: Trace element chemistry and implications for high-purity quartz formation. *Norges Geologiske Undersøkelse Bulletin* 2000; **436**: 57-65.
94. Sørensen B, Larsen R. Coupled trace element mobilisation and strain softening in quartz during retrograde fluid infiltration in dry granulite protoliths. *Contributions to Mineralogy and Petrology* 2009; **157**: 147-161.
95. Monsen BE, Grønli M, Nygaard L, Tveit H. The use of biocarbon in Norwegian ferroalloy production. *Proceedings of the INFACON 9*, Quebec, Canada, 2001; 268-276.
96. Monsen BE, Ratvik AP, Lossius LP. Charcoal in anodes for aluminium production. *Proceedings of the Light Metals 2010 - TMS 2010 Annual Meeting and Exhibition, February 14, 2010 - February 18, 2010*, Seattle, WA, United states, 2010; 929-934.
97. Wark D, Watson E. TitaniQ: a titanium-in-quartz geothermometer. *Contributions to Mineralogy and Petrology* 2006; **152**: 743-754.
98. Murray JP, Flamant G, Roos CJ. Silicon and solar-grade silicon production by solar dissociation of Si₃N₄. *Solar Energy* 2006; **80**: 1349-1354.
99. Hofmeister AM, Rose TP, Hoering TC, Kushiro I. Infrared spectroscopy of natural, synthetic, and oxygen-18-substituted .alpha.-tridymite: structural implications. *The Journal of Physical Chemistry* 1992; **96**: 10213-10218.
100. Rosenqvist T. *Principles of Extractive Metallurgy* Tapir Academic Press. Trondheim, 2004.
101. Ozturk B, Fruehan R. The rate of formation of SiO by the reaction of CO or H₂ with silica and silicate slags. *Metallurgical and Materials Transactions B* 1985; **16**: 801-806.

102. Ghiorso M, Carmichael I, Moret L. Inverted high-temperature quartz. *Contributions to Mineralogy and Petrology* 1979; **68**: 307-323.
103. Stevens S, Hand R, Sharp J. Polymorphism of silica. *Journal of Materials Science* 1997; **32**: 2929-2935.
104. Turnbull D, Cohen MH. Concerning Reconstructive Transformation and Formation of Glass. *The Journal of Chemical Physics* 1958; **29**: 1049-1054.
105. Rao BJ, Chetal AR. An X-ray K-absorption study of muscovite mica. *Journal of Physics D: Applied Physics* 1982; **15**: L195.
106. Jain DC, et al. X-ray absorption study of some iron-rich micas. *Journal of Physics D: Applied Physics* 1980; **13**: 1113.
107. Dyar MD, Delaney JS, Sutton SR. Fe XANES spectra of iron-rich micas. *European Journal of Mineralogy* 2001; **13**: 1079-1098.
108. Petit P-E, Farges F, Wilke M, Sole VA. Determination of the iron oxidation state in Earth materials using XANES pre-edge information. *Journal of Synchrotron Radiation* 2001; **8**: 952-954.
109. Evans BW. Application of a reaction-rate method to the breakdown equilibria of muscovite and muscovite plus quartz. *American Journal of Science* 1965; **263**: 647-667.
110. Rancourt DG, Tume P, Lalonde AE. Kinetics of the $(\text{Fe}_2+\text{OH}^-)\text{mica} \rightarrow (\text{Fe}_3+\text{O}_2^-)\text{mica} + \text{H}$ oxidation reaction in bulk single-crystal biotite studied by Mössbauer spectroscopy. *Physics and Chemistry of Minerals* 1993; **20**: 276-284.
111. Hammouda T, Pichavant M. Kinetics of melting of fluorophlogopite-quartz pairs at 1 atmosphere. *European Journal of Mineralogy* 1999; **11**: 637-653.
112. Hillert M, Wang X. A study of the thermodynamic properties of MgO-SiO₂ system. *Calphad* 1989; **13**: 253-266.
113. Ohmoto H, Kerrick DM. Devolatilization equilibria in graphitic systems. *American Journal of Science* 1977; **277**: 1013-1044.
114. Jakobsson S, Oskarsson N. The system C-O in equilibrium with graphite at high pressure and temperature: An experimental study. *Geochimica et Cosmochimica Acta* 1994; **58**: 9-17.
115. Gotze J. Chemistry, textures and physical properties of quartz - geological interpretation and technical application. *Mineralogical Magazine* 2009; **73**: 645-671.
116. Muller A, Wiedenbeck M, Kerkhof AMVD, Kronz A, Simon K. Trace elements in quartz - a combined electron microprobe, secondary ion mass spectrometry, laser-ablation ICP-MS, and cathodoluminescence study. *Eur J Mineral* 2003; **15**: 747-763.
117. Baud L, Margaria T. Silicon for silicones: A developing route for P.E.M. . *Proceedings of the INFACON VII*, Trondheim, Norway, 1995; 655-664.

118. Øvrelid EJ, Tang K, Engh T, Tangstad M, Feedstock in *Crystal Growth of Si for Solar Cells*, Vol. 14 Eds: Nakajima K, Usami N, Springer Berlin Heidelberg, 2009, 1-23.
119. Shimpo T, Yoshikawa T, Morita K. Thermodynamic study of the effect of calcium on removal of phosphorus from silicon by acid leaching treatment. *Metallurgical and Materials Transactions B* 2004; **35**: 277-284.
120. Pizzini S, Acciarri M, Binetti S. From electronic grade to solar grade silicon: chances and challenges in photovoltaics. *physica status solidi (a)* 2005; **202**: 2928-2942.
121. Olsen E, Øvrelid EJ. Silicon nitride coating and crucible—effects of using upgraded materials in the casting of multicrystalline silicon ingots. *Progress in Photovoltaics: Research and Applications* 2008; **16**: 93-100.
122. Kvande R, Arnberg L, Martin C. Influence of crucible and coating quality on the properties of multicrystalline silicon for solar cells. *Journal of Crystal Growth* 2009; **311**: 765-768.
123. Trumbore FA. Solid solubilities of impurity elements in germanium and silicon. *Bell System Technical Journal* 1960; **39**: 205-233.
124. Tucker NP. Alloys of iron research, Part VII, preparation of high purity silicon. *Journal of Iron and Steel Institute* 1927; **15**: 412-414.
125. Chu TL, Chu SS. Partial Purification of Metallurgical Silicon by Acid Extraction. *Journal of The Electrochemical Society* 1983; **130**: 455-457.
126. Dietl J. Hydrometallurgical purification of metallurgical-grade silicon. *Solar Cells* 1983; **10**: 145-154.
127. Norman CE, Absi EM, Thomas RE. *Solar-grade silicon substrates by a powder-to-ribbon process*, National Research Council of Canada. Ottawa, CANADA, 1985.
128. Juneja JM, Mukherjee TK. A study of the purification of metallurgical grade silicon. *Hydrometallurgy* 1986; **16**: 69-75.
129. Santos IC, Gonçalves AP, Santos CS, Almeida M, Afonso MH, Cruz MJ. Purification of metallurgical grade silicon by acid leaching. *Hydrometallurgy* 1990; **23**: 237-246.
130. Ma X, Zhang J, Wang T, Li T. Hydrometallurgical purification of metallurgical grade silicon. *Rare Metals* 2009; **28**: 221-225.
131. Aulich HA, Eisenrith KH, Urbach HP. New methods to prepare high-purity silica. *Journal of Materials Science* 1984; **19**: 1710-1717.
132. Patermarakis G, Paspaliaris Y. The leaching of iron oxides in boehmitic bauxite by hydrochloric acid. *Hydrometallurgy* 1989; **23**: 77-90.
133. Ubaldini S, Piga L, Fornari P, Massidda R. Removal of iron from quartz sands: A study by column leaching using a complete factorial design. *Hydrometallurgy* 1996; **40**: 369-379.

134. Vegliò F, Passariello B, Toro L, Marabini AM. Development of a Bleaching Process for a Kaolin of Industrial Interest by Oxalic, Ascorbic, and Sulfuric Acids: Preliminary Study Using Statistical Methods of Experimental Design. *Industrial & Engineering Chemistry Research* 1996; **35**: 1680-1687.
135. Veglio F. Factorial experiments in the development of a kaolin bleaching process using thiourea in sulphuric acid solutions. *Hydrometallurgy* 1997; **45**: 181-197.
136. Taxiarchou M, Pnias D, Douni I, Paspaliaris I, Kontopoulos A. Removal of iron from silica sand by leaching with oxalic acid. *Hydrometallurgy* 1997; **46**: 215-227.
137. Vegliò F, Passariello B, Barbaro M, Plescia P, Marabini AM. Drum leaching tests in iron removal from quartz using oxalic and sulphuric acids. *International Journal of Mineral Processing* 1998; **54**: 183-200.
138. Lanyon MR, Lwin T, Merritt RR. The dissolution of iron in the hydrochloric acid leach of an ilmenite concentrate. *Hydrometallurgy* 1999; **51**: 299-323.
139. Vegliò F, Passariello B, Abbruzzese C. Iron Removal Process for High-Purity Silica Sands Production by Oxalic Acid Leaching. *Industrial & Engineering Chemistry Research* 1999; **38**: 4443-4448.
140. Ambikadevi VR, Lalithambika M. Effect of organic acids on ferric iron removal from iron-stained kaolinite. *Applied Clay Science* 2000; **16**: 133-145.
141. Barrett DA, Brown VA, Watson RC, Davies MC, Shaw PN, Ritchie HJ, Ross P. Effects of acid treatment on the trace metal content of chromatographic silica: bulk analysis, surface analysis and chromatographic performance of bonded phases. *Journal of Chromatography A* 2001; **905**: 69-83.
142. Lee SO, Tran T, Park YY, Kim SJ, Kim MJ. Study on the kinetics of iron oxide leaching by oxalic acid. *International Journal of Mineral Processing* 2006; **80**: 144-152.
143. Lee SO, Tran T, Jung BH, Kim SJ, Kim MJ. Dissolution of iron oxide using oxalic acid. *Hydrometallurgy* 2007; **87**: 91-99.
144. Arslan V, Bayat O. Removal of Fe from kaolin by chemical leaching and bioleaching. *Clays and Clay Minerals* 2009; **57**: 787-794.
145. Lee K, Yoon Y, Jeong S, Chae Y, Ko K. Acid leaching purification and neutron activation analysis of high purity silicas. *Journal of Radioanalytical and Nuclear Chemistry* 2009; **282**: 629-633.
146. Du F, Li J, Li X, Zhang Z. Improvement of iron removal from silica sand using ultrasound-assisted oxalic acid. *Ultrasonics Sonochemistry* 2011; **18**: 389-393.
147. Andres U. Electrical disintegration of rock. *Mineral Processing and Extractive Metallurgy Review: An International Journal* 1995; **14**: 87-110.
148. Andres U, Jirestig J, Timoshkin I. Liberation of minerals by high-voltage electrical pulses. *Powder Technology* 1999; **104**: 37-49.

149. Andres U, Timoshkin I, Jirestig J, Stallknecht H. Liberation of valuable inclusions in ores and slags by electrical pulses. *Powder Technology* 2001; **114**: 40-50.
150. Andres U, Timoshkin I, Soloviev M. Energy consumption and liberation of minerals in explosive electrical breakdown of ores. *Mineral Processing and Extractive Metallurgy* 2001; **110**: 149-157.
151. Andres U. Development and prospects of mineral liberation by electrical pulses. *International Journal of Mineral Processing* 2010; **97**: 31-38.